Dissertation

submitted to the
Combined Faculties for the Natural Sciences and for Mathematics
of the Ruperto-Carola University of Heidelberg, Germany
for the degree of
Doctor of Natural Sciences

Presented by:
Dipl.-Phys. Wanqing Xiang (项晚晴)
born in Wuhan, China

Oral examination:
November 9th, 2015

Structure and Dynamics of Replication Domains in Single Chromosome Territories of Interphase Nuclei

Referees:
Dr. Christoph Müller
Prof. Dr. Ulrich Schwarz

Summary

Knowing the three-dimensional organization of chromatin sets the framework for understanding genome regulation. Our picture of higher order chromatin structure *in situ* however remains fragmentary at many scales, since it is not directly accessible by imaging technologies available today. The recently revealed domain organization of chromatin subunits into sub-megabasepair sized topologically associating domains (TADs), enabled by chromosome conformation capture based techniques, marks a significant advancement in understanding chromatin architecture. Similarly quantitative methods for the analysis of global structure and dynamics of chromatin in single living cells are currently lacking, leaving it unclear how TADs are manifested within a single nucleus and how dynamic topological chromatin interactions are in living cells. To start to address this gap in our knowledge, I set out to systematically probe the basic polymer features of chromatin at the level of replication domains (RDs) in single cells as a basis for a model of higher order chromatin organization.

I have addressed both structural and dynamic aspects of RD organization during interphase. Using super-resolution microscopy, I was able to investigate RD organization at unprecedented resolution. I found that the median RD diameter is ~150 nm, significantly smaller than the ~270 nm distance to the nearest neighbor, which leaves sufficient physical space for extended linker regions between RDs. By quantifying correlated motion of neighboring RDs, I could reveal the typical elastic coupling range between RDs to be ~500 nm. Combining super-resolution microscopy with a perturbation experiment I could further obtain evidence for the model that chromatin compaction upon ATP depletion is predominantly mediated by preferential compaction of linker regions between RDs, rather than by compaction of RDs themselves.

In addition to these structural parameters of RD organization, I also characterized the diffusional behavior of interphase RDs of single chromosome territories. Tracking 1,372 RDs of 141 chromosome territories allowed me to obtain a global and statistically robust view of interphase chromatin dynamics across the entire nucleus. My data confirms that heterochromatin chromatin is immobile within a few hundred nanometers of the nuclear membrane and nucleolar surface over the time scale of several minutes and that nucleoplasmic dynamics is characterized by anomalous diffusion. I did not observe reproducible directed motion of RDs on the timescale of seconds to a minute. I observed a systematic reduction in chromatin motion as the cell cycle progressed from G1 to late S-phase and an increase in mobility if I artificially increased nuclear volume by allowing cells to grow when DNA replication was inhibited.

My observations on native and perturbed chromatin structure and dynamics in nuclei of living cells allow me to propose a comprehensive model of higher order chromatin organization in single cells, that consists of stable structuring units of RDs, which are connected by extended flexible linker domains, whose dynamics are limited by attachment to the nuclear periphery and nucleoli and the available free volume inside the nucleus.

Zusammenfassung

Die Kenntnis der räumlichen Chromatin-Organisation ist eine Grundlage für das Verständnis der Genregulation. Unser Bild der höheren Ordnung des Chromatins *in situ* ist jedoch lückenhaft, da sie nicht direkt mit heutigen bildgebenden Verfahren zugänglich gemacht werden kann. Die vor kurzem durch Chromosom-Konformationserfassung ermöglichte Erforschung der Organisation von Chromatin-Untereinheiten in topologisch assoziierte Domänen stellt einen wichtigen Schritt für das Verständnis der Chromatin-Architektur dar. Ähnlich globale, quantitative Methoden, die Struktur und Dynamik des Chromatins individueller lebender Zellen beschreiben, fehlen derzeit. Daher ist es noch immer unklar, wie topologisch assoziierte Domänen in der einzelnen Zelle ausgeprägt sind, und wie dynamisch Chromatin-Interaktionen in lebenden Zellen sind. Um diese Wissenslücke zu adressieren, habe ich eine systematische Untersuchung der grundlegenden Polymereigenschaften von Chromatin auf der Ebene von Replikationszentren (RZ) durchgeführt – mit dem Ziel ein Modell der höheren Ordnung des Chromatins im Zellkern zu entwickeln.

Zu diesem Zweck habe ich strukturelle und dynamische Aspekte der Organisation von RZ während der Interphase beleuchtet. Mit Hilfe von superauflösender Fluoreszenzmikroskopie habe ich die Organisation von RZ untersucht. So konnte ich messen, dass der Durchmesser von RZ im Median ~150 nm beträgt, deutlich kleiner als der Median der Distanz zum nächstgelegenen Nachbarn, der ~270 nm beträgt. Daraus folgere ich, dass ausreichend Raum für ausgedehnte Verbindungselemente zwischen benachbarten RZ vorhanden ist. Indem ich korrelierte Bewegung benachbarter RZ quantifiziert habe, konnte ich eine elastische Kopplungsreichweite von ~500 nm messen. Zudem habe ich durch Kombinierung von superauflösender Mikroskopie und einem Störungsexperiment Hinweise darauf gefunden, dass eine durch ATP-Entzug verursachte Chromatin-Verdichtung maßgeblich durch Verdichtung der Verbindungselemente verursacht wird, und weniger durch gleichförmige Verdichtung der RZ selbst.

Zusätzlich zu den strukturellen Parametern von RZ Organisation habe ich in lebenden Zellen Diffusionseigenschaften von RZ in einzelnen Chromosomenterritorien (CT) über mehrere Minuten charakterisiert. Ich habe Trajektorien von 1.372 RZ von 141 einzelnen CT ausgewertet und konnte dadurch eine umfassende und statistisch robuste Übersicht der Chromatin-Dynamik im gesamten Zellkern erlangen. Meine Daten bestätigen, dass Heterochromatin im Abstand weniger hundert Nanometer von der Kernmembran oder den Nucleoli quasi immobilisiert ist, während die Mobilität im Kernplasma durch anomale Diffusion geprägt ist. Hinweise für direktionale Bewegung von RZ habe ich nicht gefunden. Desweiteren habe ich eine Verminderung der Mobilität während des Zellzyklus von der G1-phase bis in die späte S-phase beobachtet. Eine Zunahme der Dynamik konnte ich nach künstlich induzierter Vergrößerung des Kernvolumens beobachten.

Zusammenfassend beschreiben meine Erkenntnisse zu nativer und gestörter Chromatinstruktur und -dynamik ein umfassendes Modell der höheren Chromatinordnung auf Einzelzellebene. Es beschreibt Chromatin bestehend aus stabilen, aneinandergereihten Struktureinheiten, den RZ, die durch ausgedehnte, flexible Verbindungsdomänen verbunden sind. Die Dynamik der RZ wird durch Anheftung an die Kernperipherie oder Nukleoli und durch den begrenzten Raum im Zellkern limitiert.

Contents

List of Figures

List of Abbreviations

2D	Two-dimension(al)
3D	Three-dimension(al)
SIM	Structured illumination microscopy
APD	Avalanche photodiode
ATP	Adenosine triphosphate
ATR	Ataxia telangiectasia and Rad3 related (gene)
CLSM	Confocal light scanning microscopy
CT	Chromosome territory
CTCF	CCCTC-binding factor (gene)
DMEM	Dulbecco's modified Eagle medium
DMSO	Dimethyl sulfoxide
DNA	Deoxyribonucleic acid
dUTP	Deoxyuridine triphosphate
eGFP	Enhanced green fluorescent protein (gene)
EM	Electron microscopy
FBS	Fetal bovine serum
FISH	Fluorescence in-situ hybridization
GaAsP-PMT	Gallium arsenide phosphide photomultiplier tubes
GFP	Green fluorescent protein
GSDIM	Ground state depletion followed by individual molecule return
H2B	Histone H2B
HEPES	4-(2-hydroxyethyl)-1-piperazineethanesulfonic acid
IgH	Immunoglobulin heavy chain
kb	Kilobasepair
KS-test	Kolmogorov-Smirnov test
MATLAB	Matrix laboratory (Mathworks)

Mb	Megabasepair
MSD	Mean-square-displacement
NRK cells	Normal rat kidney epithelial cells
PBS	Phosphate-buffered saline
PCNA	Proliferating cell nuclear antigen (gene)
RD	Replication Domain
RF	Replication Focus
STED	Stimulated emission depletion microscopy
TAD	Topologically associating domains
TSA	Trichostatin A

1 Introduction

1.1 Higher Order Chromosome Organization

In recent years, many observations have added up to the picture that information on the linear DNA sequence alone does not suffice to understand how the information encoded in the genome leads to biological function. This is especially becoming clear for how transcription is regulated. Regulatory elements such as promoters and enhancers work through physical contact (Lenhard et al., 2012). And there is evidence that nuclear positioning of genes in respect to regulatory elements, transcription factors and nuclear landmarks, such as the nuclear periphery and nuclear bodies can contribute to determine their transcriptional state (reviewed in (Misteli, 2007; Sexton et al., 2007)). Thus, elucidating the dynamic three-dimensional genome organization inside the nucleus is considered to be a key milestone on the way to bridge the genotype-phenotype gap, which is the synonym for understanding the causal connections when relating genome sequence to the phenotypic outcome.

How chromatin folds into higher order structures precisely is still poorly understood, since the amorphous chromatin structure *in situ* has not been directly accessible by the imaging technologies currently available. The core of the problem is the dense packing of chromatin in intact nuclei, especially chromatin of higher eukaryotes. While conventional light microscopy lacks the resolution to distinguish the smallest unit of chromatin, individual nucleosomes, or to follow the path of the DNA fiber within its physiological context, electron microscopy is not yet routinely compatible with specific DNA or chromatin labeling while preserving the fragile native structure of the genome. In label-free electron micrographs of vitrified chromatin samples, the convolved electron densities of the closely stacked proteins and nucleic acids result in poor contrast, leveling the advantage of the superior resolution of electron microscopy. Therefore, much of what is known about chromatin structure today has been derived from isolated or artificially assembled chromatin fibers *in vitro*.

1.1.1 Chromatin Structure from the Bottom up

Starting at the lowest level, about 150 bp of DNA wrap around an octamer of histone proteins forming a nucleosome core particle (Luger et al., 1997). Multiple nucleosomes are linked by stretches of DNA up to 80 bp long. This linker DNA is frequently occupied by the linker histone H1. Histone H1 stabilizes chromatin structure by attaching to the entry and exit point of the DNA wrapped around the core particle (Thoma and Koller, 1977). In isolated chromatin fibers, taken out of their physiological context and exposed to a hypotonic environment, histone H1 is extracted and nucleosomes unravel into what looks like small beads strung on a thread. This structured is commonly referred to as the 10 nm beads-on-a-string fiber (Woodcock, 2006), see Figure 1-1.

Another prominent in-vitro chromatin structure, which has been observed in buffer extracted or assembled chromatin by transmission electron microscopy and also X-ray scattering analysis is the so-called 30 nm fiber (Gall, 1966; Paulson and Langmore, 1983) (Bednar et al., 1995), (Robinson et al., 2006). The 30 nm fiber was later also observed *in situ*, in chicken erythrocytes (Langmore and Schutt, 1980) and starfish spermatocytes (Horowitz et al., 1994) e.g., which are somewhat exceptional cell types, since transcription in these cells is almost completely silenced. The 30 nm fiber is so compact that it so far has not allowed for unambiguous tracing of individual nucleosomes within the fiber to determine its internal structure. Experimental combined with computational efforts to describe the precise conformation of the 30 nm fiber have resulted in a handful of models, the most prominent two being the zig-zag 2-start helix model (Schalch et al., 2005) and the solenoid 1-start helix model (Robinson et al., 2006). It has been further suggested that DNA linker length impacts nucleosome stacking within the 30 nm fiber, and that variations in DNA linker length contribute to variable topology of the 30 nm fiber (Wu et al., 2007).

Higher order structures formed of 30 nm fibers have been reported in an EM study on decondensing chromosomes in G1. Two classes of so-called ‘chromonemas’ where observed, they are reported to be 60–80 nm and 100–130 nm in diameter (Belmont and Bruce, 1994).

On the other hand, methods allowing the best structural preservation, such as cryo-EM studies of vitreous sections have found no signature of the 30 nm fiber or comparable higher order structures in chromatin *in situ* (McDowall et al., 1986; Eltsov et al., 2008; Fussner et al., 2011). These findings question the relevance of the 30 nm fiber structure observed in non-physiological conditions *in vitro* for chromatin of actively transcribed chromatin in most cell types (Tremethick, 2007), (Maeshima et al., 2010; 2014).

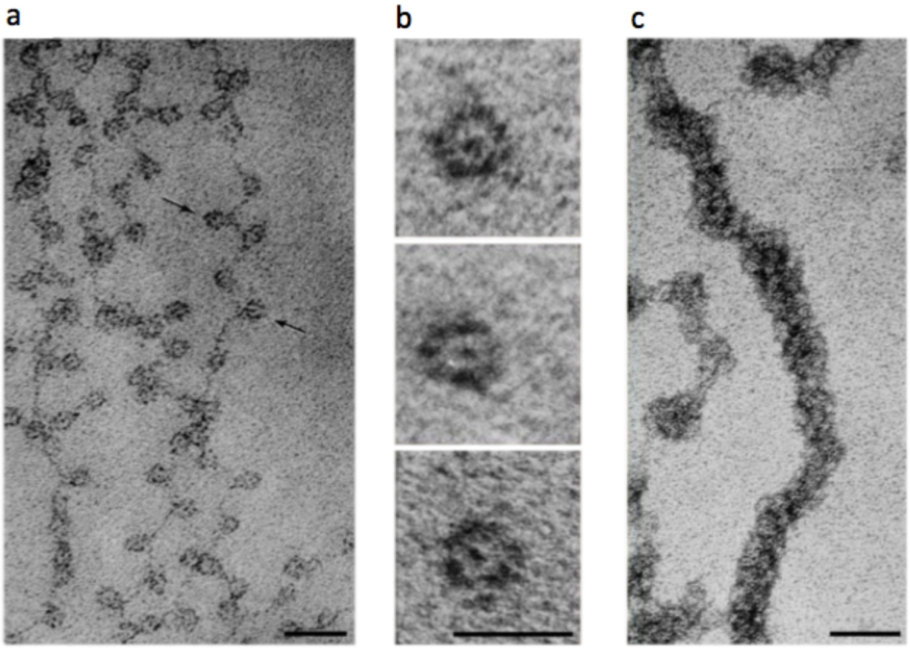

Figure 1-1: Electronmicrographs of the 10 nm fiber and the 30 nm fiber *in vitro*.
a, 10 nm ‘beads on a string’ fiber, arrows point to individual nucleosomes in low ionic-strength chromatin spread. Scalebar 30 nm. **b**, Isolated mononucleosomes from nuclease digested chromatin. Scalebar 10 nm. **c**, 30 nm fiber in moderate ionic strength chromatin spread. Scalebar 50 nm. Figure from (Olins and Olins, 2003).

Even though the precise higher order chromatin structure and its organizing principles remain elusive in situ, many important aspects of chromatin organization have been revealed using various cytological methods, genomic tools and (computational) modeling over the last decades. Different hierarchies and compartmentalization levels of chromatin organization have been revealed. The main findings are introduced in the following sub-chapters.

1.1.2 Functional Compartmentalization of the Cell Nucleus

Membrane-free functional compartmentalization is a hallmark of nuclear organization, particularly in complex organisms such as higher eukaryotes. It ensures that essential processes such as precisely timed transcription of specific genomic sequences, DNA replication, RNA splicing, ribosome synthesis and assembly e.g. can be orchestrated efficiently.

1.1.2.1 Chromosome Territories

During interphase, individual chromosomes in higher eukaryotes are not entirely intertwined, but stay largely confined into their own nuclear space. The subnuclear volume occupied by one chromosome is commonly referred to as the chromosome territory. Boveri hypothesized chromosome territories already in 1909. But over 70 years passed until UV-micro-irradiation experiments demonstrated that chromosome territories indeed existed (Cremer et al., 1982; Zorn et al., 1979). Later theses results were confirmed by fluorescence in-situ hybridization (FISH) experiments (Lichter et al., 1988). FISH allows visualizing single target genes or whole chromosomes by hybridizing fluorescently tagged sequence-complementary hybridization probes to genomic DNA-sequences. A cell nucleus in which individual CTs were individually fluorescently labeled using FISH is shown as an example in Figure 1-2.

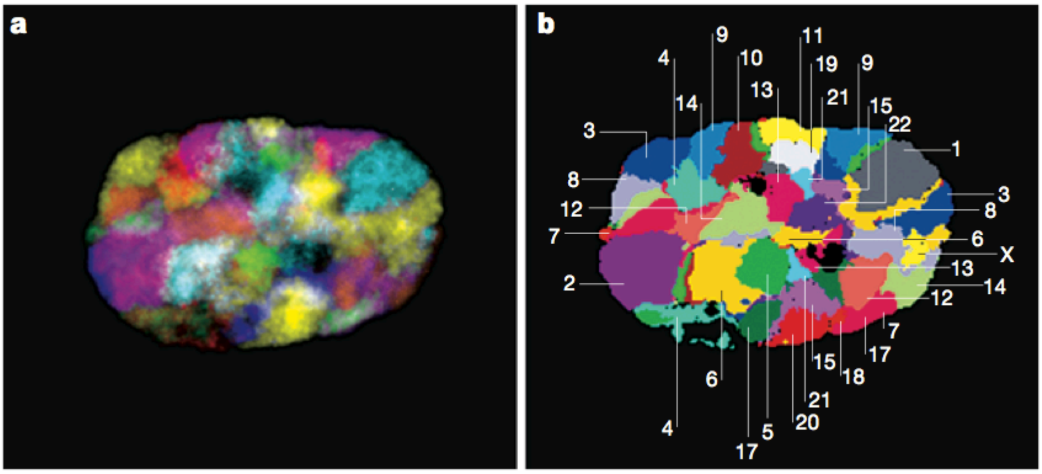

Figure 1-2: Interphase chromosome territories in a human cell nucleus visualized using FISH.
a, The midplane-view of a cell nucleus with FISH painted CTs, 7 color-channels are superimposed. **b,** Each human chromosome territory (Chr 1-22, X, Y) can be unambiguously identified by their unique color-combination used on the hybridization probes. The unsegmented black regions in the nucleus are occupied by nucleoli. Figure modified from (Speicher and Carter, 2005).

Chromosome territories are found in most higher eukaryotes, but not in less complex organisms such as bacteria or lower eukaryotes such as *s. cerevisiae* (reviewed in (Meaburn and Misteli, 2007)). In plants and flies chromosomes are organized in a polarized pattern known as Rabl configuration. Here, telomeres and centromeres are attached to opposite poles of the nucleus (Hochstrasser et al., 1986; Schubert and Shaw, 2011).

Even though there is no rigid, deterministic order of chromosome territories within the cell nucleus, probabilistic patterns do arise (Parada et al., 2003). Preferential chromosomal neighborhoods have been observed in a cell-type specific context (Parada et al., 2002). A hypothesis for an advantage of the enhanced association frequency between specific chromosomes, is that in each cell type particular sets of co-regulated genes, located on different chromosomes, benefit from spatial proximity (Parada et al., 2004). Smaller gene rich chromosomes tend to be located more centrally in the cell nucleus, whereas bigger gene-poor chromosomes containing large heterochromatic regions tend to be located more peripherally (Croft et al., 1999). This non-random radial patterning has been conserved during primate evolution (Tanabe et al., 2002). The accessible, actively transcribed and early replicating euchromatin is located more centrally within the nucleus, while heterochromatin is generally more condensed, transcriptionally silent, late replicating and located mostly around the nuclear periphery and nucleoli (reviewed in (Woodcock and Ghosh, 2010)). The only known extreme exceptions from this architecture are retina rod cells of nocturnal mammals, in which the spatial distribution of euchromatin and heterochromatin are inverted (Solovei et al., 2009). In these cells the condensed heterochromatin residing at the center of the nucleus has been demonstrated to show a lens effect, when light is scattered on these cells. The effect is believed to improving night vision for nocturnal mammals (Solovei et al., 2009).

Chromosome positioning within one cell cycle is usually quite stable, can be partially transmitted through mitotic division (Gerlich et al., 2003), but can change during differentiation and development (Kuroda et al., 2004).

1.1.2.2 Functional Models of Chromatin Architecture

The internal organization of chromosome territories is not yet well known; and even less is known about the principles and forces underlying chromatin organization. This is reflected in somewhat contradictory models, which attribute different roles to the positioning of genes relative to their chromosome territory surface (reviewed in (Rouquette et al., 2010)).

1.1.2.2.1 The Chromosome Territory - Interchromatin Compartment Model (CT-IC)

The chromosome territory – interchromatin compartment (CT-IC) model is based on the observation that the transcription and splicing machineries are relatively excluded from the interior of CTs. The splicing machinery for example was observed to be exclusively found at the CT surface(Zirbel et al., 1993). It was thus suggested that the nucleus contains two distinct compartments, the CTs and a chromatin-free interchromatin space (IC) harboring the nuclear bodies (Cremer et al., 1993), (Albiez et al., 2006; Cremer and Cremer, 2001).

It has been shown for individual genes, e.g. the MHC class II genes and epidermal differentiation complex (EDC) gene, that transcriptional activation can result in their relocalization from within to outside the CT (Volpi et al., 2000; Williams et al., 2002). CT-IC model interpretes this observation as genes looping out of the CT to be transcribed at the CT surface. In an extreme version of this model, transcription decondenses CTs locally to forming giant chromatin loops reaching out several µms (Chubb and Bickmore, 2003). Another study by the Bickmore lab from 2002 suggests that not only active transcription, but also high gene density of genomic regions incline them to loop out of their CT (Mahy et al., 2002).

The CT-IC model envisions little intermingling between neighboring CTs and originally hypothesized that the IC is a contiguous chromatin-free tunnel system connecting the CT surfaces with the nuclear pores. Later the model was slightly adapted for the IC to also permeate through individual CTs (Cremer et al., 1993), (Cremer and Cremer, 2001). The existence of the IC was further supported by an EM study looking at immuno-gold staining against BrdU-labeled chromatin domains. In these electron-micrographs channel-like ‘empty’ structures were visible between the electron-dense chromatin (Visser et al., 2000). It has to be noted though, that the EM protocol used requires harsh chemical treatment of the samples, affecting preservation of native chromatin structure in these samples.

The CT-IC model further further suggests that sub-chromosomal domains located at the interior of CTs are more condensed and less accessible to the transcription machinery compared to domains at the territory surfaces, which are more decondensed and enriched in ribonucleoproteins (RNPs). The authors termed this region 'perichromatin'.

1.1.2.2.2 The Interchromosomal Network Model (ICN)

In 2006 Branco and Pombo proposed the ICN model. They investigated chromatin structure using correlated fluorescence in situ hybridization (FISH) and immuno-gold labeling EM on thin cryosections of painted chromosome territories, and found no evidence of chromatin-free channels or 'perichromatin'. They estimated that about 20% of the nuclear volume is occupied by areas with significant intermingling between neighboring CTs. They further quantified the average DNA concentration across the nucleus. Even though they picked up local variations in DNA concentrations, regions weakly stained by intercalating DNA-dyes, were completely randomly distributed across nuclei. They found the chromatin concentration at CT surfaces unchanged compared to internal regions (Branco and Pombo, 2006). In their model they propose that mixing of euchromatin fibers is driven by constrained diffusion, which does not distinguish whether the fiber moves within the same or between neighboring chromosomes. Interestingly, the areas of interchromsomal overlap changed structurally in response to inhibition of transcription and the degree of intermingling between neighboring chromosomes decreased significantly. The authors therefore propose that transcription stabilizes inter-CT chromatin-associations (Branco and Pombo, 2006).

The authors note that their model is supported by a study using electron spectroscopy imaging (ESI) which also found a rather homogeneous chromatin distribution across the nucleus and no signatures of chromatin-free channels within the nucleus (Dehghani et al., 2005). The advantage of ESI over EM is that it allows distinguish proteins from nuclear acids by their respective high content of nitrogen and phosphorus. Cartoons of both the CT-IC and ICN models are shown in direct comparison in Figure 1-3.

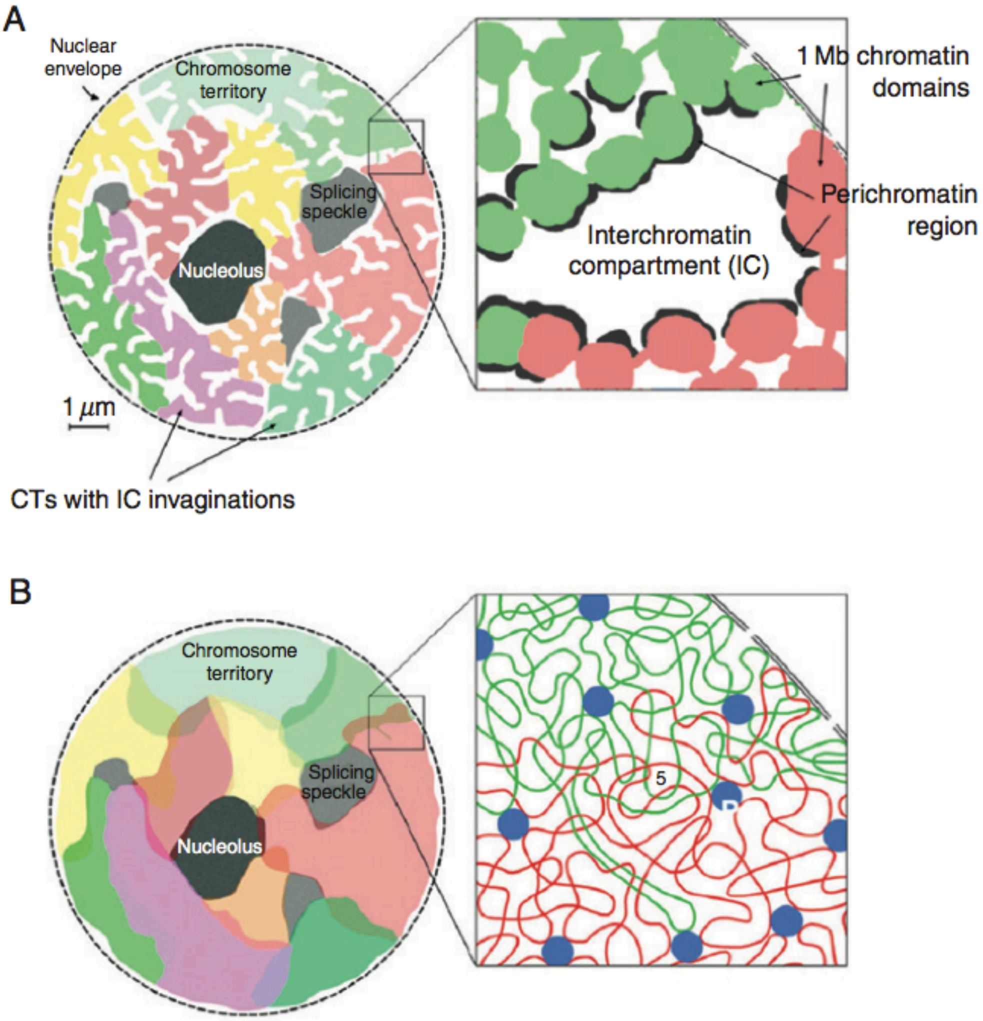

Figure 1-3: Comparison of the CT-IC versus the ICN model.

a, The CT-IC model hypothesizes that CTs are permeated by chromatin-free channels, the so-called interchromatin space (IC), depicted in white. The CT surfaces consist of decondensed chromatin, termed ‘perichromatin region’, where genes loop out into the IC to be transcribed. The CT interior is more condensed and transcriptionally less active, because the high condensation state acts as an accessibility barrier. The zoom-in on the right shows the sub-chromosomal organization of chromatin hypothesized by the CT-IC model. CTs are divided into sub-chromosomal domains ~1 Mbp in size. **b,** The ICN model hypothesizes near homogeneous intermingling of chromatin fibers, within the same CT, but also between neighboring CTs. The mode proposes a homogeneous chromatin density distribution within the CT. In the ICN model the surface and interior regions of CTs have the same chromatin density. Dynamic associations to the nuclear periphery, nuclear bodies and also active transcription (blue dots in the zoom-in) is postulated to be involved in maintain chromatin structure. Figure modified from (Rouquette et al., 2010).

The main aspect in which the ICN model contradicts the CT-IC model is the question whether there are fundamental differences between the inside and outside of CTs (reviewed (Branco and Pombo, 2007)).

1.1.2.3 The Role of the Nuclear Periphery in Chromatin Organization

In metazoans the double-membraned nuclear envelope contains the nuclear pores and is lined by the nuclear lamina (NL), a nucleoskeletal structure underneath the inner nuclear membrane, which not only provides mechanical stability to the cell nucleus, but also contributes to chromatin organization. The NL is composed of a 30-100 nm thick fibrillar network of intermediate filaments (Lamins) and additionally contains a range of membrane-associated proteins. Four Lamin proteins are expressed in mammals: 2 splice variants of the LMNA gene, namely Lamin A and C; additionally Lamin B1 and Lamin B2 encoded by the LMNB1 and LMNB2 genes (reviewed in (Amendola and van Steensel, 2014) (Wilson and Foisner, 2010)).

The nuclear periphery is an important structuring element for compartmentalizing chromatin in the nucleus. It anchors heterochromatin and therefore helps the spatially separate the two main chromatin compartments in higher eukaryotes. In human cells, about 40% of the genome associate with the nuclear lamina. This number was estimated using the DamID approach. The bacterial DNA adenine methyltransferase (Dam) fused to lamin B1 is used as a reporter system, which adenine methylates all chromatin regions in close physical contact to the nuclear periphery. By genomic mapping of adenine-methylated DNA one receives NL-chromatin interaction maps.

In general, the nuclear periphery appears to be a transcriptionally more repressive environment, (reviewed in (Lanctot et al., 2007)). Transcriptional shut-down of several reporter genes was observed upon gene repositioning to the NL (Reddy et al., 2008). Despite this general trend, not all genes contacting the nuclear lamina are transcriptionally silenced. There are examples of NL targeted reporter genes, which do not change transcription status upon relocation (Kumaran and Spector, 2008). In yeast, there are examples of transcriptionally active genes at the nuclear periphery.associated with nuclear pore complexes (reviewed (Brown and Silver, 2007)). Positioning close to the nuclear periphery may therefore rather serve to facilitate the regulation of gene activity (repression) than to repress transcription directly.

A major question is how chromatin is targeted to the nuclear envelope. There is evidence for both DNA sequence-specific (Zullo et al., 2012) and core-histone mediated anchoring mechanisms (Taniura et al., 1995). It has been suggested that Lamins can bind chromatin directly (reviewed in (Prokocimer et al., 2009)), but chromatin tethering is also mediated by proteins inserted into the inner nuclear membrane (reviewed in (Amendola and van Steensel, 2014)). Much effort has been put into identifying the proteins in charge of chromatin tethering. The proteome at the nuclear periphery is very diverse with many cell-type specific and many poorly characterized proteins. Well-studied examples include the LEM-domain family (e.g. Emerin, Lap2β, MAN) or lamin B receptor (LBR) and BAF. Emerin and Lap2β can directly bind the chromatin-silencing enzyme HDAC3 (histone deacetylase 3) (Demmerle et al., 2012). This is an example of how the nuclear envelope serves both as a chromatin tethering and silencing platform. The inverted chromatin architecture in mouse rod cells described earlier is related to absence of both LBR and Lamin A/C, ectopic expression of LBR reverts the inverted chromatin architecture in mouse rod cells (Solovei et al., 2013), suggesting that LBR is also involved in heterochromatin tethering (Solovei et al., 2013). An example demonstrating that epigenetic marks are involved in chromatin tethering is H3K9 methlyation. It has been found that depletion of H3K9 methylation in mouse cells destabilizes both heterochromatin and NL integrity (Pinheiro et al., 2012). Heterochromatin Protein HP1, has been shown to bind to methylated lysine 9 in histone 3 (H3K9) and trigger a positive feedback loop, by recruiting H3K9 methyltransferase, which reinforces the repressive H3K9me2/me3 marks (Jacobs et al., 2001; Lachner et al., 2001)

1.1.2.4 The Nucleolus

Nucleoli are the largest nuclear bodies in the cell nucleus. In mammalian cells they are about 0.5-2 μm in size and a nucleus typically contains 1-10 of them. They form around tandem repeats of rDNA genes, known as the nucleolar organizing regions (NOR), and are the dedicated sites of ribosomal RNA synthesis and ribosome subunit assembly.

Similar to the nuclear periphery, the nucleolar surface is also known to anchor chromatin, both structures have been aptly termed 'velcro for heterochromatin' (Padeken and Heun, 2014). In single cell studies looking at chomatin-lamina interactions, it was observed that heterochromatin domains located at the nuclear periphery in mother cells, preferentially either return to a peripheral location or change to a perinucleolar position in daughter cells (Kind et al., 2013). Two general mechanism of nucleolar chromatin targeting have been described. One mechanism works via specific DNA sequences. Centromeric satellite repeats are enriched in the genome fraction which associates with nucleoli (Németh and Längst, 2011), and there is evidence that the repeat RNA could be involved in targeting centromeres to nucleoli (Wong et al., 2012). The second known anchoring strategy of chromatin to the nucleolus is mediated by proteins that bind in a DNA sequence unspecific manner. An example is the CCCTC-binding factor (CTCF), which can tether chromatin to the nucleolus surface by binding to nucleophosmin, as demonstrated in nuclei of human K562 cells (Yusufzai et al., 2004). However, the complete protein inventory that tethers chromatin to the nucleolar surface is yet to be identified.

Besides nucleoli, higher eukaryotes contain many additional nuclear bodies. These are focal assemblies of proteins and also RNAs, located within the interchromatin space, which are dedicated to specific nuclear processes (reviewed in (Mao et al., 2011; Spector, 2006)). Nuclear Speckles for instance are focal hotspots for pre-mRNA splicing factors (Spector and Lamond, 2011). Paraspeckles and PML bodies are involved in the regulation of gene expression in response to external cues (Fox and Lamond, 2010), and Cajal bodies are involved in snRNAs and snoRNAs modification, assembly and trafficking (Morris, 2008). There is evidence that these smaller nuclear bodies can contribute to shaping local chromatin conformation. Nuclear speckles for instance have been suggested to serve as dynamic hubs for transient chromosomal interactions (reviewed in (Mao et al., 2011)).

1.1.3 Domain Organization of Chromatin

The internal organization of chromosome territories is still under debate. Recently, different genome-wide mapping approaches, including chromatin-proteome profiling, epigenetic profiling and chromosome conformation capture and replication timing profiling have revealed a striking domain organization of higher eukaryotic genomes into sub-megabasepair sized domains (reviewed in (Bickmore and van Steensel, 2013; Sexton and Cavalli, 2015; van Steensel, 2011)). These findings nicely complement older discoveries from microscopy studies on single cells, which have characterized stable and spatially distinct native subunits of chromatin, the so-called replication foci.

1.1.3.1 Replication Foci

Starting at the onset of DNA-synthesis phase (S-phase), one finds thousands of focal speckles all across the nucleus containing nascent DNA and the assembled molecular machinery to replicate DNA. These structures were first discovered in a microscopic study and named replication foci (RF) (TAYLOR, 1960).

Each mammalian replication focus co-replicates a contiguous stretch of DNA, sub-Mb in size during S-phase. DNA replication initiates synchronously from multiple points within this DNA segment. In budding yeast, replication originates from specific 11 bp consensus sequences, so called replication origins. In mammalian cells replication origin sequences vary and different sets of origins are activated in each new cell cycle (Gilbert, 2012).

The replication machinery assembles in a self-organizing process. Freely diffusing replication factors are recruited to a group of replication origins, where replication is initiated simultaneously (Sporbert et al., 2002). Starting from each replication origin, replication forks move often times bi-directionally along the DNA fiber (Huberman and Riggs, 1968), replicating it at a speed of 1-2 kb per minute (Jackson and Pombo, 1998; Técher et al., 2013; Palumbo et al., 2013). These bi-directionally growing structures are called replicons. Examples of replicons from isolated chromatin fibers visualized using EM are shown in Figure 1-4. Within approximately an hour, all replication forks of a RD have met and a genomic segment of a few hundred kbs is fully replicated (Ma et al., 1998) (Jackson and Pombo, 1998).

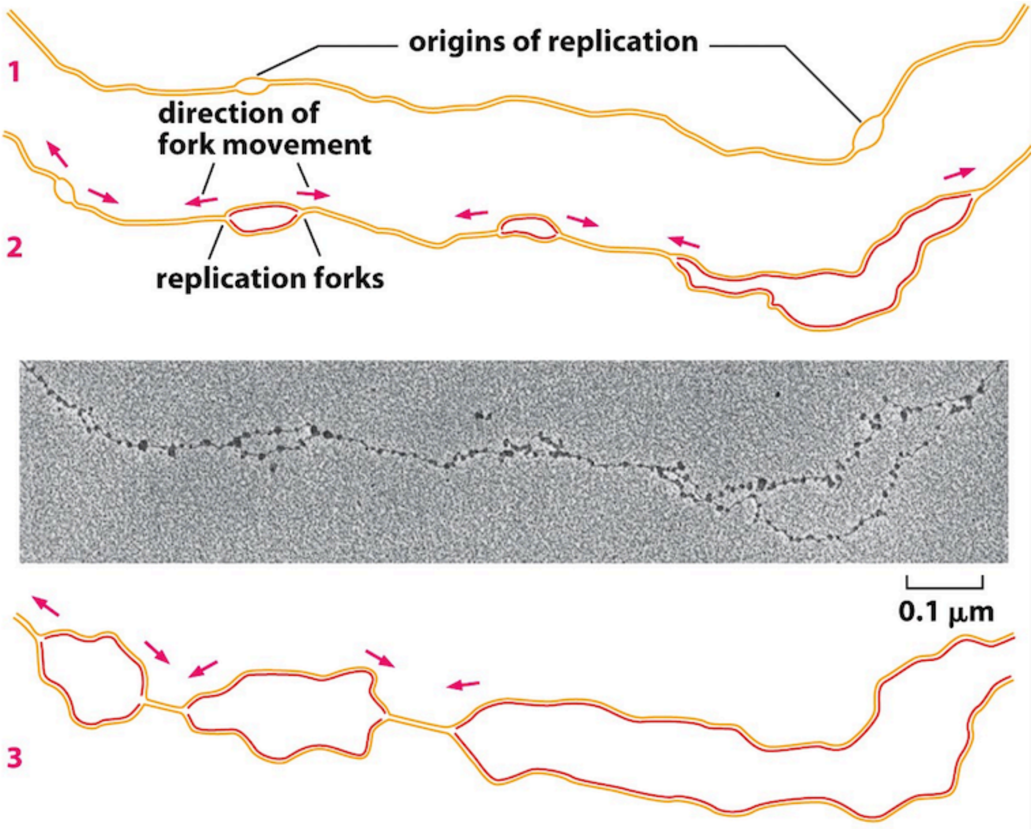

Figure 1-4: Progression of DNA replication in three neighboring replicons. The electron micrograph in the center of the panel shows an isolated and unraveled 10 nm bead-on-a-string chromatin structure, which was undergoing replication. The cartoon panels 1-3 depict a time-course of DNA replication. Starting from the replication origins, replication proceeds bi-directionally, three synchronously replicating replicons are shown. Image adapted from Essential Cell Biology, Fourth Edition 2013 by Garland Science.

Much of what is known about replication foci is based on studies from molecular DNA combing experiments. This experiment works by feeding living cells with a tagged nucleotide-precursor for a defined time while the cells replicate their DNA.

Later chromatin is isolated from these cells and single labeled DNA fibers are linearly stretched out on glass-slides. This allows to assess parameters such as replication speed, number of origins/replicons per replication focus and the time necessary to replicate a complete RF. Earlier studies used radioactively ([^{3}H]thymidine) labeled nuclei (Huberman and Riggs, 1968), while newer studies use fluorescently labeled nucleotides (Jackson and Pombo, 1998) and more sophisticated DNA stretching techniques, that allows more controlled stretching DNA fragments (Bensimon et al., 1994). See Figure 1-5 for examples of single replication-labeled DNA-molecules, which were stretched out for combing analysis.

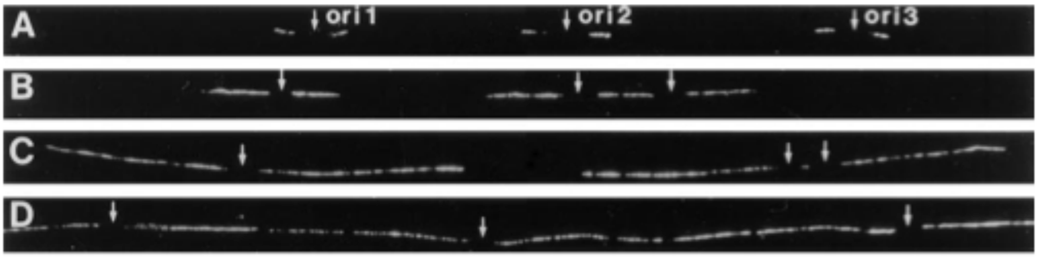

Figure 1-5: Molecular combing of single DNA molecules.
Depicted are fluorescently labeled segments of DNA, stretched out linearly on a glass slide. The labeled sequences are shown in white over black background. The length of the labeled sequence increases with length of the BrdU-pulse. a, BrdU was incorporated for 5 minutes, only short segment labeld, three replicons are shown. b, 20 minutes of BrdU; the labeled segment is longer. c, 40 minutes of BrdU. d, 60 minutes of BrdU, a contiguous stretch of the DNA fiber is completely labeled. Image adapted from (Jackson and Pombo, 1998)

Figure 1-6 displays fluorescently labeled RF in a mammalian nucleus during euchromatin replication. When euchromatin replication is completed, the replication foci move to the nuclear periphery and around the nucleoli to replicate heterochromatin. This leads to a characteristically changing pattern of replication foci in the nucleus from early to late S phase (Ferreira et al., 1997), which is evolutionarily conserved (Zink et al., 1999). With increasing detection sensitivity of fluorescence-based microscopy, the counts of replication foci active in mammalian nuclei at a time also keep increasing. The estimates range from a few hundreds to several thousands at any time during S-phase in mammalian nuclei (Baddeley et al., 2010; Cseresnyes et al., 2009; Jackson and Pombo, 1998; Ma et al., 1998).

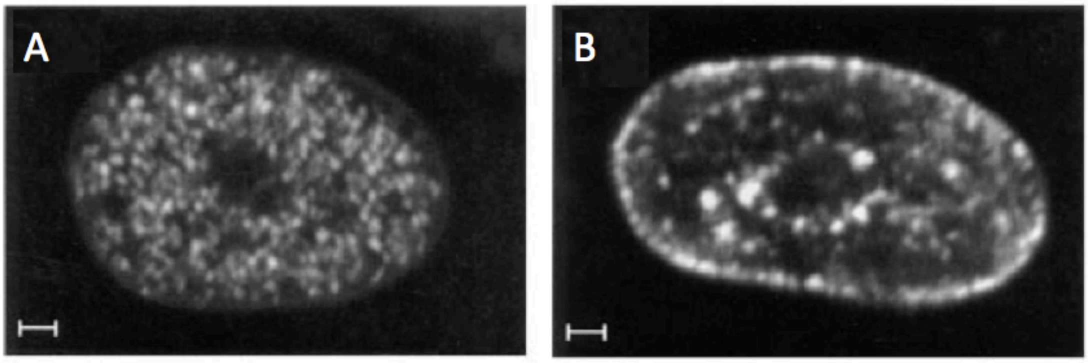

Figure 1-6: Replication foci in the midplane of a mammalian interphase cell nucleus are shown. Cells were labeled by BrdU replication labeling.

a, The cell was imaged in early S-phase, during replication of euchromatin across the nucleoplasm. **b**, The cell was imaged in mid S-phase, during replication of heterochromatin close the nuclear periphery and around nucleoli, scalebar 1 µm. Figure from (Ferreira et al., 1997).

When the genome-duplication at one replication focus is fully completed, the replication machinery disassembles and subsequently newly assembles at a spatially and genomic neighboring site. In this way chromatin replication proceeds in what has been called a ‘domino’-like fashion (Leonhardt et al., 2000; Maya-Mendoza et al., 2010). The molecular mechanisms that preferentially recruit new replication machinery to assemble close to the previously replicated RF are not yet understood (reviewed in (Chagin et al., 2010; Rhind and Gilbert, 2013)).

Several studies were able to demonstrate that the chromatin domain gathered in a replication focus is stable throughout the cell cycle. (Sparvoli et al., 1994),(Zink et al., 1998),(Ma et al., 1998; Sadoni, 2004). Individual replication foci correspond to spatially organized replicon clusters harboring several synchronously firing replicons and comprising on average about 500 kb of DNA (Jackson and Pombo, 1998).

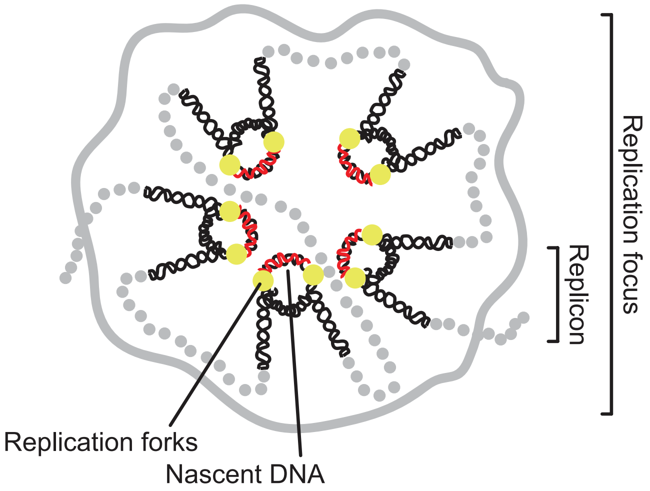

Figure 1-7: Organization of a Replication Focus
The cartoon illustrates a group of synchronously replicating replicons forming a replication focus (RF). Replication forks are depicted in yellow, nascent DNA in red.

It has been shown that DNA organized into distinct replication domains during S-phase remains in this conformation long after S-phase. Additionally, it was observed in several studies that position and replication timing of RFs are maintained during several subsequent cell divisions. (Zink et al., 1998). In a study by Sadoni et al. 2004, the authors could observe co-localization of neighboring RF during early and late stages of S-phase using pulse-chase-pulse double color RF-labeling. Their data demonstrated that RFs, which had replicated synchronously in a mother cell, in turn synchronously initiated and co-replicated their RD in the respective daughter cells at the corresponding S-phase stage (Sadoni, 2004).

1.1.3.2 Replication Domains

Using replication-timing profiling it is possible to investigate the temporal program of replication. It allows assessing at which stage in S-phase each genomic region replicates. The idea is to sort cells into different S-phase stages chromatin content and then to map the regions of nascent replication. There are two different protocols how to perform this experiment. The first strategy is the BrdU-immunoprecipitation approach. It requires exposing replicating cells to a ~1h pulse of BrdU, which is a nucleotide-precursor tagged to a bromide-group. The cells readily incorporate BrdU into their DNA backbone while replicating their DNA. Then, after the BrdU-pulse, the DNA is stained and fluorescence-activated cell sorting (FACS) sorted into different S-phase stages (e.g. early, mid and late S-phase) stages according to chromatin content. The nascent DNA fraction in these samples contain BrdU can thus be immunoprecipitated and be mapped using micro-arrays or sequencing. The second method is the so-called S/G1 method and can be performed on unlabeled cell population. Cells are sorted into a G1-phase population and a S-phase fraction. In the G1-phase cells, the copy numbers of all genomic sequences are equal. In the S-phase cells, copy numbers of genomic sequences are proportional to how early the sequences replicates. Thus, the replication program during S-phase can be profiled by lining up the results of S/G1-ratios across the genome for each S-phase fraction (Gilbert, 2010; Hansen et al., 2010). An example of the results of replication timing profiling is shown in Figure 1-8.

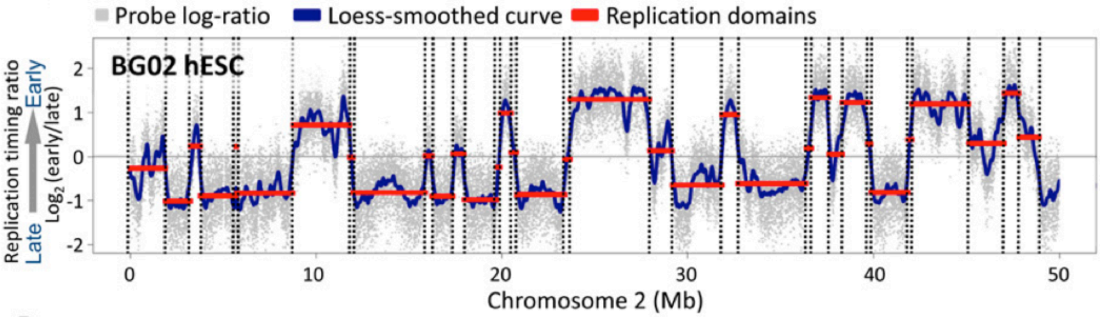

Figure 1-8: Exemplary result of replication timing profiling.
50 Mb region on human chromosome 2 is profiled for replication timing. The panel shows hundreds of kb to several Mb-sized alternating segments of early, mid and late replicating DNA. The black dotted lines delineate the position of replication domain boundaries, image modified from (Ryba et al., 2010).

In high-resolution replication timing profiles, where S-phase is well sampled, it appears that replication timing does not simply divide the genome into early versus late replicating regions. Instead one finds many more than only two replication time zones (Hansen et al., 2010). Importantly, replication-timing profiles allow the annotation of zones of stable replication timing, the so-called replication domains. Replication domains are the genomic equivalent of replication foci observed by microscopy. The boundaries between genomic neighboring replication domains are demarcated by a sharp transition in replication timing and they are referred to as timing transition regions (TTRs).

Comparison of high-resolution replication timing profiles with DNase I hypersensitivity maps revealed that replication typically initiates from chromatin domains with highly accessible chromatin, containing high frequencies of DNase I cutting sites (Hansen et al., 2010). It was also shown that replication timing correlates more strongly with chromatin accessibility than with gene expression (Hansen et al., 2010). Replication timing is well conserved during evolution. When comparing syntenic chromosome regions of mouse and men for their replication timing profiles, a striking degree of overlap is found between the TTRs. (Hiratani et al., 2008; Ryba et al., 2010). For about 50% of the genome, replication timing was found to be cell-type specific (Ryba et al., 2010; Schwaiger et al., 2009). It was found that early-replicating domains contain many active genes, while late-replicating domains contain mostly transcriptionally silent domains (Hiratani et al., 2008; Schwaiger et al., 2009). This finding agrees well with the observation described from microscopy experiments that euchromatin replicates early in S-phase, while heterochromatin replicates later in S-phase (Schermelleh et al., 2001; Zink et al., 1999). When lining up replication timing profiles with respective epigenetic profiles it was evident that late replicating domains in the human genome lack active histone marks and are instead enriched for the repressive mark H3K9me2.

The importance of chromatin domains such as replication domains as the basic structural units of chromatin is exemplified in a study of trisomy 21. The transcriptome of fetal fibroblasts of monozygotic twins was studied. One of the twins suffered from trisomy 21, while the other was not affected. This allowed studying the impact of trisomy 21 on the transriptome without additional genetic variations. The analyses revealed domain-wise differential expression between the twins. These domains showed strong overlap with replication domains. All genes within a miss-regulated domain were either up-or downregulated in the trisomy background consistent with the idea that subchromsomal domains act as a common microenvironment for the regulation of the genes they harbor (Letourneau et al., 2014).

1.1.3.3 Topologically Associating Domains (TADs)

The development of chromosome-conformation-capture (3C)–based technologies now allows for the investigation of three dimensional chromosome organization using sequencing technologies. The technique requires cell fixation with formaldehyde to cross-link chromatin regions in close physical proximity. Then chromatin is subjected to restriction digestion, and the digestion fragments are allowed to form ligation products with neighboring fragments and the ligation products are DNA sequenced and mapped back to the genome. There are multiple variations of this concept, which differ in the way ligation products are isolated and amplified for sequencing (reviewed in (de Laat and Dekker, 2012; de Wit and de Laat, 2012)).

The concept of 3C can be realized in different technical adaptation to investigate different scales of 3D chromatin organization with different resolution. The original 3C-technique is only used on a small scale to investigate interactions between a pair of selected loci (Dekker et al., 2002). Chromosome conformation capture on-chip (4C) is used to map genome-wide interactions of a locus of interest (Simonis et al., 2006). Chromosome conformation capture carbon copy (5C) is a multiplexed version of 3C which allows to investigate the interactions of many genomic loci in a highly-parallel fashion (Dostie et al., 2006). 5C has been used to map a contiguous 4.5 Mb-sized region of chromosome at 10-20 kb resolution (Nora et al., 2012). Hi-C allows genome-wide mapping of physical chromatin associations (Lieberman-Aiden et al., 2009), the resolution increases with sequencing depth. The first genome-wide association frequency map generated using Hi-C had low resolution of only ~1 Mb (Lieberman-Aiden et al., 2009), ever since the resolution has increased significantly in more recent Hi-C studies and has currently reached 1 kb (Dixon et al., 2015; 2012; Jin et al., 2013; Rao et al., 2014). The results of 5C and Hi-C are chromatin interaction frequency heat maps over large genomic regions/ the entire genome. An example is depicted in Figure 1-9.

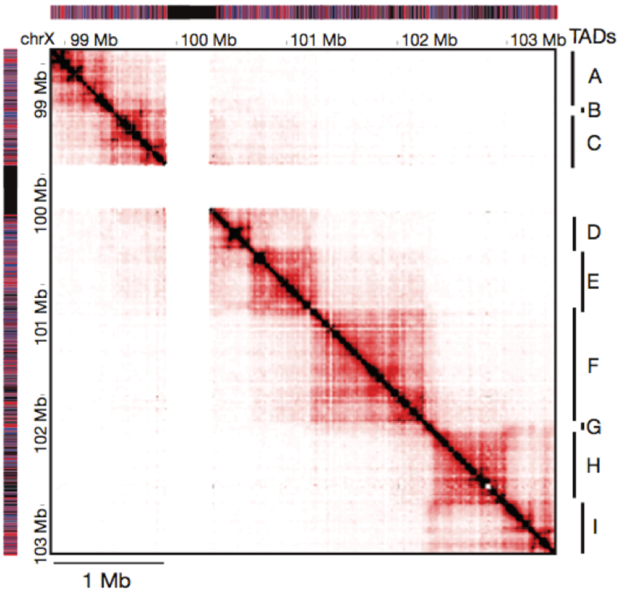

Figure 1-9: Exemplary interaction frequency map from 5C-data. Image adapted from (Nora et al., 2012).
A 4.5 Mb-sized region on the mouse X chromosome was mapped for physical contacts. The darker the red color on the heatmap, the higher the contact frequency measured between respective genomic loci. The TADs identified are highlight on the right of the panel.

Currently, high-resolution 5C and Hi-C datasets are available for *drosophila* cells and mammalian cells (Dixon et al., 2012; 2015; Nora et al., 2012; Sexton et al., 2012). A striking observation in these datasets is that 90% of the genome is covered by long linear domains of enhanced local interactions, termed topologically associating domains (TADs). These domains are flanked by short segments of seemingly non-interacting segments, termed TAD boundaries. The median genomic size of TADs found in humans is ~800 kb and ~100 kb in flies (Dixon et al., 2012; Sexton et al., 2012).

FISH was used to explore the packing of DNA in TADs in intact nuclei. It could be shown that chromosomal loci within the same TAD are closer in 3D compared to chromosomal loci in neighboring TADs with the same linear distance from each other (Nora et al., 2013).

The majority of boundary regions between TADs were estimated to be below 50 kb in human cells (Dixon et al., 2012), they were enriched in CTCF-binding sites, transfer RNA genes and SINE elements, which all can have insulator function for transcriptional regulation. However, more than 75% of total CTCF-sites are found within TADs, suggesting that TADs may contain substructure and subdomains (Dixon et al., 2015). Boundaries were also enriched in promotors of housekeeping genes (Dixon et al., 2012).

Insulator proteins and active transcription associating to TAD boundaries was also found in flies (Hou et al., 2012; Sexton et al., 2012). Boundary regions seem to be essential to chromosome organization. The deletion of a boundary region on the mouse chromosome X disrupted the topology of the adjacent TADs severely (Nora et al., 2012). A recent study could further demonstrate that structural variations at TAD boundaries can distort neighboring TADs, which can in turn result in de novo enhancer-promoter interaction leading to dramatic phenotypes in limb development (Lupiáñez et al., 2015).

TAD boundaries between mouse and human are highly conserved, suggesting that their positioning is non-random (Dixon et al., 2012). Even though cell-type specific differences can be found, TAD boundaries of neural cells compared to lymphocytes still show a high degree of overlap. Interestingly, the regions where TAD-positioning is different between cell types correlate with differentially transcribed regions.

TADs often times align perfectly with domains of active or repressive epigenetic marks (Nora et al., 2012). This raised the question whether the epigenetic state of a genome region dictates TAD positioning/ local chromatin structure. By mapping

TADs in Eed and G9a knockout-mice respectively, it was demonstrated that the absence of neither and are required for H3K9me2 nor H3K27me3 compromised TAD integrity, leading the authors to conclude and that epigenetic marks are established downstream of TAD formation(Nora et al., 2012).

1.1.3.4 The Replication Domain Model

In a recent study, replication timing profiling of 31 cell lines from mouse and human was performed in the framework of the ENCODE-project (ENCODE Project Consortium et al., 2012). The authors compared the collectively found TTRs from all 31 cell lines to the annotated TAD boundaries from HiC experiments. They were able to uncover a striking overlap of TTR with TAD boundaries, suggesting that TADs and the stable units of replication-timing regulation are one and the same chromatin structure (Pope et al., 2014).

The authors state that is was crucial to the success of the experiment to combine annotations TTRs and TAD boundaries from all 31 cell lines. Looking for the overlap of boundaries just within single cell lines does not show the overwhelming correspondence, since technical limitations lead to incomplete boundary annotation for both HiC and replication timing assays. Adjacent TADs with similar replication timing for instance can obscure correct boundary identification (Pope et al., 2014). Earlier attempts to quantify the correspondence between RDs and TADs have ran into exactly the same problem, namely not being able to unambiguously resolve a large enough fraction of both RDs and TADs, lowering the observed overlap. Even though the studies were able to find a strong correlation between 3D chromatin structure and replication timing domains, they were not yet able to reveal the direct correspondence of RDs to TADs (Letourneau et al., 2014; Moindrot et al., 2012; Ryba et al., 2010). The recent more comprehensive data however strongly supports the so called ‘replication-domain model’, which is a unifying model as it reconciles many of the older and more recent findings about linear and three dimensional domains as stable subunits of chromatin organization. A scheme of the model is shown in Figure 1-10. Importantly, the ‘replication-domain model’ establishes the RD as the central stable subunit of higher order chromosome organization (Pope and Gilbert, 2013), which consists of DNA sequences within typically no more than one megabase of DNA that are physically closely associated in 3D space by looping and backfolding and share the same replication timing and transcriptional regulation.

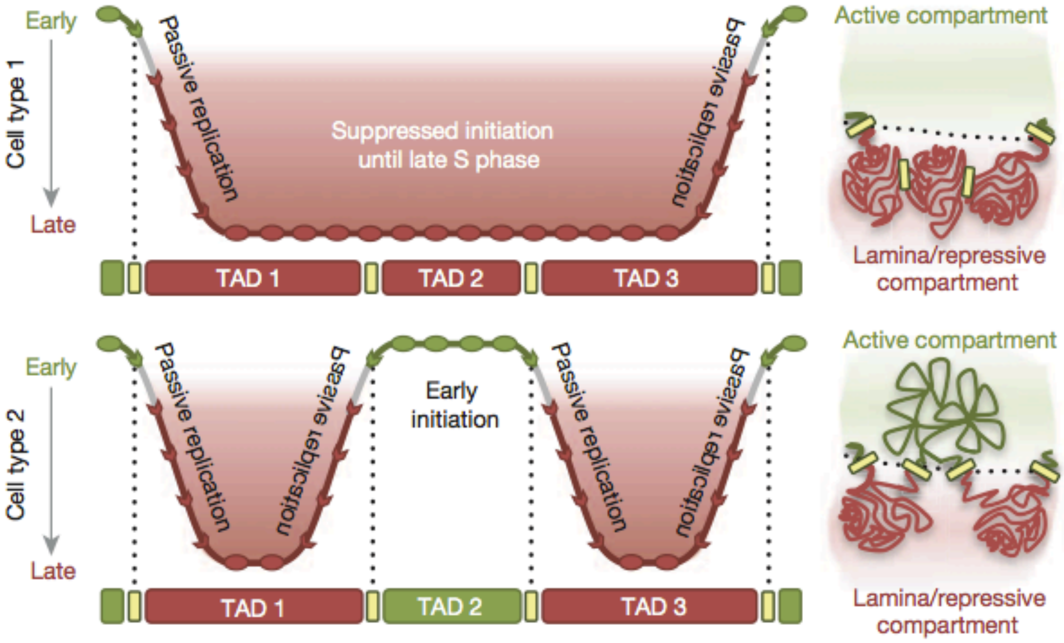

Figure 1-10: The replication domain model.
The top and lower panels of the cartoon compare the same genomic region within 2 different cell types. While the overall TAD structure between the two cells is conserved, TAD2 has changed replication timing and from a repressed into an active state. In the top panel, all 3 TADs have similar late replication timing, therefore no TTR can be picked up for TAD2. In contrast, the cell in the lower panel shows clear TTR regions flanking TAD2, which line up perfectly with the TAD boundaries (marked in yellow).

1.1.4 Chromatin Compaction

The compaction state, or DNA/nucleosome concentration per unit volume, is one of the basic features of chromatin organization. Local chromatin compaction has been suggested to constitute an accessibility barrier, which is considered crucial for essential nuclear processes, such as gene transcription, DNA replication and DNA damage repair. In order to accommodate these processes, the cell nucleus needs to be able to regulate chromatin compaction. How delicate the right balance of local chromatin compaction is, is revealed in severe diseases associated with aberrant chromatin compaction, such as cancer (reviewed in (Chi et al., 2010)).

The lower compaction state of euchromatin compared to dense heterochromatin has been described for many decades. Fluorescence microscopy of DNA-intercalating dyes or GFP-tagged core histones typically reveals a dense rim of heterochromatin underneath the nuclear envelope and surrounding the nucleoli of living cells. Densely stained patches of heterochromatin in the nucleoplasm can also be clearly distinguished from less densely packed euchromatin on electron micrographs. Heterochromatin is reported to be less accessible for larger diffusing particles compared to chromatin at the nuclear interior, indicating a smaller effective pore size (Bancaud et al., 2009; Görisch et al., 2005).

Transcriptional activity is often associated with lowered chromatin compaction. The most striking example are probably the actively transcribed regions of *Drosophila* polytene chromosomes. These regions expand visibly into so-called chromosome puffs. They appear as fluffy, seemingly uncoiled regions of chromatin. Other examples include the large-scale unfolding of chromosomal regions upon artificially induced transcriptional hyperactivation (Tumbar et al., 1999).

A prominent mechanism participating in the dynamic regulation of chromatin compaction state involves covalent histone modifications. The enzymatic modifications primarily affect the N-terminal histone tails and they include modifications including methylation, acetylation, phosphorylation and ubiquitination. They are known to both directly impact chromatin packaging by affecting binding affinities between modified histones and DNA and also to be involved in signaling to recruit further proteins factors (reviewed in (Strahl and Allis, 2000)). Additional proteins directly associated with maintenance of local chromatin compaction include linker histone H1, which impacts nucleosome stacking (Francis, 2004) and Polycomb Group (PcG) proteins (Hizume 2005), such as PRC1 which is required to maintain the compacted state of transcriptionally silent Hox loci in mouse embryonic stem cells.

Genome-wide chromatin compaction can be assessed using a sedimentation assays on long chromatin fibers. The rationale is that slow sedimentation indicates more decondensed structures compared to fast sedimenting fibers. Open chromatin structure has been reported to correlate with high gene density (Gilbert et al., 2004). A remaining question is the degree of structural conservation in the sedimentation assay, since it is performed on isolated chromatin fibers *in-vitro*. It is important to distinguish chromatin compaction from chromatin accessibility. Even though these two features are often times correlated, they represent distinct parameters of chromatin organization. While compaction addresses the sheer physical packing density of DNA or nucleosomes, accessibility refers to the availability of certain genomic regions for binding proteins, which can also be locally regulated e.g. by chromatin remodelers. Accessibility is for instance measured in the DNase I hypersensitivity assay, where cutting sites are mapped in chromatin samples exposed to DNase I digestion. The frequency of cutting sites found are considered to directly correlated with accessibility of genomic regions (Weintraub and Groudine, 1976).

A new avenue for quantifying chromatin compaction has opened up with the advent of 3C-based technologies introduced previously in chapter 1.1.2. The distance-scaling factor, which describes how quickly interaction frequency between distal genomic segments decay with increasing linear distance, is interpreted as a measure of chromatin compaction in some models (Imakaev et al., 2012; Lieberman-Aiden et al., 2009). In *Drosophila,* transcriptionally repressed genomic domains show a lower scaling factor compared to actively transcribed regions (Sexton et al., 2012), which has been interpreted as a reflection of the higher compaction level (Bickmore and van Steensel, 2013). However, the results from chromatin conformation capture based experiments do not always match up with FISH measurements of physical proximity, which is the standard procedure to validate 3C-based experiments (Moindrot et al., 2012; Nora et al., 2012). The at times contrasting results, have been discussed in previously reviews (Bickmore and van Steensel, 2013) and has been specifically addressed in a recent study investigating the compaction of the Hox locus using both chromosome conformation capture and FISH (Williamson et al., 2014). There are both conceptual and technical difficulties when attempting to translate 3C-based association frequencies into physical 3D distances, which will remain a future challenge in interpreting chromosome conformation capture data (de Laat and Dekker, 2012; Tanay and Cavalli, 2013).

New experimental approaches to measure local chromatin compaction in single cells are needed. Accessibility and structure of eu- and hetrochromatin has for example been assessed by imaging of diffusing inert probes inside live nuclei (Bancaud et al., 2009). .An additional promising approach was presented in a recently published study, which quantified histone density in pluripotent and differentiated cell nuclei using super-resolution microscopy (Ricci et al., 2015). In the results chapter 3.1.3 of this thesis, I present the results of a novel experimental approach to address local compaction of subchromosomal domains using super-resolution microscopy.

1.1.5 Chromatin Dynamics

1.1.5.1 Long Range Chromatin Movements

The phenomenon of actively transcribed genes found located outside/ on the surface of their respective CTs has been observed in numerous studies on fixed cells (Mahy et al., 2002; Volpi et al., 2000) (Williams et al., 2002). This has been interpreted as genes ‘looping out’ of CTs to be transcribed. To my knowledge there are only two studies, which have observed directed movement of genomic loci over several micrometers inside the nucleus in live-cell experiments. The study by Chuang et al. from 2006 has observed directed long-range movements of an inducible transgene from the nuclear periphery to the nuclear interior (up to 5µm) upon transcriptional activation (Chuang et al., 2006). In 2007 Dundr et al. made a similar observation, they described directed movement of a transgene array towards the Cajal body (up to 3µm) upon induction of transcription (Dundr et al., 2007). Both studies found indications that nuclear actin and myosin are required for these movements. Long nuclear filaments of actin have not been observed in mammalian nuclei though, the role of nuclear actin is still controversial. It has been speculated, but not experimentally validated that movements could be driven by transiently polymerizing short actin filaments, which have escaped microscopic observation so far (reviewed in (Kapoor and Shen, 2014; Pederson and Aebi, 2005)).

1.1.5.2 Chromatin Diffusion

1.1.5.2.1 Diffusional Behavior of whole Chromosome Territories

A study looking at the dynamic behavior of entire CTs has found Brownian diffusion-like motion at very slow rates. Mutual diffusion rates of foci from different territories were found to be higher than mutual diffusion rates of foci within the same territory

(Bornfleth et al., 1999). Even though CTs can be found in variable morphologies, from e.g. rather flat to almost spherical, the morphology of each CT is stable in interphase. Once fully decondensed after mitosis, CT morphology is almost unchanged over the time-coures of several hours (Edelmann et al., 2001). The authors could also observe differences in Brownian diffusion rates of CTs between different cell lines. CTS of a neuroblastoma cell line show 2-fold faster diffusion compared to Hela cells (Edelmann et al., 2001). It was further shown that CT morphology once established in late G1-phase is stable after inhibition of transcription, histone deacetylation or chromatin remodeling (Müller et al., 2010).

1.1.5.2.2 Subchromosomal Chromatin shows Rapid Constrained Diffusion

First experiments investigating subchromosomal chromatin mobility were FRAP experiments. Nuclei stained with DNA-intercalating dyes were photobleached (diameter of bleached region 800 nm). After the bleaching, the time-course of fluorescence recovery in the bleached region was analyzed. The investigators observed incomplete fluorescence recovery in this area and concluded that chromatin must be immobile (Abney et al., 1997). Later directly tracking of chromatin GFP-labeled genomic loci and Topoisomerase II-foci in yeast and fly cells allowed to investigate chromatin motion on a smaller scale (below 300nm), inaccessible to FRAP due to the spatial dimensions of the bleaching spot. Direct tracking of subchromosomal loci revealed constrained diffusional motion, insensitive to metabolic inhibitors (Marshall et al., 1997).

A study by Heun et al from 2001 investigated four GFP-labeled chromosome loci in yeast and found both early and late replicating loci to undergo diffusive movements in G1 which slowed down in S-phase, through a replication-dependent mechanism. The authors could also show that telomere and centromere movement was more constrained and independent of replication (Heun et al., 2001).

A high resolution (30 ms) tracking study of artifial genomic loci (lacO) in mammalian cells has reported short, seemingly directional jumps of ~150 nm lasting only 0.3-2s in between longer periods of constrained diffusion. The jumps were sensitive to ATP-depletion. Two relatively close-by loci (<2 μm) did not show correlated jumps (Levi et al., 2005). The nature of these jumps is still elusive, whether they reflect transcriptional activity or spontaneous chromatin unfolding as the authors have suggested, still remains to be investigated by future studies. Recently, it was demonstrated that the CRISPR/Cas9 system can be used to tag not only repetitive elements in telomeres but also single coding genes in living cells (Chen et al., 2013). Likely, this technology will be important for studying chromatin dynamics of specific loci in the future.

1.1.5.2.3 Role of Nuclear Structure on Chromatin Dynamics

A study by Chubb et al. in 2002 reported that subchromosmal loci close to the nuclear periphery and nucleoli are immobile in mammalian cells. The authors tagged several genomic loci with ectopic arrays of bacterial lacO sequences, which are visualized by the co-expressed GFP-fused lac repressor protein that binds to the arrays. The authors tracked the movement of these loci over time and found that loci at the nuclear periphery and around nucleoli were significantly less mobile than loci in the nuclear interior. They attributed this to tethering or steric confinement (Chubb et al., 2002). This result is consistent with an experiment, studying the dynamics of early and late replication foci. It was found that late replicating chromatin located at the nuclear periphery and around nucleoli showed reduced diffusion rates in comparison to early replicating foci (Pliss et al., 2009).

1.1.5.2.4 Inferring Properties of the Chromatin Polymer using Diffusion Data

High temporal resolution tracking data of multiple loci in yeast suggests that the diffusion of these loci agree with diffusion of a rouse chain (Albert et al., 2013; Hajjoul et al., 2013). In polymer physics, the rouse model describes a polymer consisting of beads connected by harmonic springs. It assumes that the motion of each bead is dominated by elastic interactions with adjacent beads on the chain. The rouse model does not regard contributions of the solvent in which the chain is immersed (Zimm-model) and additional geometric constraints (Reptation-Model). Tracking of mammalian telomeres spanning a time regime from of 10^{-2}–10^{4} s reveals that telomere motion can be explained by with ‚transient diffusion', which is to say that telomeres constantly undergo binding and unbinding, with a wide distribution of waiting times between binding events (Levi et al., 2005).

In a recent study (Lucas et al., 2014), the authors have tagged loci involved in V(J)D recombination in pro-B cells. During B lymphocyte development, the recombination of distal V J and D segments results in the highly diverse pool of antibodies produced by immune cells. Loci on distal V and D-J-E were fluorescently marked using TetO arrays. These arrays work according to the same principle as LacO arrays mentioned earlier. The authors observed trajectories of these loci in both pro-B and B cells, and interpreted the movement as ‚fractional Langevin motion'. This is a mode of motion displayed by particles diffusing in an environment with viscoelastic hindrance. Using modeling, the authors propose that genes and regulatory elements, bounce back and forth in a spring-like fashion' in the viscoelastic environment formed the surrounding chromatin network and that the local compaction state which can change with development, controls the frequency of encounters between distal regions oft he genome (Lucas et al., 2014).

1.2 Super-Resolution Microscopy

The invention of the microscope about 400 years ago has opened up the field of cell biology for science. Technical innovations improving the resolving power of light microscopes have ever since preceded important discoveries in this field. Today light microscopy is an essential tool for cell biologists, being the only microscopy technique compatible with routine molecularly specific labeling and live imaging.

For a long time, the conviction persisted that the resolution of optical instruments is fundamentally limited by the diffraction of light. In 1873 Ernst Abbe formalized the observation that the wavelength of light and opening angle of the objective (numerical aperture; NA see below) fundamentally limit the optical resolving power. 1896 lord Rayleigh phrased a related definition of the resolution limit. Light of a point-emitter collected through an objective does not appear as a point on the resulting image, even if optimally focused, but instead creates an interference pattern. This so-called Airy pattern consists of a bright circular central region, surrounded by concentric dark and bright rings. The intensity of the interference pattern also varies along the optical axis. The 3-dimensional interference pattern is described by the point spread function (PSF) of the imaging system. The interference is caused by diffraction of the light wave-front at the lens aperture. As a consequence of the wave-nature of light, the image forming process blurs the depicted signal. The Rayleigh resolution criterion describes that two point-like emitters spaced at lateral distances closer than $d_{xy} = \frac{0.61*\lambda}{n*\sin(\theta)}$ cannot be distinguished as two separate light sources. d_{xy} describes the distance between two point emitters, for which the central maximum of the Airy disc of one emitter meets the first minimum of the Airy disc of the second emitter. In the equation λ stands for the wavelength of light collected by the objective, n is the diffractive index of the medium and θ is the half opening angle of the cone from which photons can be collected by the objective. The term $n * \sin(\theta)$ denotes the numerical aperture (NA). In a typical example where wavelength 500 nm is collected with NA = 1.3, the lateral resolution reached is ~230 nm.

The axial resolution along the optical axis is lower than the lateral resolution; the reason for this is the geometry in which light is collected by the objective. The axial pattern of the PSF is hourglass shaped, according to the Rayleigh criterion the axial resolution is limited to $d_z = \frac{2*n*\lambda}{(n*sin\,(\theta))^2}$. In the same example ($\lambda$ = 500 nm; NA = 1.3), the axial resolution limit defined by the Rayleigh criterion is ~790 nm.

Macromolecules such as proteins are one to two orders of magnitude smaller than the diffraction limit, thus fundamental biological structures and processes are not directly accessible by conventional light microscopy. In the last two decades though, several methods have been developed allowing to resolve point emitters spaced much closer than the traditional diffraction barrier defined by Abbe. They now allow light microscopy to directly access the molecular scale. These new microscopy techniques were collectively named super-resolution microscopy.

The first approaches reaching resolution below the diffraction barrier were achieved using near-field optics (Betzig et al., 1986). Because of the limited relevance of near-field optics for intra-cellular imaging, I will only introduce far-field super-resolution microscopy methods in the following. Far-field super-resolution microscopy approaches can be grouped into two main categories. One category are excitation-patterning based methods, including structured illumination microscopy (SIM) and stimulated emission depletion microscopy (STED). The second category are single molecule localization based methods, of which the most prominent are stochastic optical reconstruction microscopy (STORM) and photo-activated localization microscopy (PALM).

1.2.1 Structured Illumination Microscopy (SIM)

SIM uses the Moiré-effect, which describes that superposition of two fine periodic light patterns results in a coarser pattern (Moiré fringes). In SIM one fine pattern is the fluorescently labeled sample and the second fine pattern is the high contrast periodic stripe pattern used for sample illumination, see Figure 1-11.

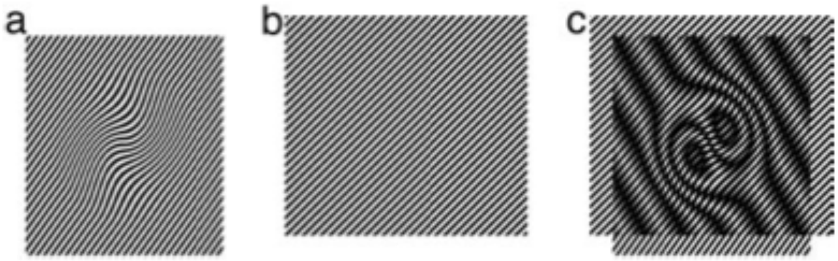

Figure 1-11: Moiré-effect used by SIM
Superposition of two fine periodic patterns **a,** and **b,** results in coarser moiré fringes **c**, Figure from (Gustafsson, 2005).

Even though the detected raw image does not contain any image features smaller than the diffraction limit, it does encode the higher resolution information. This higher resolution information can be computationally reconstructed in combination with the information about the known excitation pattern. In order to reconstruct an image with sub-diffractive resolution, it is necessary to cover a significant fraction of the higher frequency reciprocal space. Therefore information of different illumination angle and phases need to be combined. With each phase orientation and angle of the applied striped excitation pattern, a fraction of the higher frequency Fourier space can be explored, see Figure 1-12.

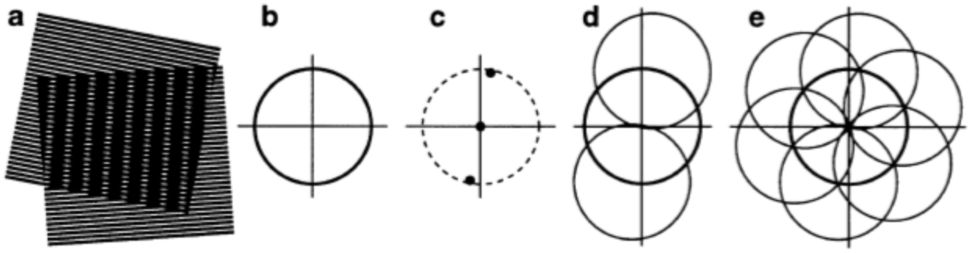

Figure 1-12: Expanding the observable region in frequency space using SIM **a,** Pattern orientation in real space. **b,** The black circle contains the observable region in Fourier space for conventional diffraction limited microscopy, circle radius is $k_{conv.}$. The origin of the coordinate system encodes low frequency information. At increasing distance from the origin are the regions of higher frequency information. X-axis and y-axis mark horizontal and vertical frequency components. **c,** A sinusoidal striped pattern in real space transforms into three bright dots in Fourier space. The illumination pattern orientation defines the position of the 2 opposing black dots in Fourier space. To retrieve information about the underlying finer structure pattern from the moiré fringes in the resulting image, one has to shift the information back in Fourier space, the direction to translate the pattern is defined by the excitation pattern orientation and the translation distance depends on the line spacing of the excitation stripe pattern used. **d,** The observable frequency region now additionally contains two higher frequency domains outside of the diffraction limited region. **e,** Using three different orientation angles of the excitation pattern, most of the frequency space $k_{SIM} = 2^* k_{conv}$ can be observed, the spatial resolution increases by a factor of 2. Figure from (Gustafsson, 2000).

To reconstruct a 2D SIM image with enhanced resolution, a series of typically 9 (for 2D SIM) or 15 (for 3D-SIM) images are taken at different phase and rotation angles of the excitation pattern of the same image window. The original SIM approach using a striped excitation pattern, with line spacing close to the diffraction resolution limit (Gustafsson, 2000), yields a two-fold lateral resolution improvement. By using an illumination pattern, which is also modulated along the optical axis, the axial resolution can also be improved by a factor of 2 in 3D-SIM (Gustafsson et al., 2008; Schermelleh et al.). The axial resolution is further improved in the I^5S setup. By

adding a second objective to the system, interference effects between two opposing objectives are used to reach ~100 nm isotropic resolution (Shao et al., 2008).
Further resolution improvement can be achieved using saturated structural illumination (SSIM) (Gustafsson, 2005). By using very high laser intensities, excitation regimes are reached where the emission rate of the fluorescently labeled sample no longer linearly responds to the illumination intensity. As a result, the effective excitation pattern contains harmonics with frequencies higher than the frequency of the periodic stripe excitation pattern. The resolution reached in SSIM depends on the excitation energy used. The higher the excitation energy, the higher the order of harmonics, which are found in the effective excitation pattern.

Another advantage of SIM is its compatibility with various dyes. In principle all fluorescent proteins and synthetic dyes are compatible for SIM, facilitating multi-color SIM. SSIM on the other hand is slower and more demanding of the dyes used. To reach ~50 nm resolution in 2D, 108 pictures at different stripe orientation angles and phases need to be captured. SSIM additionally requires extremely photostable dyes because of the high laser intensities required to saturate fluorescence emission (Gustafsson, 2005).

While the resolution gain of SIM is modest compared to STED or localization microscopy, the acquisition speed reached is higher than in any other super-resolution method. It makes SIM the optimal method for live imaging in a big field of view, when spatial resolution is not the top priority (Fiolka et al., 2012; Kner et al., 2009; Shao et al., 2011). It is important to note though that SIM-reconstruction requires significant post-processing, which makes it sensitive to motion artifacts.

1.2.2 Stimulated Emission Depletion (STED) Microscopy

The first method developed allowing to break the diffraction barrier in far-field fluorescence microscopy was developed in 1994 (Hell and Wichmann, 1994). The concept is to deplete spontaneous emission at the periphery of a diffraction limited light spot using the process of stimulated emission. The dimension of the PSF shaped by this method is smaller than the PSF of a conventional imaging system according to Abbe’s diffraction limit, improving the achievable resolution.

In practice, the sample is scanned pixel by pixel as for confocal light scanning microscopy (CLSM), but in addition to the excitation beam the sample is also exposed to a depletion laser, the so-called STED beam. The wavelength of the STED beam is red-shifted compared to the excitation laser. The superposition of excitation and depletion laser results in stimulated emission, which is the process in which photons emitted by the depletion laser trigger excited atoms of the fluorophore to undergo an energetic transition from the excited state into the ground state. Using a phase-modulator the intensity in the center of the depletion beam is reduced to zero by destructive interference, the resulting depletion beam profile is ‘donut-shaped’. So there remains an unaffected region around the beam center, where the STED laser intensity is zero and the fluorophores are only exposed to the excitation laser, as in conventional microscopy. This region is significantly smaller though than in conventional microscopy, see Figure 1-13. The resulting effective excitation spot size defines the resolution reached by STED.

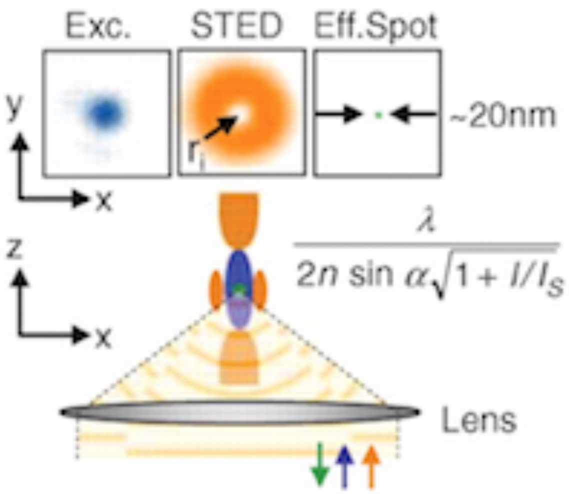

Figure 1-13: STED principle
Top panel shows the beam profiles of the excitation beam (blue), the STED beam (orange) and the effective excitation region (green) in the xy-plane. Effective excitation spot is ~20 nm in this example. Lower panel shows the axial profiles. Cartoon from (Hell, 2007).

STED resolution can be approximated by $d_{STED} \approx \frac{\lambda}{2*n*\sin(\theta)*(1+\sqrt{\frac{I}{I_{sat}}})}$. Fluorophores spaced at sub-diffractive distances bigger than d_{STED} can now be distinguished, since they can be imaged sequentially by scanning small sample volumes one after another. I denotes the intensity of the STED beam and I_{sat} the saturation intensity for the transition, where half of the molecules are in the excited state and the other half in ground state. In order to reach resolutions as good as 20 - 40 nm, high STED laser intensities in the order of 100 – 500 MW/cm^2 have to be reached at the crest of the depletion beam (Grotjohann et al., 2011), this is about 3 orders of magnitude higher than the intensity of the excitation beam (Nägerl et al., 2008). This requirement demands high photo-stability of the fluorophores used and can negatively affect biological samples.

Axial resolution can also be improved using phase modulation. By applying a quenching pattern above and below the focal plane an axial resolution ~100 nm could be reached (Klar et al., 2000), by adding a second lens using the 4Pi –setup, the axial resolution could be even further improved down to 33 nm (Dyba and Hell, 2002).

STED microscopes were originally operated only in pulsed mode, where both excitation and depletion beam where pulsed. The development of CW-STED (Willig et al., 2007), making continuous wave lasers applicable for STED microscopy, has made the technique more affordable and easier to implement. CW-STED also improved scanning speed. A significant improvement in resolution for CW-STED can be achieved with time gated STED (T-STED) (Moffitt et al., 2011; Vicidomini et al., 2011). This approach takes advantage of the longer life-time of the fluorescent state of fluorophores at the unaffected center compared to the periphery of the STED donut. The detectors begin photon-collection only after a defined temporal offset. In effect, fluorescence life times shorter than the cut-off threshold, which dominantly stem from the peripheral regions, can be selectively excluded from detection.

While the original STED microscopy relies on molecular electronic transitions where fluorophores are brought from excited state S_1 to ground state S_0, the concept has now been generalized to also exploit additional on-off transitions of fluorophores, such as conformational changes. The acronym for this generalized concept is RESOLFT (Reversible Saturable Optical Fluorescence Transitions). The advantage of using alternative transitions is the lower light intensity required to achieve super-resolution, making the technique applicable for live cell imaging. In 2011 it was demonstrated that by using a reversibly switchable enhanced GFP (rsEGFP), an intracellular resolution below 40 nm could be achieved imaging living cells (Grotjohann et al., 2011).

1.2.3 Single-Molecule Localization Microscopy – PALM/ STORM/ GSDIM

This class of super-resolution microscopy techniques takes advantage of the high center localization precision, which can be reached for single diffraction limited emitters. When any diffraction limited volume in the sample contains no more than one single emitting fluorophore, the problem of overlapping fluorescent signal of closely spaced fluorophores is avoided and individual fluorophore positions can be localized at very high precision. In practice, a long image sequence is recorded with high frequency sampling, so positions of a significant fraction of all fluorophores in the samples can be localized cumulatively over time. Photo-switchable probes allow observing a small subset of all fluorophores in the sample at any time. Localization precision below 10 nm can be achieved. The resulting image is then reconstructed by summing up center positions of all detected single molecule events.

Stochastic optical reconstruction microscopy (STORM) (Rust et al., 2006), photo activated localization microscopy (PALM) (Betzig et al., 2006) and fluorescence photo-activation localization microscopy (FPALM) (Hess et al., 2006) were the original localization based super-resolution microscopy methods developed independently by three different laboratories.

In contrast to PALM, which uses photo-activation/ photo-conversion of fluorescent proteins, STORM makes use of photo-switching of synthetic fluorophores. STORM originally relied on an activator-emitter fluorophore pair to realize photo-switching. Cy5 (exc. 647 nm) was used as the actual fluorescent reporter, which was driven into the dark state. A Cy3-molecule in close proximity to the Cy5-molecule (exc. 532 nm) was used to trigger the return of Cy5 from the dark state. In 2008 ground state depletion microscopy followed by individual molecule return (GSDIM) (Fölling et al., 2008), also referred to as direct stochastic optical reconstruction microscopy (dSTORM) (Heilemann et al., 2008) based on the STORM principle was developed. These methods no longer require a fluorophore pair for photo-switching. Instead they directly switch fluorophores into their dark states and bring them back to an excitable state using UV-light (405 nm).

A GSDIM experiment starts with continuous illumination of the sample at high laser intensity, until blinking of single molecules returning from the dark state is observed. Fluorophores are driven from their electronic ground state S_0 into the excited state S_1. The fluorescent lifetime of molecules is typically short, only in the order of ns. From S_1 the molecule can either return to the ground state via photon-emission or go into a dark state, typically the metastable triplet state T_1 via intersystem crossing. The probability of the S_1 to S_0 transition is typically three orders of magnitude higher than the transition probability from S_1 to T_1. But since the triplet state is long-lived with lifetimes ranging from ~0.1 – 100 ms, it is nevertheless possible to accumulate a triplet state population. The molecule can also enter additional dark states with lifetimes up to several seconds. As long as no irreversible photo-bleaching occurs from the higher energy electronic states, the fluorophore can return to its electronic ground state S_0 and undergo the next switching cycle.

An optimal fluorophore for localization microscopy needs high on-off emission contrast and should be able to undergo many switching cycles. A high number of photons per switching event increases the localization precision, which in turn critically limits the achievable resolution. At the same time photon-emission from the dark state needs to minimal. The currently best available fluorophores, such as Alexa 647, can reach ~30 switching cycles and > 5000 photons per switching cycle. Additionally the equilibrium on-off duty cycle of the fluorophores should be low, this is the time fraction the molecule spends in S_1 compared to the dark states. The duty cycle is ~0.001 for Alexa 647 in optimal buffer conditions (Dempsey et al., 2011).

The specific demand of fluorophore photo-physics requires optimized chemical buffer conditions, which can vary for fluorophores. A key requirement to achieve molecular blinking of fluorophores is the stabilization of the non-fluorescent triplet state. Localization microscopy therefore relies on imaging buffers reduced in molecular oxygen and with millimolar concentrations of reducing agents such as thiols (Rust et al., 2006). Molecular oxygen is a known triplet quencher. In its open-shell triplet ground state it readily interacts with fluorophore triplet states, changing their duty cycle unfavorably. It is therefore common practice to deplete molecular oxygen from the imaging buffer using the combination of an enzymatic system of glucose-oxidase and catalase with glucose as the substrate (GLOX). An additional desirable effect of oxygen reduction is the increased fluorophore photostability. Primary thiols help to stabilize the triplet state, either β-mercaptoethanol or β-mercaptoethanolamine (MEA) are commonly used (Vogelsang et al., 2008). A reasonable number of dyes perform best or at least well in buffers containing GLOX and thiol, making them compatible for multicolor imaging. Other fluorophores such as ATTO 532, however perform best when embedded in solid poly-vinyl alcohol (PVA). It was also reported that glycerol based vectrashield mounting medium (Vector Labs) is a compatible environment for the most popular far-red dyes used in STORM such as Alexa 647 and Dyomics 647 (Olivier et al., 2013). The choice of fluorophores for multi-color imaging in single molecule localization microscopy can thus be limited depending on environmental requirements of the dyes and biological sample.

2D localization microscopy only has the axial resolution of a conventional wide-field microscope which is in the order of 800-1000 nm. Various strategies have been employed to improve axial resolution in localization microscopy. The first 3D-STORM setup was realized using astigmatism. Introducing a cylindrical lens in the illumination light-path yields an elliptical PSF. The eccentricity of the now ‘distorted’ PSF varies along the optical axis and also with lateral distance from the optical axis. From the PSF shape and the lateral position from the optical axis, it is thus possible to calculate the imaged z-position (Huang et al., 2008). Additional strategies to improve axial resolution using the shape of the PSF in localization microscopy include using a double-helix PSF (Pavani et al., 2009) and biplane FPALM using a double plane detection scheme (Juette et al., 2008). While these methods reach significantly improved z-resolution, they do not provide isotropic resolution. Another drawback is the necessary distortion of the PSF, which reduces lateral resolution. In order to sample a significant z-volume, the sample needs to be exposed to a lot of light and for a long time. Photobleaching and sample drift therefore pose severe limitations to apply these methods to biological samples.

A different approach is taken in virtual volume super-resolution microscopy (VVSRM), here isotropic resolution is reached by introducing a mirror to generate side-views of the sample (Tang et al., 2010). Yet another fundamentally different approach is super-critical angle detection which exploits the principle of surface-generated fluorescence and reaches near-isotropic resolution up to a few hundred nanometers from the glass surface (Deschamps et al., 2014). Dramatic improvement of axial resolution in single molecule localization microscopy was also demonstrated using an interferometric detection scheme named iPALM, where the relative intensity of detected molecules encode the emitter z-positioning(Shtengel et al., 2009)}.(Aquino et al., 2011). Proof-of-principle experiments using microtubules have demonstrated lateral localization precision of ~10 nm and an even higher axial localization precision of ~6 nm in a layer of 650 nm thickness. Yet, operation of the microscopes is still far from trivial, thus so far biological applications of these approaches have been very limited.

While localization microscopy methods reach the highest spatial resolution of all super-resolution techniques, image acquisition in localization-based microscopy is more time demanding compared to SIM and STED. Image sequences containing tens of thousands of time points, sampled ~100 Hz, typically need to be captured for the reconstruction of a super-resolved image. The long time course required makes the method specifically sensitive to stage-drift. The lacking speed limits the applications of single molecule localization microscopy for live-cell imaging. The method is ideally suited for imaging of fixed samples where a high resolution is the top priority. Single molecule localization microscopy also requires high labeling density to reach optimal resolution. This is an important practical parameter to consider, when samples are prepared and stained. The Nyquist-theorem in the context of images states that spatial sampling of an image (pixel size) needs to be at least 2-fold smaller than the smallest distance one wishes to resolve. In order to be able to sample up to the Nyquist-frequency, fluorescent labels in the sample must be spaced closer than half the desired resolution.

1.3 Research Objectives

The main goal of the PhD project presented in this thesis is to characterize the basic polymer features of chromatin by analyzing the properties of RDs, which have emerged as the basic, stable subunits of higher order chromatin organization, in single cells in situ. I have employed state of the art imaging technologies to address both the basic structural and dynamic properties of RD organization inside the nucleus.

The first objective was measuring the physical size of RDs by imaging *in-vivo* nucleotide labeling of RDs using super-resolution microscopy (GSDIM), which can reach lateral resolution below 20 nm. As a second basic structural parameter of RD organization, I was interested in the physical distance separating two adjacent RDs. I set out to measure this distance on *in-vivo* pulse chase two-color labeled RDs using 3D confocal as well as STED microscopy. Thirdly, I measured the range of elastic coupling between genomically neighboring RDs by quantifying the coherence of their respective movement by live cell confocal imaging and computational tracking of double-color labeled RDs. Combined, the results I obtained allow me to formulate a comprehensive model for the dynamic organization of RDs in nuclei of living cells. This model allowed me to predict two different mechanisms by which the chromatin polymer could undergo large-scale compaction, by shortening boundary domains between RDs, or by shrinking RDs. To differentiate between these mechanisms, I induced chromatin condensation acutely by ATP-depletion and used GSDIM to measure changes in RD size after compaction. My results are inconsistent with RD shrinking and thus favor a boundary shortening mechanism of compaction.

In addition to this structural and dynamic characterization of RDs, I was interested to revisit the basic dynamic parameters of chromatin. Since the literature has so far largely relied on a few single artificial loci labeled by ectopic sequences or very specialized regions such as centromeres and telomeres, I decided to take advantage of my ability to label and image many replication domains in live cells and obtain a global picture. My goal was to describe the diffusional dynamics of euchromatic and heterochromatic RDs and investigate how their mobility depends on proximity to the main determinants of nuclear architecture, the nuclear periphery and nucleoli and on cell cycle and especially S-phase progression. To this end, I recorded a large scale data set of time-lapse series of fluorescently labeled early or late replicating RDs in living cells, and mined their movement trajectories in relation to subnuclear and sub-chromosome territorial location and the G1, early/mid/late-S or G2 phase cell cycle state of the cell. This data largely confirmed previous observations of chromatin dynamics in live cells, but provides the first comprehensive, statistically robust and global data set on these parameters. Since my data was consistent with slow diffusion of chromatin constrained by the available free volume inside the nucleus, I additionally characterize how RD dynamics responds to artificially induced changes in nuclear volume, which confirmed that an increase in available volume leads to increased mobility.

2 Methods

2.1 Experimental methods

2.1.1 Cell culture

All cell culture work was carried out under the laminar flow hood (Safe 2020 by ThermoScientific)

Cell line

All experiments presented in this thesis were performed using PCNA-eGFP NRK cells (Ellenberg lab database ID #1428, expanded from #428 construct by Catherine Chapuis).

Cell culture medium

DMEM (4.5 g/L glucose) cell culture medium (Gibco)
10% fetal bovine serum (FBS) (Gibco)
1 mM sodium pyruvate (Gibco)
2 mM L-glutamine (Gibco)
100 U/ml Pen-Strep mix (Gibco)
Filtered with Steritop filter pore size 0.22 μm (Millipore).
Cell were grown in 75 cm^2 cell culture flasks (Falcon)
Cell incubator: at 37 °C in 5% CO_2 (Hera)

Cell passage

Cells were washed twice with 20 ml 1x PBS, treated with 1x Trypsin-EDTA for 2 minutes (left at ambient temperature in laminar flow hood) before splitting. Cells were passaged every day (split 1:2) or every second day (split 1:4) during experiment phases. Cells were maximally used to passage number 40.

Cell freezing

Cells were washed twice with 20 ml 1x PBS, treated with 1x Trypsin-EDTA for 2 minutes (left at ambient temperature in laminar flow hood) before harvesting in 50 ml Falcon Tube. Cells were centrifuged at 1300 rpm for 2 minutes, cell pellet was collected in cryotubes (Sigma) in freezing medium: 90% in FBS, 10% DMSO, then transferred to -80 °C freezer. They were further transferred to the liquid nitrogen tank within 2 weeks.

2.1.2 *In vivo* scrape replication labeling

Cell synchronization step: Arresting cells at G1 to S-phase border

PCNA-eGFP NRK cells were grown in 150 cm^2 cell culture flask to near confluence. Mitotic cells were harvested using mitotic shake-off: Mitotic cells were collected in 15 ml Falcon tube for spinning at 1300 rpm for 2 minutes. Supernatant was discarded and the mitotic cell pellet harvested. Mitotic cells from one 150 cm^2 cell culture flask were plated in one well of an 8-well labtek in 0.5 ml of culture medium containing aphidicolin at 1 µg/ml concentration and placed for 10 h in the tissue culture incubator. Aphidicolin is a reversible inhibitor of DNA replication. Aphidicolin washout was performed after 10 h (this is enough time for the mitotic cells to finish G1-phase, cells are thus arrested at the G1 to S-phase border) three times with 500 µl pre-warmed medium in the labtek well.

Scrape labeling step (single-color labeling)

For early replicating chromatin (euchromatin) labeling I used a 15 min waiting time between aphidicolin washout from synchronized cells and labeling. For late replicating chromatin (heterochromatin) labeling, I used a 3.5 h waiting time between aphidicolin washout from synchronized cells and labeling. Figure 2-1a is an example of a cell where early replicating chromatin was labeled. Figure 2-1b is an example of a cell where late replicating chromatin was labeled.

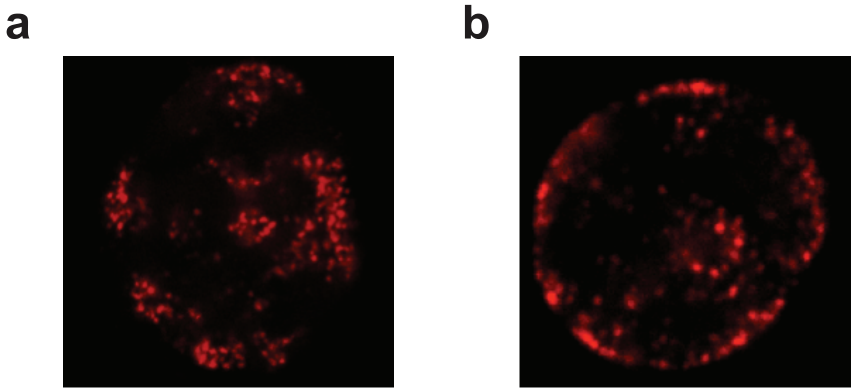

Figure 2-1: Scrape labeling of replicating chromatin.
a, Example of a single nucleus in which early replicating chromatin was labeled (15 min after aphidicolin washout). **b**, Example in which late replicating chromatin was labeled (3.5 h after aphidicolin washout).

After the desired waiting-time, cells were exposed to a final concentration of 67 µM ATTO 633-dUTP (Jena Bio-tec) in culture medium. Cells were scraped off the Labtek surface using a rubber policeman. During the scraping process, cells are exposed to ATTO 633-dUTP for approximately 60 s. The well is then filled with 500 µl of medium to dilute concentration of ATTO 633-dUTP. Cells were returned to cell culture incubator. After 1 h time for cell reattachment, labeled cells were washed five times with 500 µl of pre-warmed medium. This washing step to remove residual ATTO 633-dUTP from the medium prevents aggregation of remaining ATTO 633-dUTP in cell plasma membranes. Cells were further cultured for 5 days to single chromosome territory stage for live cell imaging (only a single chromosome territory remains labeled per cell) or for 3 days for correlated GSDIM and confocal imaging. An overview of the single-color scrape labeling is provided in Figure 2-2.

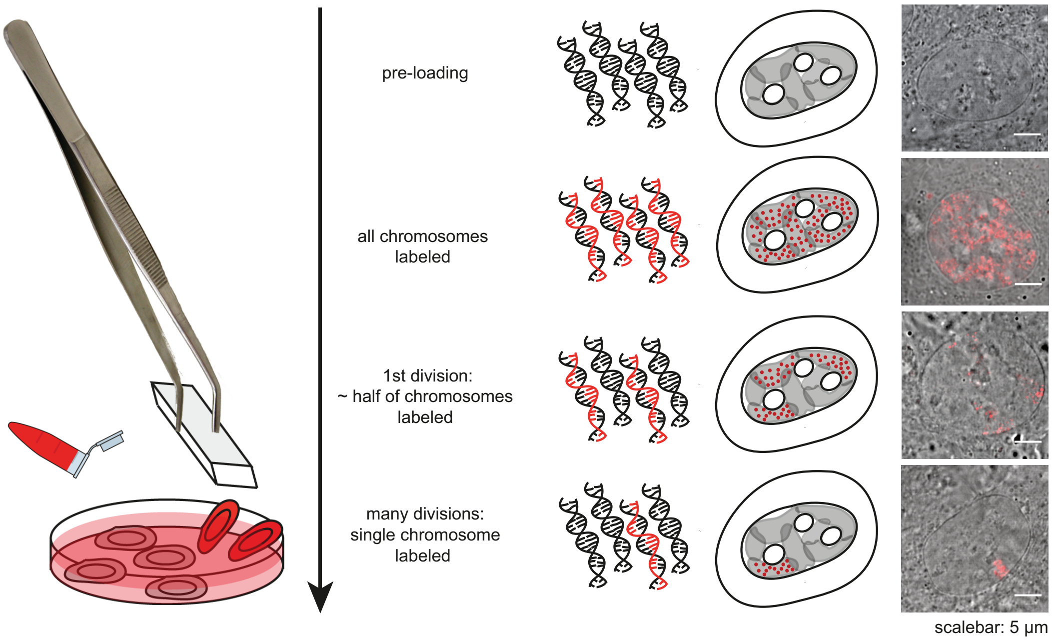

Figure 2-2: Overview of the scrape labeling protocol.
By exposure to ATTO 633-dUTP during cell scraping, the fluorophore is incorporated into the newly synthesized strand of all chromosomes. By semi-conservative inheritance over many cell divisions, eventually only a single chromosome remains labeled.

Scrape labeling step (double-color labeling)

In contrast to the single-color labeling protocol, ATTO 633-dUTP exposed cells were scratched using a hypodermic needle. About 20 horizontal and vertical ‘scratch-lines’ were used respectively in a single well of an 8-well-labtek. After dilution with 500 µl of medium, different waiting times were used before the second labeling step (15, 30, 45, 60, 90 and 120 min). The scratching step kills ~30% of the adherent cells, while scraping generally does not cause cell death. Cells were then exposed to a final concentration of 67 µM ATTO 565-dUTP (second pulse) and scraped off surface using a rubber policeman. During the process, cells are exposed to ATTO 565-dUTP for approximately 60 s. Subsequent steps are identical with the single-color-labeling protocol. Cells were further cultured for one to three days before imaging.

2.1.3 Cell fixation

Cells were washed twice with 1x PBS, then fixed with buffer containing 4% PFA in 1x PBS for 5 minutes at ambient temperature under chemical hood. 16% Para-Formaldehyde (PFA) stock concentration (Electron Microscopy Science) was stored at -20 °C for a maximum of 4 weeks.

> **I have tested PBS compared to HEPES-buffer at different concentrations containing 4% PFA, using overall volume conservation of the nucleus as a parameter to score conservation. HEPES-buffers are commonly used for cell fixation for electron microscopy (EM) imaging of chromatin. The best preservation of nuclear volume were achieved using fixation in 4% PFA dissolved in 1x PBS. HEPES buffer was least distorting at a concentration of 135 mM and 150 mM, the variability between cells was higher though compared to 1x PBS. The results are shown in**

Figure 2-3.

Cells were washed twice with 1x PBS after fixation and left in 1x PBS if they were used for correlated confocal and GSDIM imaging. Cells used for double-color confocal and STED microscopy were mounted in Vectashield H1000 (Vector Laboratories) imaging medium (refractive index 1.45 on autoclaved cover glass). High precision coverslips were used (thickness 0.17 mm ±5 µm). Microscopy slides of size 75×25 mm were used (Menzel).

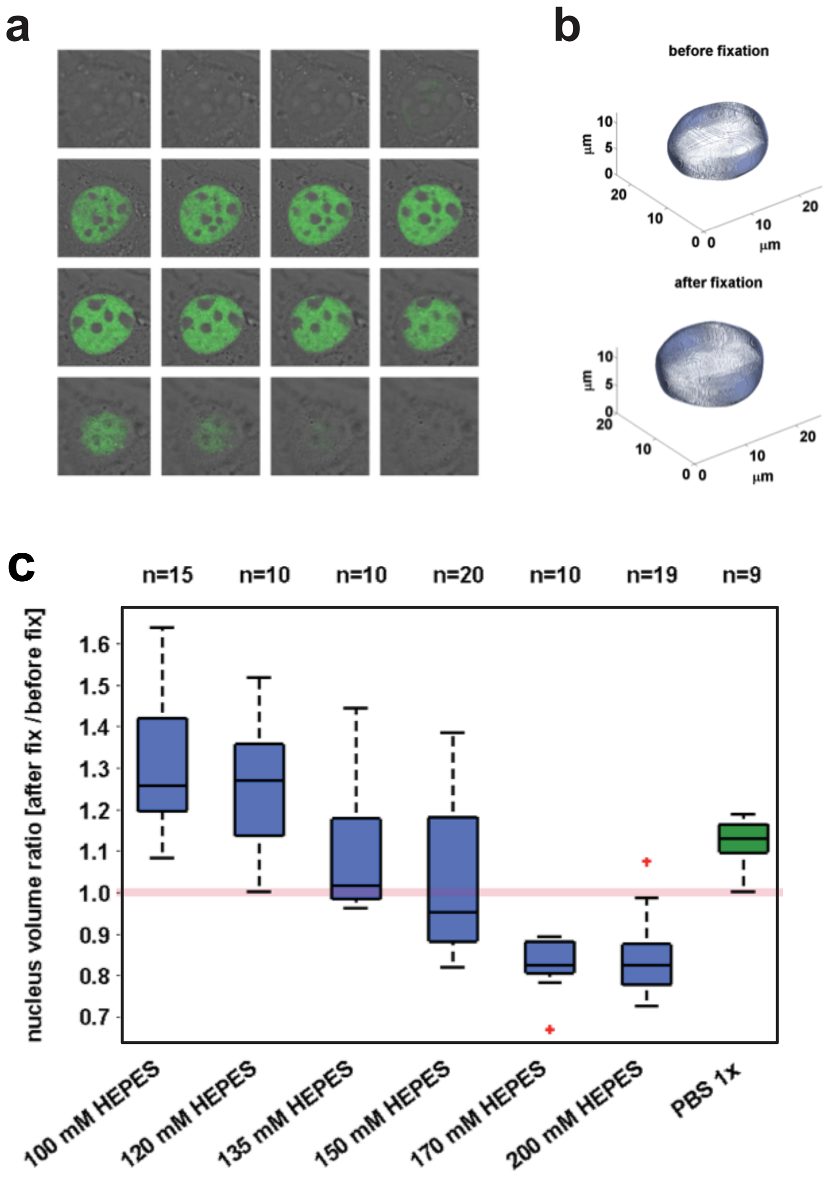

Figure 2-3: Quantification of volume conservation in nuclei fixed in 4% PFA using different buffers.
a, Confocal z-stack of a single nucleus. **b**, 3D segmentation results before and after cell fixation. **c**, Overview of results comparing 1x PBS compared to different concentrations of HEPES-based buffers.

2.1.4 Perturbation Treatments

2.1.4.1 ATP-depletion

Final concentration added to cells: 15 mM NaN_3 (stock concentration 1M in ddH_2O) 30 mM 2-deoxyglucose (Sigma-Aldrich) directly dissolved into imaging medium.

2.1.4.2 Trichostatin A treatment

Stock concentration of TSA (Sigma-Aldrich) 100 µg/ml (302 µM) in DMSO at -20 C. Long-term treatment: 100 ng/ml (0.3 µM) for 20h before washout. Accute treatment: 200 ng/ml (0.6 µM) for 4h, no washout.

2.1.4.3 Long-term Aphidicolin treatment to increase Nuclear Volume

Final concentration of aphidicolin 1µg/ml (Sigma-Aldrich), stock concentration of aphidicolin 1mM/ml in ethanol store at -20C. Cells were treated for 20h.

2.2 Microscopy

2.2.1 Confocal Live Microscopy

2.2.1.1 Reducing oxygen level in imaging medium to minimize photo-toxicity in live cell imaging experiments

Reactive oxygen species are the most common cause of photo-toxicity in live-cell fluorescence microscopy experiments (Dixit and Cyr, 2003). They are very reactive and readily damage biological macromolecules including nucleic acids, proteins and lipids.

Molecular oxygen has two unpaired electrons in its outer shell. The two electrons occupy separate orbitals and have parallel spin, forming a triplet state. This triplet ground state prevents molecular oxygen from reacting directly with most other molecules at room temperature, which are typically in the singlet state, according to Wigner's spin conservation rule. Molecular oxygen can convert into excited singlet oxygen through thermal activation or photochemical action of photosensitizers (e.g. fluorophores). Singlet oxygen in turn gives rise to a series of oxygen-derived radicals, collectively referred to as reactive oxygen species (Schweitzer and Schmidt, 2003). Upon laser excitation, fluorophores act as photosensitizers catalyzing the conversion of molecular oxygen into reactive singlet oxygen. Especially synthetic fluorophores are problematic in this respect. Unlike in fluorescent proteins, in which the fluorogenic cores are commonly contained within a barrel of beta-sheets, the uncontained radicals formed through photosensitization by synthetic fluorophores are even more likely to damage cellular structures.

A way to reduce cellular damage introduced by photo-toxicity in live cell microscopy experiments is lowering oxygen levels in the imaging medium. The hypoxic condition is well tolerated by cell culture. While ambient oxygen concentration is about 20%, physiological oxygen concentration in tissues of living organisms is in the range of 1% to 11% (e.g. 3% in skin, 4% in muscle and 10% in kidney (Carreau et al., 2011)).

When oxygen was completely depleted from the medium, the proliferation of NRK PCNA-EGFP cells, which is the cell-line used throughout this work, is heavily compromised. The cells stop dividing and loose their typical PCNA replication pattern over time. I further tested if the NRK cells would also be impaired by a lowered oxygen concentration to 5%. When reducing the oxygen concentration to 5%, I could see that cells were still replicating normally, as indicated by the unaltered PCNA-eGFP patterns displayed by the NRK cells. In order to exclude long-term effects, I have taken 30 h time-lapse movies of the NRK cells seeded on 2-well labteks and immersed in imaging buffer. I have acquired z-stacks of 5 planes using 1 μm spacing every 30 minutes during the time course. Imaging buffer with fresh Oxyrase and lactate were supplied every 10 h. The result showed that oxygen reduction to ~5% by Oxyrase in medium containing 10 mM lactate did not alter cell cycle duration or replication pattern displayed by PCNA-eGFP NRK cells. Median cell cycle duration of PCNA-eGFP NRK cells in control labteks at ambient O_2 concentration was 21.8 ± 3.5 h (n = 20 cells used for analysis), compared to 20.7±3.8 h (n = 19) in cells with reduced oxygen concentration in 10 mM lactate with OxyFluor. Cells in lactate control with 10 mM lactate, but without OxyFluor in medium, had a median cell cycle duration of 21.1±3.5 h (n = 18). Each condition was assessed in three independent experiments. Statistical testing performed between control and low oxygen/lactate control does not indicate a significant change in cell cycle duration (Student's *t*-test $P = 0.35$ and $P = 0.71$, respectively).

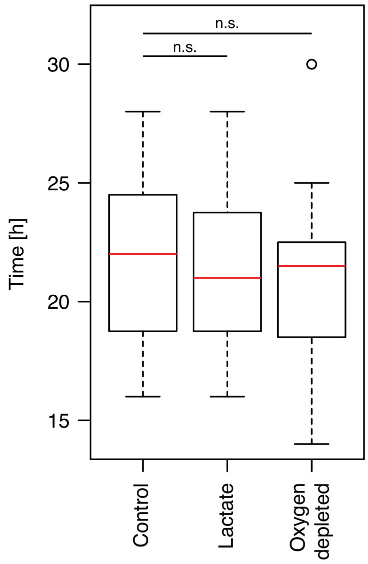

Figure 2-4 Control showing that oxygen depletion and lactate concentration in imaging medium do not affect cell cycle timing in PCNA-GFP-NRK cells

Oxygen levels in the imaging medium were lowered enzymatically using OxyFluor containing the Oxyrase system (Oxyrase Inc.). Oxyrase is an enzyme system extracted from *E. coli* membranes (actual enzymes are not disclosed by the vendor) and uses lactate as a substrate to reduce oxygen concentration in the culture medium. It was originally developed for anaerobic bacterial culture. At concentrations above 0.03 U/ml, and with at least 10 mM lactate as a substrate, it can fully deplete oxygen from the medium up to a few millimeters away from the liquid/air interface (WONGLUMSOM et al., 2000). Metazoan cell culture, unlike anaerobic bacteria, typically do not grow in anaerobic conditions, even though there are exceptions (Hills, 1940; Marcus, 1973). In order to retain some oxygen in the medium Oxyrase has previously been used at low concentration (0.5-1 U/ml) in the imaging medium as a photo-protectant for imaging experiments with mammalian cell culture (Wittmann et al., 2003). To find ensure reproducible imaging conditions, I developed a protocol, which allows to maintain stable oxygen levels during imaging. In this protocol the oxygen concentration at the bottom of the dish is controlled by the height of the liquid level. This results in stable and easily controllable oxygen levels.

The kinetic rates of oxygen diffusing in and the rate at which oxygen is consumed by the enzymatic system define the oxygen concentration in the medium. Even with a high concentration of Oxyrase enzyme in the medium quickly using up the available oxygen, the region close to the air/liquid interface in the imaging dish always retains at a non-zero oxygen concentration, since atmospheric oxygen keeps diffusing into the liquid. The deeper one goes into the imaging well, the lower the oxygen concentration found. Thus, a simple way to adjust the oxygen concentration at the bottom of an imaging dish is to adjust the height of the liquid level above the dish bottom, while keeping the Oxyrase concentration in the imaging medium constant.

To prepared cells for imaging at different oxygen levels I used 1:100 Oxyrase final concentration 0.3 U/ml (Oxyrase Inc.) and 10 mM sodium lactate (sodium DL-lactate solution syrup, 60% (w/w), Sigma) in the imaging buffer and filled 2-well-labteks (well surface: 4.2 cm^2) with different levels of buffer. Over a timespan of 30 minutes, the oxygen concentration at the bottom of the labtek decreased from ambient levels and plateaued into steady state. By fully filling up a labtek-well and creating high liquid levels using >2.5 ml of media, oxygen concentration at the bottom of the dish drops to below 0.01%. For very low liquid levels in the imaging well, small buffer volumes of <0.25 ml per 2-well labtek well, oxygen concentration at the bottom of the dish stayed at ambient oxygen concentration of just below 20%. To lower the 5% oxygen at the bottom of a 2-well labtek is reached by using 1.7 ml (4 mm liquid level) of buffer in a well of a 2-well labtek. Because surface tension creates a meniscus, which causes higher liquid levels at the labtek edges compared to the labtek center, all measurements were performed in the central square (1 cm^2) of the labtek well.

Labteks were sealed using silicon grease (Bayer). Imaging was performed in an environmental box at 37 °C. Oxygen measurements at the bottom of the dish were performed using the FireSting O_2 fiberoptic oxygen meter with a retractable needle tip sensor (430 μm diameter).

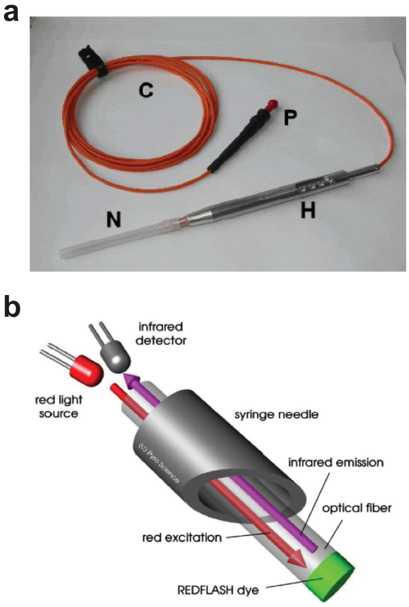

Figure 2-5: The FireSting oxygen meter with a needle-type sensor.
a, Photograph of the needle-type sensor. **b**, Illustration showing of the sensor. Figure taken from the manufacturer website.

2.2.1.2 Protocol for Preparing Cells for Live Cell Imaging

Labeled cells (labeling usually 5 days prior to imaging) were plated on 2-well-labteks dishes typically a day before the imaging experiment and kept in the incubator with regular cell culture medium. CO_2-independent medium without phenol red (Gibco) containing 20% FCS (Gibco), 1% glutamine (Gibco), 1% streptomycin/penicillin mix (final concentration 100 U/ml streptomycin and 100 µg/ml penicillin) was warmed up to 37 C. 10 mM final concentration of lactate and OxyFluor (Oxyrase) 1:100 was added to the prewarmed imaging medium. Then 1.7 ml of the oxygen-depleted imaging medium was added to the 2-well labtek with the cells and incubated for at least 30 minutes for the oxygen level to reach ~5% before start of imaging.

2.2.1.3 Confocal live cell imaging settings

All confocal live and fixed cell imaging was done using a Zeiss LSM 780 ConfoCor 3 microscope. The objective used was an alpha Plan-Apochromat (63x, NA 1.4). GaAsP detectors were used for imaging EGFP. APD detectors were used for detecting signal from ATTO 633 and ATTO 565.

Live cell imaging settings, 2D time-lapse movies (single-color)

ATTO 633 was stimulated using a 633 nm laser; xy-pixel size: 90 nm; sampling rate: 2 Hz; 300 frames were collected; image window 100×100 pixels; pixel dwell 8.2 µs per pixel, no averaging. Maximum light deposition of sample was kept below 5 J/cm^2 for the reference dataset of 142 cells presented in results chapter 3-4.

Live cell imaging settings, 2D time-lapse movies (double-color)

ATTO 633 was stimulated using a 633 nm laser. ATTO 565 was stimulated using a 565 nm laser. Simultaneous scanning of both channels was performed; xy-pixel size: 90 nm; sampling rate: 2 Hz; 300 frames were collected; image window 300×300 pixels; pixel dwell 8.16 µs per pixel, no averaging.

Confocal z-stacks (before and after ATP-depletion)

ATTO 633 was stimulated using a 633 nm laser; xy-pixel size: 90 nm; z-pixel size 400 nm; image window 100×100 pixels; pixel dwell 8.2 µs per pixel, no averaging.

2.2.1.4 Confocal fixed cell imaging

Confocal z-stacks (for correlated confocal and GSDIM imaging)

ATTO 633 was stimulated using a 633 nm laser; xy-pixel size: 90 nm; z-pixel size 200 nm; image window 100×100 pixels; Cells were plated on IBIDI dishes with 50 µm grid-size, see Figure 2-6.

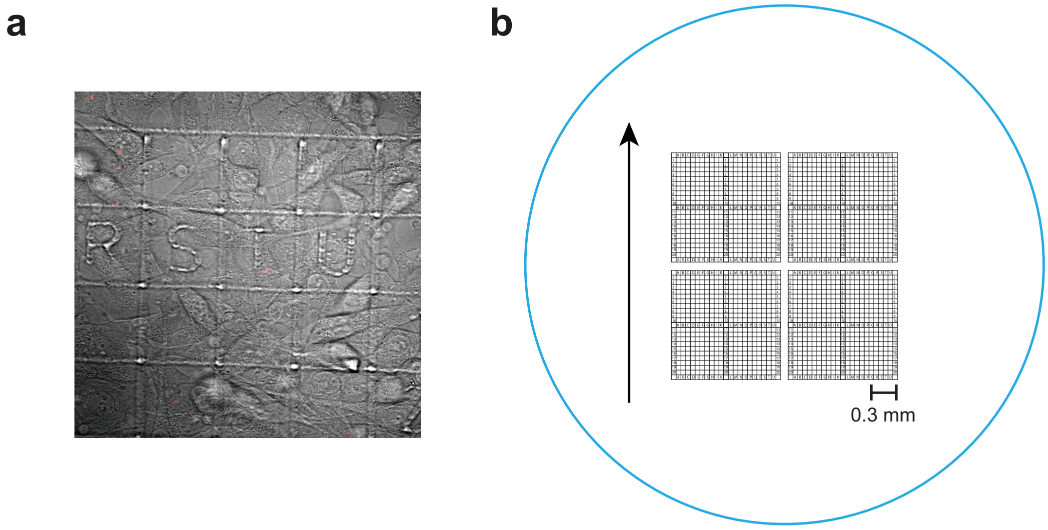

Figure 2-6: IBIDI dishes used for correlated confocal and GSDIM imaging. **a**, The grid is labeled by alphanumeric characters. This allows for subsequent imaging of the same cell using different imaging techniques. **b**, Schematic of a gridded dish.

Confocal z-stacks (double-color imaging)

ATTO 633 was stimulated using a 633 nm laser. ATTO 565 was stimulated using a 565 nm laser. Sequential scanning of both channels was performed, frame-by-frame; xy-pixel size: 90 nm; z-pixel size 150 nm; image window 300×300 pixels.

2.2.2 STED imaging

STED images were taken on a Leica SP8 STED 3X microscope with gated detection, white-light laser (470-670 nm), STED laser (592 and 660 nm); xy-pixel size: 30 nm; z-pixel size: 150 nm; using 2D-depletion doughnut; image window 256×256 pixels; sampling rate: 400 Hz; Scanning objective: 100x, NA 1.4.

Dual color gated STED was performed using ATTO 532 and ATTO 565. The fluorophores were excited using white-light laser, see Figure 2-7. Both dyes were depleted using a 660 nm depletion beam.

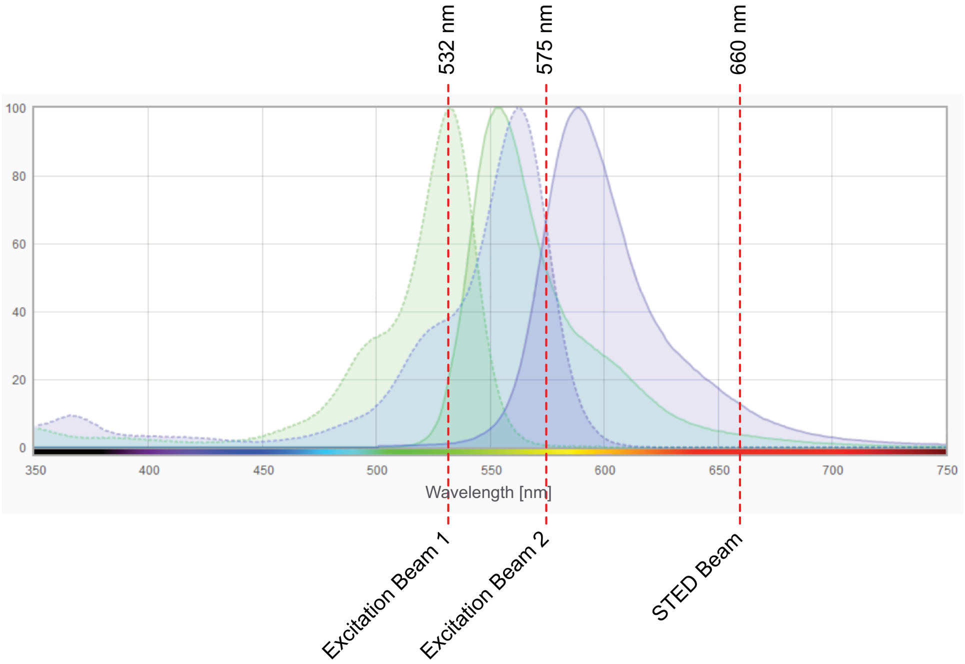

Figure 2-7: Absorption and emission spectra for dual-color STED imaging using ATTO 532 (green spectra) and ATTO 565 (blue spectra).
Both excitation wavelengths and depletion wavelength are indicated.

<u>Deconvolution settings used in Huygen SVI for STED deconvolution</u>

Signal-to-noise ratio (SNR) of images was between 5 and 15 depending on image quality. SNR was estimated using Huygen SVI wizard._Further parameters used for deconvolution (except imaging settings):_STED saturation factor = 40; excitation fill factor: 1.2; immunity factor: 1%.

2.2.3 GSDIM imaging

Most of the GSDIM experiments were mainly performed by Dr. Maria Julia Roberti.

Blinking buffer

Fresh linking buffer was prepared freshly immediately before each experiment. Blinking buffer was exchanged to fresh buffer every 2-3 h.

10 mM MEA/GLOX
50 mM Tris pH 8.5,
10 mM NaCl
10% w/v glucose
0.5 mg/ml glucose oxidase (Sigma # G0543),
40 µg/ml catalase (Sigma #C3155)
10 mM MEA (stock at -20 °C; 100 mM in 1x PBS and pH 7.4, titrated using HCl)

GSDIM imaging settings

GSDIM imaging was performed on a Leica SR 3D GSD microscope, lasers: 642 nm (500 mW), 405 nm diode laser (30 mW) by Coherent Inc. and Suppressed Motion (SuMo) stage; Objectives used were Leica HCX PL APO 100x, NA 1.47 Oil CORR TIRF PIFOC and HCX PL APO 160x, 1.43 Oil CORR TIRF PIFOC; Andor iXon3 897 EMCCD camera; pixel size: 100 nm. Microscope was operated in epifluorescence mode. System was left to equilibrate for 2 hours before system start and sample mounting. Samples were exposed to maximum laser power 642 nm until single fluorophore blinking was detected. Then the actual imaging started. A series of at least 30,000 frames were acquired, a sampling rate of 100 Hz was used. Sample was illuminated with the UV-405 nm laser. Laser power was manually increased.

2.3 Image analysis

2.3.1 GSDIM image analysis

Building and processing the event-list

All GSDIM movies were localized with the Leica SR GSD Wizard with photon threshold 40. The event-list built by Leica SR GSD Wizard was imported and further processed using MATLAB 2012b. Localizations with less than 500 photons were filtered out, threshold was chosen based on shape of the intensity histogram. Lateral drift in the images was corrected using a correlation-based algorithm implemented by Anna Szymborska (Szymborska et al., 2013).

Estimating image resolution

Residual drift in the event-list, which could not be corrected by the drift-correction algorithm, was quantified by Fourier-ring profile analysis (Banterle et al., 2013). Fourier-ring profiles were generated according to the description of Banterle *et al.*, 2013. The Fourier-ring was calculated for each event-list, and the radial profile along the images center to evaluate symmetry for every cell was plotted. Then the single CTs were cropped out from each nucleus manually using a MATLAB routine. Typically two to three well separated CTs per nucleus images were identified.

Image resolution was estimated for each CT according to the Fourier-ring correlation using the 3-sigma threshold criterion (Nieuwenhuizen et al., 2013), calculated in a script using MATLAB 2012b; The implementation was done according to Nieuwenhuizen *et al.,* 2013. Event-lists were not randomized but divided into 2 temporal blocks, from beginning to half of the event-list and from half to end. When images had residual drift not detected as strong asymmetry in the Fourier-ring profile, such as rotational drift, this is reflected in the estimate for resolution. I excluded all images from analysis which showed an asymmetric Fourier-ring profile or which had resolution worse than 50 nm, calculated using the 3-sigma threshold. Super-resolved images were reconstructed with 10 nm pixel size.

Image Preprocessing

Median filter (3-by-3 neighborhood) was applied to the reconstructed raw images. All pixels not connected to at least 3 other pixels were filtered. Forks were detected using grayscale dilation. The structural element used was a disc of radius 4 pixels.

Detecting replication forks as local maxima

For each pixel in the image, the neighborhood defined by the structural element is scanned for the highest intensity value found. This highest intensity value is then assigned to the pixel. Then the grayscale dilated image is subtracted from the original. Local maxima have intensity value 0 on the subtracted image. When directly neighboring pixels were simultaneously identified as local maxima, only one of them was kept for analysis.

Clustering of replication forks into RD using density based clustering

The identified forks were clustered using the DBSCAN algorithm (Ester et al., 1996) in an implementation by Michal Daszykowski (Daszykowski et al., 2002) using the following parameters: minimal cluster size k=2 in a neighborhood radius of 14 pixels.

Parameter extraction

The following values were calculated from the clustered replication forks:

- Total number of replication forks, number of replication fork clusters, number of solitary replication forks
- Nearest neighbor distance between forks within clusters
- Convex hull of each cluster with at least 3 replication forks as a measure for RD size
- Feret-Diameter of each cluster as a measure for replication domain area

Automated Confocal and GSDIM overlay

Overlays were created using MATLAB 2012b. Confocal images (xy-pixel size: 90 nm) were scaled up by a factor of 9 and horizontally flipped to match GSDIM images with 10 nm xy-pixel size. Each confocal stack contained 1 CT. All possible substacks with 5 z-slices of confocal z-stacks were calculated (sum intensity). Each of the projected substacks were registered against the GSDIM image using the iterative intensity-based automatic rigid-body registration algorithm in MATLAB 2012b. Then for all registered substacks, the normalized cross-correlation between each projected substack and the GSDIM images was computed. The substack with the highest maximum value in the correlation matrix was picked for the overlay.

2.3.2 Live cell analysis

2.3.2.1 Tracking of RDs in Single Chromosome Territories

In order to get a systematic overview of chromatin diffusion across the nucleus I acquired a dataset of time-lapse movies (300 frames, 2 Hz sampling) from 141 cells, each with a single labeled CT. The size of the dataset (141 CTs/ 1,372 trajectories of RDs) and the need to extract objective dynamic parameters from it required an automated analysis pipeline. After testing the most commonly used particle trackers (Jaqaman et al., 2008; Sbalzarini and Koumoutsakos, 2005), we decided that I would need to dedicate some time into a writing customized object tracker for my analysis. Therefore, I have put significant efforts into the development of the automated live cell image analysis pipeline, which I am presenting in the following. An overview of the pipeline is given in Figure 2-8.

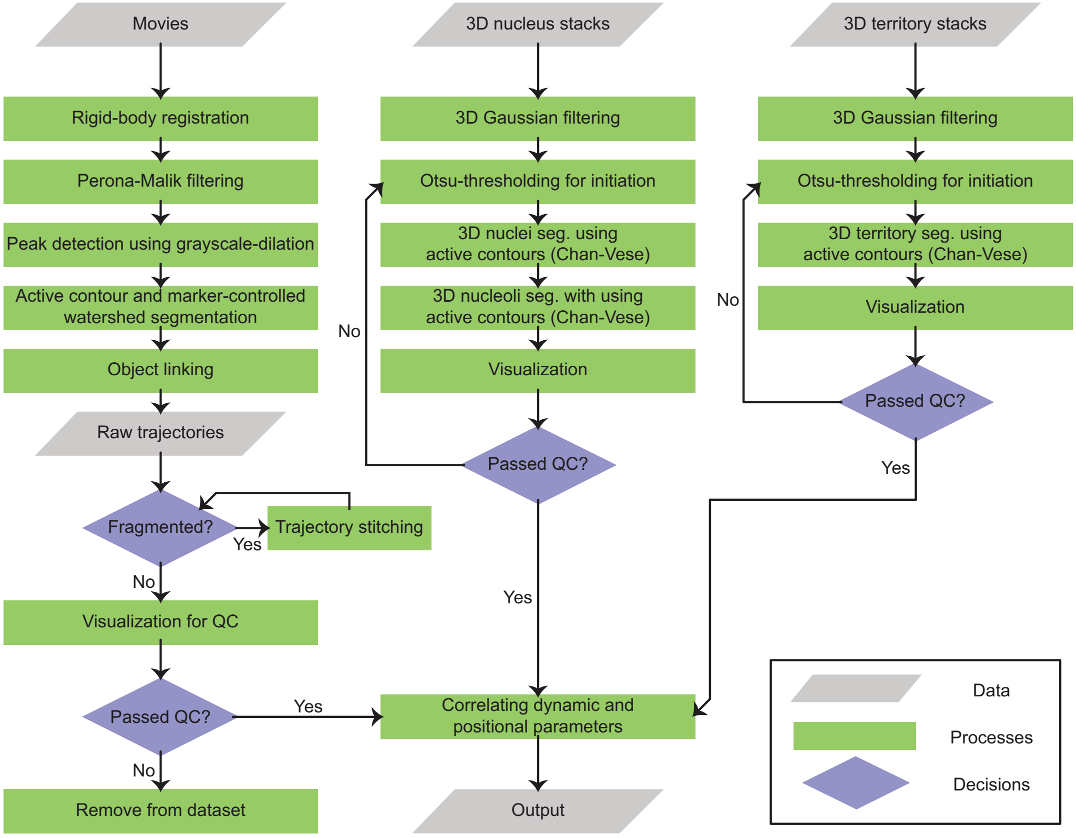

Figure 2-8: Overview of the automated live cell image analysis pipeline. Time-lapse movies of labeled RD, z-stacks of PCNA-eGFP and chromosome territory stacks (determined by all labeled RD) of the same cells were analyzed. More details are given in the Results chapter.

The challenge for automatic tracking of individual RDs in this specific dataset is the reliable detection of touching domains within densely labeled regions of the CTs. Additionally, this dataset suffered from the common problem in live cell imaging of a low signal-to-noise ratio, since signal intensity has been optimized for low phototoxicity imaging conditions.

As a first step, each movie-frame was preprocessed with the nonlinear Perona-Malik PDE filter (Perona and Malik, 1990) using the Catté regularization (Catté et al., 1992), implemented in the ICY bioimage framework (de Chaumont et al., 2013). This filter suppresses shot noise while minimizing flattening of the actual signal.

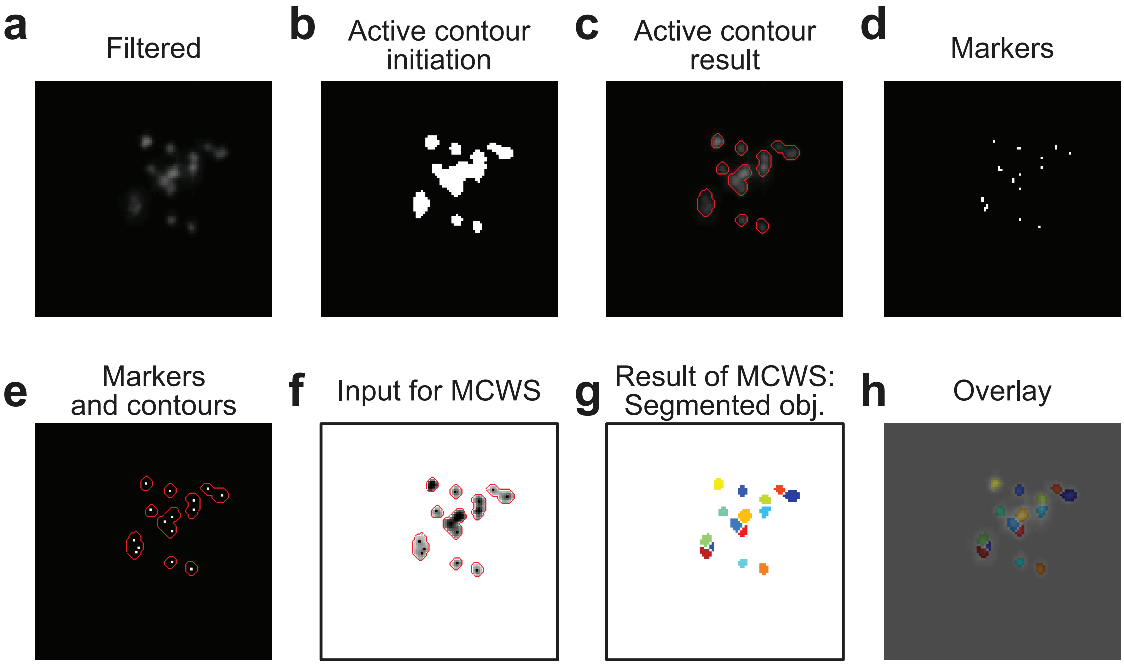

Figure 2-9: Active contour and marker-controlled watershed segmentation. a, Perona-Malik filtered image. b, Segmentation initiation by Otsu-thresholding. c, Result of active contour segmentation. d, Markers detected by grayscale dilation. e, Overlay of markers and contours. f, Image topography before watershed segmentation. g, Segmentation results. h, Overlay of segmentation results with original image.

The next step in the tracking process was the segmentation of RDs. This was challenging in areas where signal from several RD were merging. For the initial segmentation, territory outlines were first found with active contours (Chan and Vese, 2001). The final segmentation from merged RD into individual blobs for each detected RD was achieved using a marker-controlled watershed segmentation algorithm. In this routine, the number of markers controls the number of individual objects, which are then extracted from the image. The markers used are the local intensity peaks of the individual domains, which I detect by grayscale-dilation. This procedure worked well on my movies, since the intensity centers of RD can usually still be easily detected, even if borders of objects are already touching. The individual steps of RD segmentation are exemplified in Figure 2-9.

Since the step-sizes of the labeled domains within the sampling time were significantly smaller than the average nearest neighbor distance, object linking between timepoints to obtain trajectories was rather straight forward. As a linking routine, I adapted the MATLAB-implementation by Sbalzarini *et al.* of the Crocker and Grier Single Particle Tracking (SPT) algorithm (Sbalzarini and Koumoutsakos, 2005) (Crocker and Grier, 1996). In the Sbalzarini-implementation, the optimal set of links is found by the minimization of a cost functional which assigns weighted costs for differences in spatial location and differences in 0th and 2nd image moment of a predefined region around centers of candidate single particles (which are potentially to be linked). Since I segmented objects in the previous step, I could modify the linking process to consider object size and shape as well in the cost function. Fragmented trajectories are stitched based on their positioning and the respective RD area/intensity. The object tracker and subsequent analysis pipeline I custom-wrote for this project are both implemented in MATLAB 2010b.

2.3.2.1.1 Tracking Precision

RD dynamics is constrained and the typical step-size at 2 Hz is only about 100 nm. Thus the particle tracker needs to reach high precision in order to deliver usable results. In order to estimate tracker precision, I recorded a set of 264 trajectories from 31 fixed cells. The standard deviation in both x and y-direction of each time-projected trajectory was calculated and used as a measure of tracking precision σ. All trajectories tracked for longer than 20 frames were used for the initial assessment of tracking precision. The result is shown in the left column of Figure 2-10. It was evident from the initial test, that the tracker sometimes had difficulties in correctly separating closely spaced RDs over the entire trajectory. They were at times wrongly segmented as one object, resulting in a fluctuation of RD shape (eccentricity, major axis length) and area over the trajectory, evidenced by high standard deviations in these parameters correlating with poor tracking precision. In order to filter out RDs tracked at poor resolution, all trajectories with high standard deviations in RD shape and area were filtered out using the following criteria. If a trajectory showed standard deviation in RD area > 5 pixels AND standard deviation in RD major axis length >1.25 (pixels) AND standard deviation > 0.02 in RD shape AND a mean eccentricity > 0.6, the trajectory was classified as poorly tracked and excluded from the subsequent analysis.

2.3.2.1.2 3D segmentation of whole Cell Nuclei and Nucleoli

Both the cell nucleus and nucleoli were segmented using the PCNA-GFP signal. For 3D segmentation I used active contours segmentation implemented with level set methods. The algorithm used was implemented in C++/MEX for MATLAB by Shawn Lankton. The code is freely available through the MATLAB Central page.

2.3.2.1.3 Correlating Dynamic Parameters with intranuclear/intraterritorial Positioning

The processing step in which dynamic parameters extracted from 2D trajectories are correlated with positional parameters extracted from 3D segmentations is depicted in more detail in Figure 2-11. The association between the RDs tracked on 2D movies and their intranuclear/intraterritorial positioning was made using image cross-correlation of the first frame of each movie and the respective z-stacks of both the whole nucleus and higher resolution z-stacks of each CT.

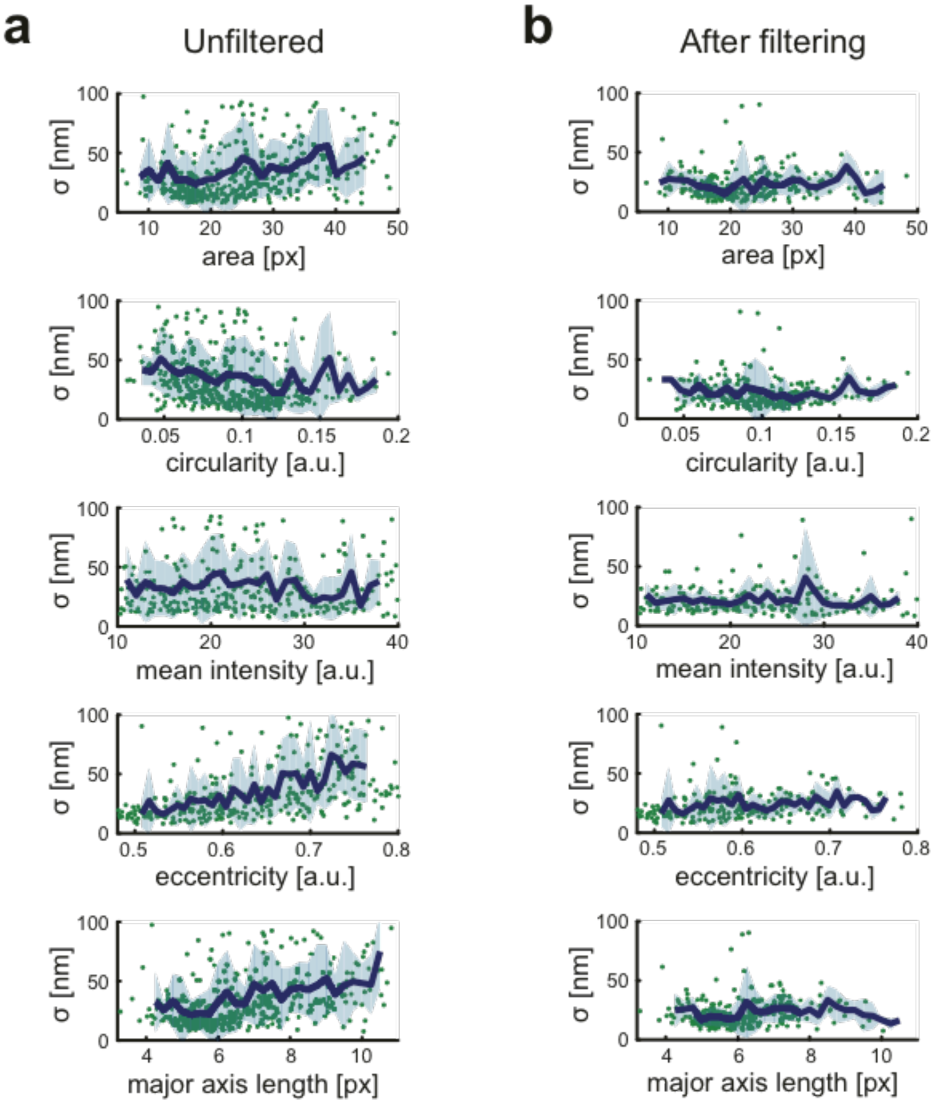

Figure 2-10 Quantification of Tracking Precision

a, On the left column the tracking precision was plotted against RD size and shape parameters, revealing that the tracker has a problem with big, elongated structures. In **b,** these poorly tracked RDs are excluded by an objective filtering routine, the remaining trajectories can all be tracked with high precision, well below 30 nm.

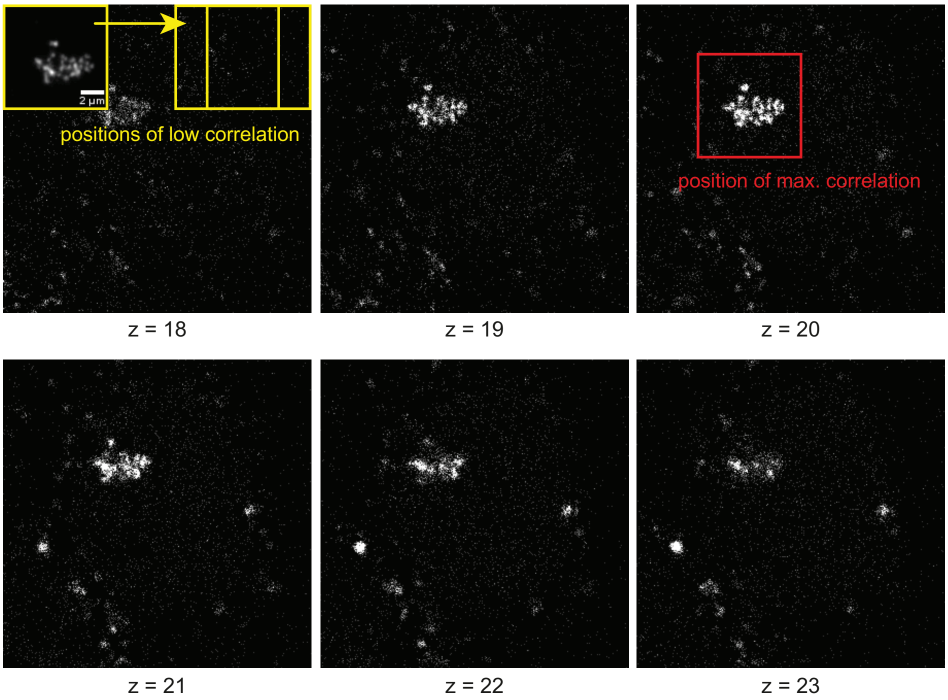

Figure 2-11: Correlating RD positions between time-lapse movies and 3D stacks.
The position of maximum image cross-correlation was identified between 2D movie and z-stack of entire nucleus for each cell tracked.

2.3.2.2 Quantifying CT Volume Change upon ATP-depletion

In the z-stacks of single labeled CTs before and after ATP-depletion in live cells, the CT volume was estimated by finding RD intensity peaks in 3D using gray-scale dilation. The convex hull containing all RD centers was subsequently calculated as an estimated of CT volume.

3 Results

3.1 Correlative confocal and GSDIM imaging of replication domains in fixed cells

In the introduction I have summarized evidence from the literature suggesting that replication domains (RDs) correspond to the fundamental subunits structuring the mammalian genome, that have been extensively characterized as topologically associating domains (TADs). The terms Replication Domains and Replication Foci are alternated in the following text, addressing one and the same structure. Basic questions regarding their organization are still unanswered. There is no agreement in the literature regarding their physical size and internal organization, i.e. how many replicons group together to form a RD.

We decided to use ground state depletion followed by individual molecule return (GSDIM) microscopy, which reaches a lateral resolution of up to 20 nm (Fölling et al., 2008), to study RD size and organization. We wanted to be able to directly compare the super-resolved images to the well characterized picture of RDs captured by confocal microscopy, and therefore decided to perform correlated confocal and GSDIM imaging on fluorescently labeled RD.

3.1.1 *In vivo* scrape replication labeling of RDs using ATTO 633-dUTP

For replication domain imaging, I labeled RDs in living normal rat kidney epithelial (NRK) cells with an adapted *in vivo* scrape labeling protocol, which allows high density fluorophore labeling with very low background (Schermelleh et al., 2001). The concept is to disrupt membranes of attached cells mechanically by scraping them off their attachment surface, while exposing them to a short pulse of dye-conjugated nucleotide precursors. The intracellular replication machinery is thus flooded with dye-conjugated nucleotide precursors for a short period of time and incorporates them into the DNA backbone, yielding fluorescently RDs labeled at the co-replicating origins at the moment of the pulse.

Scrape labeling is only efficient using hydrophilic fluorophores, which are not absorbed by cellular membranes. I have tested a series of commercially available dye-conjugated nucleotide precursors, and have found ATTO 633-conjugated dUTP to be the best candidate for the combination of GSDIM imaging and the scrape labeling protocol.

NRK cells were synchronized to the G1 to S-phase transition by mitotic shake-off followed by aphidicolin treatment for 10 h. 15 minutes after aphidicolin washout, the cells were scraped with a rubber policeman in the presence of 67 µM ATTO 633-dUTP. By culturing replication labeled cells through several divisions, we could see the numbers of labeled chromosomes in nuclei diluting out with every cell division, eventually resulting in nuclei with only a single chromosome territory (CT) labeled, as described by: (Zink et al., 1998) (Edelmann et al., 2001). When cells are washed timely after reattachment from scrape labeling, this live cell labeling method yields strongly labeled RDs and is almost free of background as can be seen in Figure 3-1. I took z-stacks of many live cells ($n = 71$), which had only a single labeled territory, using conventional confocal microscopy. An example is shown in Figure 3-1a. The stacks were taken with 90 nm pixels in xy and 400 nm pixels in z. From the images, I extracted average numbers and nearest neighbor distances of RDs per chromosome. Domains centers were detected in 3D using the 3D ImageJ Particle Detector (Sbalzarini and Koumoutsakos, 2005). For more details see the Methods chapter.

The results are displayed in Figure 3-1b,c. The analysis shows that there is, as expected due to variable chromosome sizes, a spread in the number of RDs counted per CT. The median is 22 RDs per territory and the typical 3D distance (center to center) between nearest neighbor RDs active at the time of labeling is approximately 800 nm.

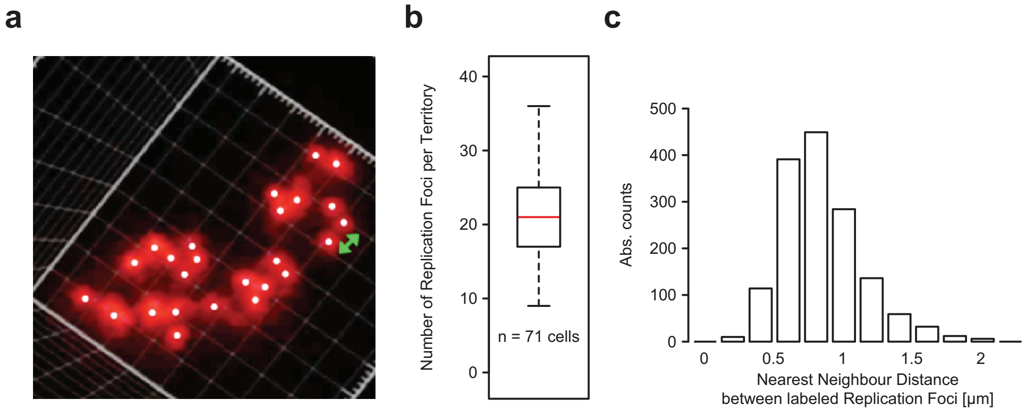

Figure 3-1: Single chromosome territories can be efficiently labeled by *in vivo* scrape replication labeling with ATTO 633-dUTP.
a, Representative confocal z-stack of ATTO 633-labeled replication domains (RD) from a cell nucleus with a single labeled chromosome territory (CT). White dots mark the centers of RD; green arrow marks the distance between two RD. **b**, Boxplot of RD number per CT, the median number is 22 RD per CT, from cells (n = 71) with single labeled CT. **c**, Histogram of nearest neighbor distances, measured for all RD (n = 1,518) from the 71 cells.

3.1.2 Visualizing the internal organization of RDs

At confocal resolution (lateral ~300 nm, axial ~750 nm), RDs appear as sub-diffractive spots without discernable substructure. Quantification of RD size measured by confocal light scanning microscopy (CLSM) can be found in the literature: Albiez *et al.* find them to be typically 500 nm in size (Albiez et al., 2006), and Maya-Mendoza *et al.* measured typical diameters of 350 nm (Maya-Mendoza et al., 2010). Even though it is not evident from confocal imaging *in situ*, RDs are macroscopic structures. They consist of small groups of replicons, most of which replicate DNA bidirectionally and thus harboring two replication forks. The group of replicons within the same RD initiate DNA replication synchronously during S-phase and it is therefore possible to label all replicons of a RD by catching them with a single short pulse of tagged nucleotide precursors (Huberman and Riggs, 1968) (Jackson and Pombo, 1998). The individual replication forks of a RD have been visualized and counted on single, stretched out DNA molecules using DNA combing (Huberman and Riggs, 1968) (Yurov and Liapunova, 1977) (Jackson and Pombo, 1998; Yurov and Liapunova, 1977). But until now, single replication forks have not yet been visualized *in situ*, in an intact nucleus.

We hypothesized that the stochastic super-resolution microscopy method of ground state depletion followed by individual molecule return (GSDIM) microscopy can be used to visualize individual replication forks within a RD inside fixed cell nuclei. We assumed that individual pulse-labeled replication forks within a RD are spaced far enough from one another so that they can be identified by GSDIM microscopy, which reaches lateral resolution up to 20 nm (Fölling et al., 2008).

We expected the unresolved diffraction limited structures, as which RD appear with confocal resolution, to deconvolve into multiple smaller domains, corresponding to those individual labeled forks with a distance above the resolution of GSDIM imaging. This idea is depicted in Figure 3-2. Figure 3-2a shows the cartoon of a chromosome, which was pulse-labeled by scrape labeling: Only RD active at the time of dye loading are labeled fluorescently, while others remain invisible (compare with Figure 3-1a for a representative confocal image). Figure 3-2b and Figure 3-2c illustrate how the same labeled RD, consisting of a small group of replicons, looks under a confocal versus super-resolution microscope, which has approximately 10-fold improved lateral resolution.

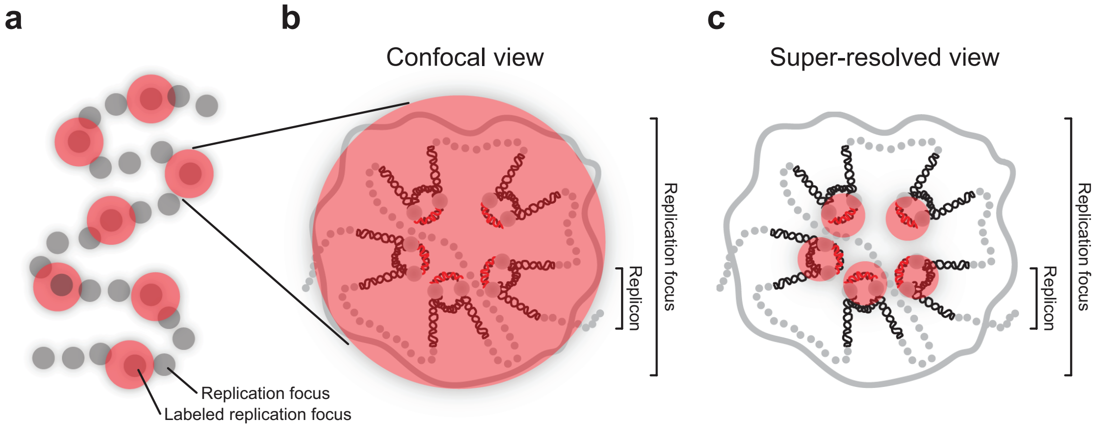

Figure 3-2: Pulse-labeled RD in hypothesized confocal and super-resolved view.
a, Cartoon of a chromosome labeled using replication scrape labeling. Only the subset of RD active at the time of loading is fluorescently marked. **b**, Each RD consists of several replicons which are simultaneously activated during S-phase and which co-replicate their DNA synchronously upon activation. With confocal resolution of ~300 nm, RD appear as sub-diffractive spots. **c**, Our hypothesis is that with super-resolution microscopy it is possible to resolve the individual replicons or replication forks which constitute a RD.

In order to be able to directly compare GSDIM images of labeled domains with confocal images, we performed correlative confocal laser scanning microscopy (CLSM) and GSDIM imaging. We assumed that the single RD correlative approach would help us to assess the gain in information provided by super-resolution imaging more easily. By having a direct comparison to the best possible confocal image of the very same RD, we would be able to better assess which information is likely missed by confocal microscopy.

For the experiment, I labeled cells by scrape replication labeling, using ATTO 633-dUTP as described earlier. All the cells were labeled 15 minutes after aphidicolin release. Therefore labeled RDs are part of early replicating euchromatin. For simplicity, I will refer to them as euchromatic domains throughout the thesis. Cells were plated on gridded dishes, fixed using 4% PFA in 1x PBS and imaged with CLSM in 1x PBS after washing.

I tested PBS compared to several concentrations of HEPES-based buffers, which are commonly used to fix cells for electron microscopy (EM) imaging of chromatin. We have found that PBS gives the best and least variable nucleus volume conservation of all tested buffers. Details and results of the comparison can be found in the Methods chapter.

The freshly fixed cells were imaged by CLSM on a Zeiss LSM780 ConfoCor. z-stacks of entire territories were acquired with an xyz resolution of 90x90x200 nm (first column of panels a-d of Figure 3-3). After confocal imaging, I noted grid-positions of each imaged cell, which allowed imaging the same cells for a second round on the GSDIM microscope.

The data presented in Figure 3-3 and Figure 3-4 were in parts acquired by Dr. Maria Julia Roberti, a postdoc in the laboratory. I want to acknowledge her important contribution, which was the acquisition of most of the GSDIM data presented in this thesis. I have processed and analyzed the GSDIM data. I have further carried out sample preparation and confocal imaging.

For GSDIM imaging, cells were transferred into a TRIS-HCl buffered solution containing GLOX/MEA, at pH 8.5. All GSDIM experiments were performed on a Leica SR GSD Microscope with active suppressed motion stage. The GSDIM microscope was operated in wide-field mode. For the GSDIM experiments, we used cells with typically 2 to 4 labeled territories. Midsections of CTs were imaged. Typical image sequences acquired have at least 30,000 frames. Event-lists were created from the raw image sequences using the Leica LAS AF 3.2 software.

All events with less than 500 photons were rejected from the event-list. Drift-correction was done by maximizing correlation between overlapping sequence segments using a script written by Anna Szymborska in the lab(Szymborska et al., 2013). Her script is the MATLAB-implementation of a published method (Huang et al., 2008). The drift-corrected images were reconstructed using a pixel-size of 10 nm. Images with strong drift, which could not be corrected, as assessed by Fourier-ring profiling (Banterle et al., 2013), were rejected from the analysis.

It is crucial in super-resolution microscopy to have a good estimate of the resolution that can be achieved in the specific labeling and imaging conditions. The typical method to estimate localization precision of stochastic super-resolution images is to measure full-width at half maximum of single isolated clusters of localization. In immunofluorescence experiments, these clusters are frequently found in the image background. Assuming that they correspond to signal from single antibodies/dye-molecules, they can be used for localization precision estimation. Scrape replication labeling does not yield this background. Therefore I looked for another way to estimate the resolution in our GSDIM images.

I decided to use the Fourier-ring correlation method, which is a standard method in single particle EM and has recently been proposed for use in super-resolution microscopy (Nieuwenhuizen et al., 2013) (Banterle et al., 2013). I have implemented the method proposed by Nieuwenhuizen *et al.* 2013 in a MATLAB-script. According to my calculations of Fourier-ring correlation curves (3σ-criterion), the final dataset for further processing had at least 50 nm resolution or better. For further details regarding processing of the GSDIM event-list for image reconstruction, see the Methods chapter.

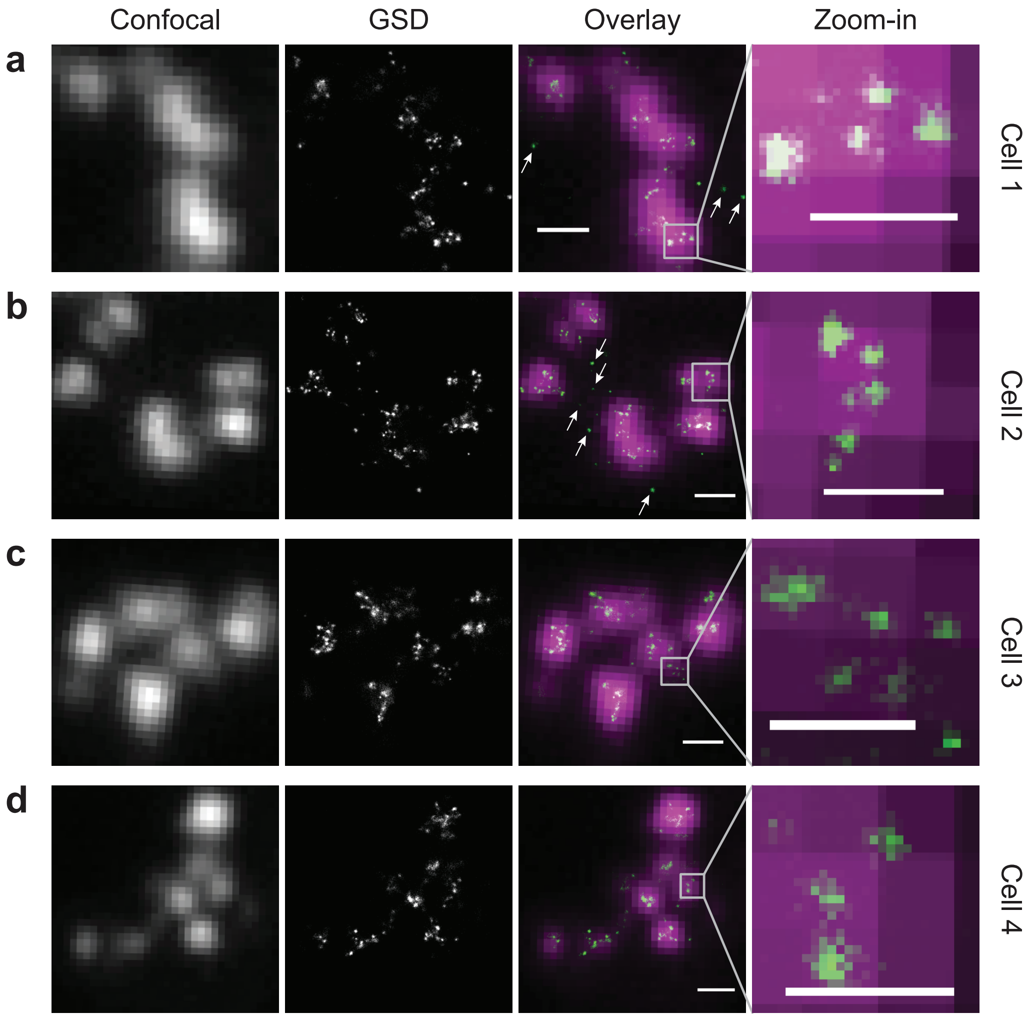

Figure 3-3: Examples of CT imaged using correlative confocal and super-resolution imaging.

a-d, Images of 4 different scrape-labeled CTs imaged by correlative confocal and super-resolution imaging. The fluorophore used in both confocal and super-resolution imaging is ATTO 633. Small groups of replication forks can be distinguished in the GSDIM images, while this substructure is not discernible from the confocal images. Solitary, unclustered replication forks are indicated by white arrows. Scale bars in column 3 are 500 nm, scale bars in column 4 are 200 nm. Results were obtained in collaboration with Maria Julia Roberti, details are given in the text.

Figure 3-3 shows 4 examples of cells imaged on both the Zeiss LSM 780 ConfoCor (column 1) and Leica SR GSD microscopes (column 2), the respective overlay (column 3) and a zoom-in of a single RD, consisting of multiple forks (column 4). To achieve exact overlay, the confocal image was rotated using a rigid-body registration algorithm, which seeks to maximize image cross-correlation between confocal and GSDIM image. The z-depth acquired by the GSDIM in wide-field mode is 800 to 1000 nm. The confocal microscope achieves higher z-resolution (~300 nm). In order to get overlays with a similar z-range, I decided to overlay each GSDIM image with a projected sub-stack (consisting of 5 z-slices) of the confocal data (200 nm z-spacing). In order to pick the best confocal sub-stack for overlay, the image cross-correlation was calculated between the GSDIM image and all possible 5-slice sub-stacks of each confocal z-stack, and the sub-stack with maximal cross-correlation with the GSDIM image was chosen for the final overlay.

GSDIM image preprocessing and analysis steps included event-list preprocessing, resolution estimation using Fourier-ring correlation, automated overlay of confocal and super-resolution images and peak detection and clustering in the reconstructed GSDIM images. Details of GSDIM imaging and image processing are given in the Methods chapter.

The overlays in Figure 3-3 show that GSDIM imaging is indeed capable of resolving substructures within RDs. Most of the RDs seen in confocal images each resolve into a group of spatially clustered intensity peaks in the GSDIM image, presumably representing individual replication forks, but potentially also small clusters (likely not more than pairs) of forks whose distance is below the resolution limit. A smaller fraction of the RDs could only be identified as separated RDs on the GSDIM images, and appeared as one bigger RD at confocal resolution. Replication forks are typically 30 to 50 nm in diameter, while a few bigger ones reach sizes up to 100 nm. Strikingly, a number of solitary unclustered replication forks, which are clearly detected by

GSDIM imaging, are hardly detected by confocal microscopy (e.g. as indicated by arrows in Figure 3-3a,b). Part of the reason is likely the limited dynamic range of the avalanche photo-diodes (APDs) used for detection on the confocal microscope, maximum counting rate 4 photons/ μs. Laser intensity for imaging was adjusted to avoid oversaturated pixels, while the short pixel dwell time ~8 μs used for live-cell imaging was applied. Since the range of RD intensities within a CT is large, weak signal from single forks was likely not detectable with the settings used.

3.1.3 Measuring RD size and quantifying replication fork number per RD

To quantify the GSDIM results, raw images (Figure 3-4a) were preprocessed by intensity thresholding and median filtering, see Figure 3-4b. The individual forks were detected using grayscale-dilation and clustered into RDs using density-based clustering, see Figure 3-4c,d. Further details of the analysis are listed in the Methods chapter.

From the clustered forks, each representing a RD, I counted the number of forks per RD. The median number of forks per RD is 4, see Figure 3-4e. Solitary forks are not included in the RD count, but counted separately. I also measured the area of each RD (the convex hull of the respective forks for all clusters with at least 3 forks). The median area is 8,400 nm^2, see Figure 3-4f. Figure 3-4g displays the horizontal Feret-Diameter measured for each RD, again for all clusters with at least 3 forks. If considering the clusters with 2 forks as well, the median Feret-Diameter is 105 nm.

The quantitative analysis shows that most forks are clustered into RD. We find that 8,538 out of 9,766 forks detected in total cluster into small groups of at least 2 forks (87.4%). The remaining 12.6% of forks we find are solitary forks. This means that we count almost as many solitary forks as we count fork clusters: 1,228 solitary forks and 1,457 fork clusters were found in total.

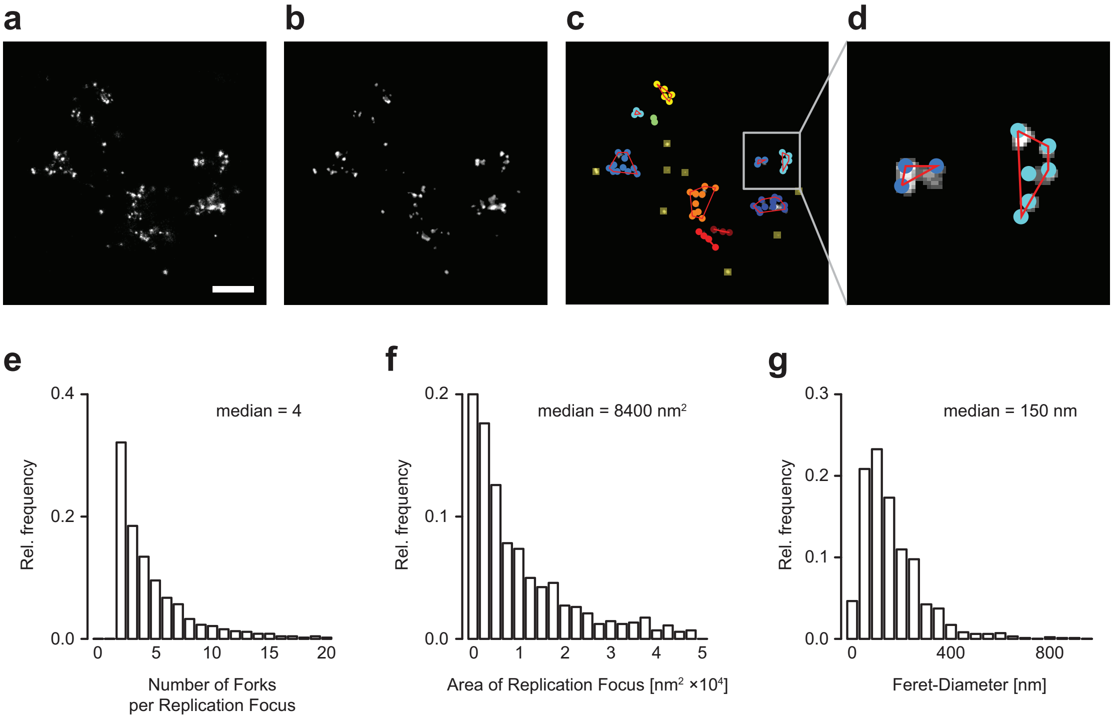

Figure 3-4: Quantification of RD Size and Replication Fork Number.
a, GSDIM image of a ATTO 633-dUTP pulsed chromosome after drift-correction (scale bar: 500 nm). **b**, Preprocessed GSDIM image after filtering and intensity thresholding. **c**, Density-based clustering of detected forks to RD. Forks assigned to the same clustered are marked in the same color. Yellow translucent squares mark unclustered, solitary forks. **d**, Zoom-In on panel c. Red lines denote the convex hull around the centers of detected forks. **e**, Histogram on number of forks counted per RD from n = 87 chromosome territories in 37 cells. **f**, Histogram on RD area. **g**, Histogram on horizontal Feret-diameter of RD.

In summary, we were able to visualize individual replication forks or small fork clusters using GSDIM imaging of intact *in vivo* pulse-labeled nuclei. I was able to quantify the number of forks per RD and measure RD dimensions. Most forks cluster into groups, but interestingly there is also a significant fraction of solitary forks. We could further show that most of the single forks cannot be detected by confocal microscopy. Our data suggest a RD organization that differs from studies suggesting that RD typically harbor 6 replicons or 12 forks(Jackson and Pombo, 1998). A more exhaustive discussion is provided in the Discussion chapter.

3.2 Nearest neighbor distance measurements between RDs

The size measurements of replication domains we obtained using GSDIM imaging bridged a gap in our knowledge of chromatin as a higher order polymer. We now understand that RDs vary in size, spanning from below 100 nm to over 400 nm, with most of the measured RD being rather small (median of 150 nm), well below the diffraction limit of conventional light microscopy.

Interestingly, the literature so far reported that the spacing between nearest neighbors of RD is similar to their size. Both the median size of RD and the distance to their next neighbor were estimated to be ~350 nm using confocal microscopy. The authors concluded that RD must lie very close or even be touching their immediate neighbors (Maya-Mendoza et al., 2010). Since our data clearly shows that replication domains are significantly smaller than 350 nm, this immediately raises the question whether the picture of close or touching RD is actually accurate. We asked if RD might actually really be located rather far apart from each other relative to their size. This would imply that there are extended linker regions of DNA between RD.

In order to answer this question, we needed to find out if we could verify the reported nearest neighbor distance measurements. I decided to measure the nearest neighbor spacing between RDs in NRK cells, the same cell line we used to measure replication domains sizes, stably expressing PCNA-eGFP (described in more detail in section

3.4.2). I used double-color labeling of replication domains active one hour after another to mark neighboring RD and to measure their respective distances, as others have done before (Manders et al., 1996) (Ma et al., 1998) (Maya-Mendoza et al., 2010).

It is known that there is a clear temporal program for genome replication and that, once replication initiates in early S-phase, genomic neighboring RDs are replicated one after another. Once a replication domain finished replication – this is when all its internal forks have met – replication will be initiated in its neighboring RD (Ma et al., 1998) (Maya-Mendoza et al., 2010). It was found that the complete replication of RDs in different mammalian cells takes about 45-60 minutes (Nakamura et al., 1986) (Manders et al., 1992) (Jackson and Pombo, 1998) (Ma et al., 1998). By performing pulse-chase-pulse labeling in which two pulses of nucleotide precursors attached to different dyes are introduced with appropriate waiting times, it is possible to preferentially label neighboring RD along the chromatin fiber. The concept explained above is visualized in the cartoon below, see Figure 3-5. In the cartoon, I depict a simplified scenario, in which all RD active at a time are completely synchronized and all get fully replicated within 60 minutes.

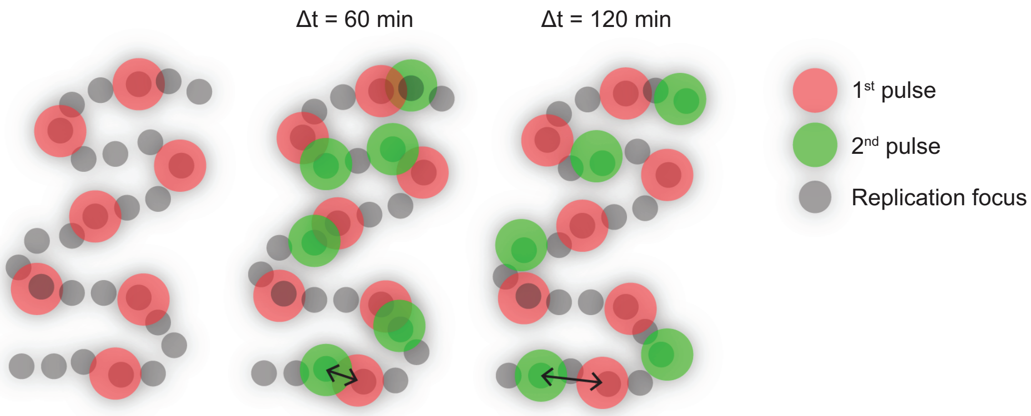

Figure 3-5: Double color labeling of genomic neighboring RD using increasing chase times yield pairs of increasing distance with increasing waiting time between pulses.
The cartoon depicts progression of DNA replication in early S-phase. After a first pulse of labeled nucleotides, a first set of RD gets labeled (red). After a waiting time, the second labeling-pulse marks the neighboring RD (green). The resulting pattern is spatially associated domains doublets. Black arrows indicate the increasing distance between consecutively labeled RD with increasing chase time between pulses.

I synchronized NRK cells to the G1 to S-phase transition using a mitotic shake-off, followed by aphidicolin treatment. Then, I released the cells for 15 min from aphidicolin to expose them to a first pulse of ATTO 633-dUTP. After a waiting time, I exposed the cells to a second pulse of labeled nucleotide precursors, this time ATTO 565-dUTP to label pairs of immediately neighboring RD along the fiber preferentially. I waited 60 minutes between pulses, since this is the time reported for one RD to be fully replicated. This procedure presumably yields labeling of direct neighbors along the fiber in 2 different colors. After labeling, I further cultured the cells for ~48 h, allowing them to go through 2-3 divisions before they were fixed for imaging. Cells were directly mounted on coverslips for imaging. For the live cell labeling approach, no immunofluorescence staining step using antibodies, for which cells would require permeabilization, is needed. Thus, it minimizes the disruption of the fragile nuclear structure. The detailed protocol is listed in the Methods chapter.

z-stacks of double-labeled nuclei were acquired on a ZEISS LSM 780 ConfoCor with 50x50x150 nm spacing. The stacks were deconvolved using Huygens SVI, and detecting domains centers in 3D was done using IMARIS Bitplane v2.6. The RD center positions in both colors were read out and pairs of nearest neighbors between domains of the two channels were assigned. The last step was done using MATLAB 2010b. For detailed protocols please refer to the Methods chapter.

The result is presented in Figure 3-6. For a waiting time of Δt = 60 min between the two labeling pulses, we find the median nearest neighbor distance between doublets of red and green RD to be 270 nm. The distribution of nearest neighbor distances along the chromatin fiber is broad: They range from complete overlapping domains centers to distances up to approximately 600 nm

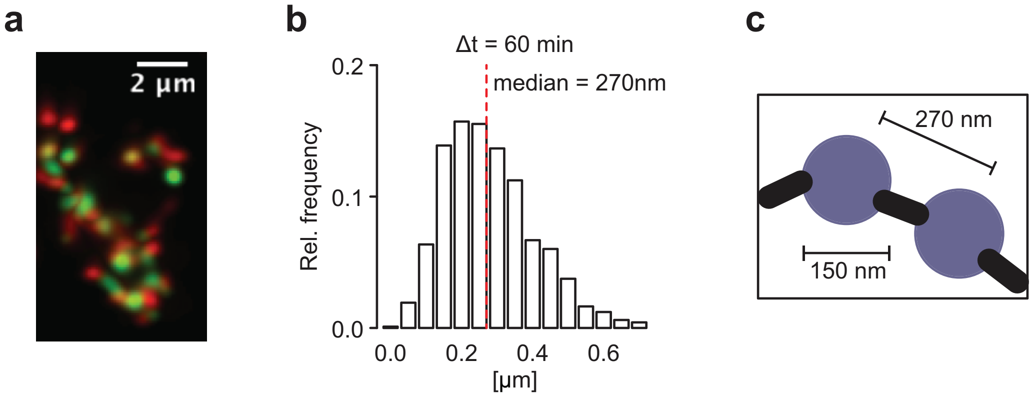

Figure 3-6: Measurement of nearest neighbor distances between pairs of ATTO 633 and ATTO 565-dUTP labeled RD.
a, Example of chromosome labeled with pulse-chase-pulse labeling protocol with waiting time Δt = 60 min; max. intensity projected z-stack after deconvolution (50 nm pixels in xy, 150 nm pixels in z). **b**, Histogram showing the nearest neighbor distance distribution measured between domains pairs of different color. 2,711 pair distances measured in total from 16 cells. **c**, Median RD nearest neighbor spacing is significantly larger than median RD size.

The distances we measure between immediate neighboring RD in our data are only a little smaller than what was reported earlier (median of 270 nm as compared to 350 nm). Clearly, the median distance between neighboring domains we measured is significantly bigger than our measured median replication domain sizes. With a median RD size of 150 nm, compared to the median spacing of 270 nm, this leaves significant space between RDs. And it leads us to hypothesize that there are potentially linker regions of DNA between RDs, whose DNA is more spatially extended than the DNA within RDs. I am addressing the implications of this result in light of a new study, which found a clear correspondence between RDs with topologically associating domains (TADs), in the Discussion chapter.

In the Discussion chapter I am further addressing our efforts to estimate chromatin persistence length at the scale of RDs by live imaging of neighboring RDs.

3.3 Investigating RD compaction upon ATP depletion

In the last chapter, I have presented our finding that the typical RD spacing is significantly larger than the typical RD diameter, suggesting that there must be extended linker regions of DNA between RDs.
This intuitively raises the question how chromatin composed of a linear chain of compact domains and extended linkers undergoes large-scale compaction. It is an intriguing question, since a change in chromatin compaction state is commonly associated with important physiological processes. For instance, it is known that chromatin changes compaction state during differentiation (Sinclair et al., 2010) (Meshorer, 2008; Talwar et al., 2013) and in response to DNA damage (Hamilton et

al., 2011; Kruhlak et al., 2006; Ziv et al., 2006). It is further known that cells actively limited the compaction level. When ATP is depleted, bulk chromatin undergoes additional compaction and dense regions accumulate preferentially at the nuclear periphery and around nucleoli (Lleres et al., 2009) (Martin et al., 2007). Chromatin condensation upon ATP depletion is furthermore associated with increased nuclear Ca^{2+}-levels. It is assumed that calcium binding changes the ionic balance between the negatively charged phosphate backbone of DNA and the positively charged histones (Visvanathan et al., 2013) (Martin et al., 2007).

Figure 3-7 shows my results on quantifying volume reduction in a labeled CT in response to ATP depletion. I observed a median volume reduction by 37%. This number is consistent with reports in the literature measuring bulk chromatin volume compaction of ATP-depleted cells (Martin et al., 2007). Controls are shown in the Appendix.

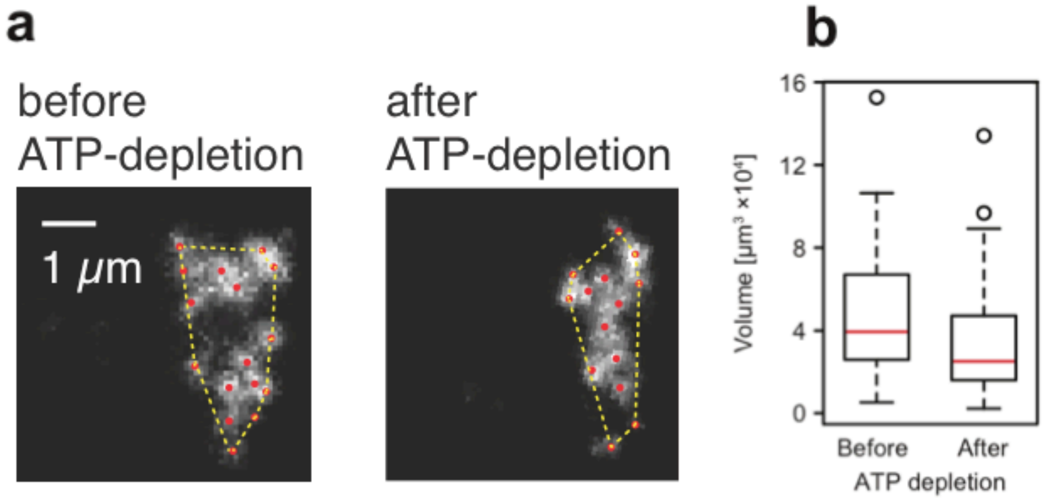

Figure 3-7: Chromatin volume of CTs decreases upon ATP depletion.
a, Z-stacks of single labeled CT in living cells were imaged before and after ATP depletion. Red circles indicate center of RDs, yellow dotted line is the convex hull around all RD centers **b**, The median volume of the CT convex hull

reduced by 37% percent calculated from n = 49 cells, $P = 0.016$ using Kolmogorov-Smirnov test.

Our results presented in sections 3.1 and 3.2 have shown that typical RD spacing is larger than the typical RD size. We have concluded that there must be linker regions of DNA between RD that are less compacted compared to chromatin within RD. This led us to hypothesize on how chromatin could undergo compaction. Two possible scenarios are shown in Figure 3-8. The cartoon in panel “a” depicts the first hypothetical scenario: Volume reduction by global, uniform chromatin condensation. In this picture, the DNA fiber would shrink uniformly across the territory, like a polymer immersed into poor solvent. Panel “b” depicts the second scenario: Volume reduction by preferential linker compaction. In this scenario, extended linker regions between RD are preferentially affected by ATP depletion compared to chromatin within RD. The main volume reduction is caused by linker shortening. While this model attributes the volume change mainly to condensation of linker regions, it does not exclude the possibility of mild compaction of RD.

Chromatin compaction can be quantified by fluorescence-based methods, such as FLIM-FRET (Lleres et al., 2009), molecular flow (Hinde et al., 2012) or by measuring penetrance of large fluorescent molecules (Görisch et al., 2005). However, these methods are designed to study bulk chromatin compaction differences. They do not allow for distinguishing between the two presented scenarios, since they cannot distinguish between compact RDs and linkers.

In chapter 3.1 I have presented our results on GSDIM imaging of internal RD organization. We were able to visualize small clusters of replication forks within replication domains. With GSDIM imaging, we therefore now had a tool in hand to test if the internal organization of RDs changes after ATP depletion induced compaction.

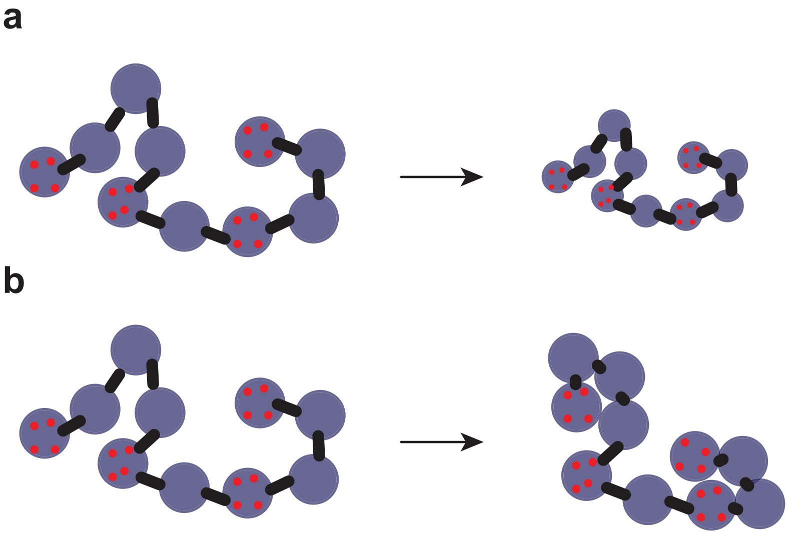

Figure 3-8: Two models of chromatin compaction upon ATP depletion
a, Model 1: Uniform, global polymer shrinkage causes chromatin volume reduction. This model predicts a decrease in both nearest neighbor distance between replication forks and RD area. **b**, Model 2: Linker condensation causes non-uniform chromatin compaction. Purple spheres represent replication domains; black bars represent extended inter-RD linkers; red dots represent fluorescently labeled replication forks.

The two models of chromatin compaction make clear predictions of what one would expect to see under the GSDIM microscope. The model of uniform, global chromatin compaction predicts a significant reduction in both replication domain area and nearest neighbor distance between the forks within one RD, see Figure 3-8a. In order to account for a 3D volume change reduction of 37%, the nearest neighbor distance between forks would have to decrease by $d_{1D} = 14.3\%$, with $d_{1D} = \left(1 - 0.63^{\frac{1}{3}}\right)$ and replication domain area would have to decrease by $d_{2D} = 26.5\%$, with $d_{2D} = \left(1 - 0.63^{\frac{2}{3}}\right)$.

I labeled cells as described in chapter 3.1. Before fixation for imaging, I depleted the cells of ATP for 30 minutes by immersing them into media containing 15 mM of sodium azide (NaN_3) and 30 mM 2-deoxy-D-glucose, blocking both the mitochondrial respiratory chain and glycolysis.

Dr. Maria Julia Roberti performed most GSDIM imaging experiments of the ATP-depleted cells, concomitantly with the control dataset of unperturbed cells presented in chapter 3.1. I have prepared the samples and performed GSDIM image processing and analysis as described in chapter 3.1.

My analysis shows that replication fork nearest-neighbor spacing decreased from a median of 63 nm in the unperturbed reference dataset to a median of 61 nm in the ATP-depleted cells, see Figure 3-9a. This is a very mild, but statistically significant decrease by 3.2% ($P = 2\times10^{-4}$, Kolmogorov-Smirnov test). Surprisingly, the median area of RDs increased significantly by 40% from a median of 8,400 nm^2 to a median of 14,200 nm^2 upon ATP depletion ($P = 9.7\times10^{-11}$, Figure 3-9b).

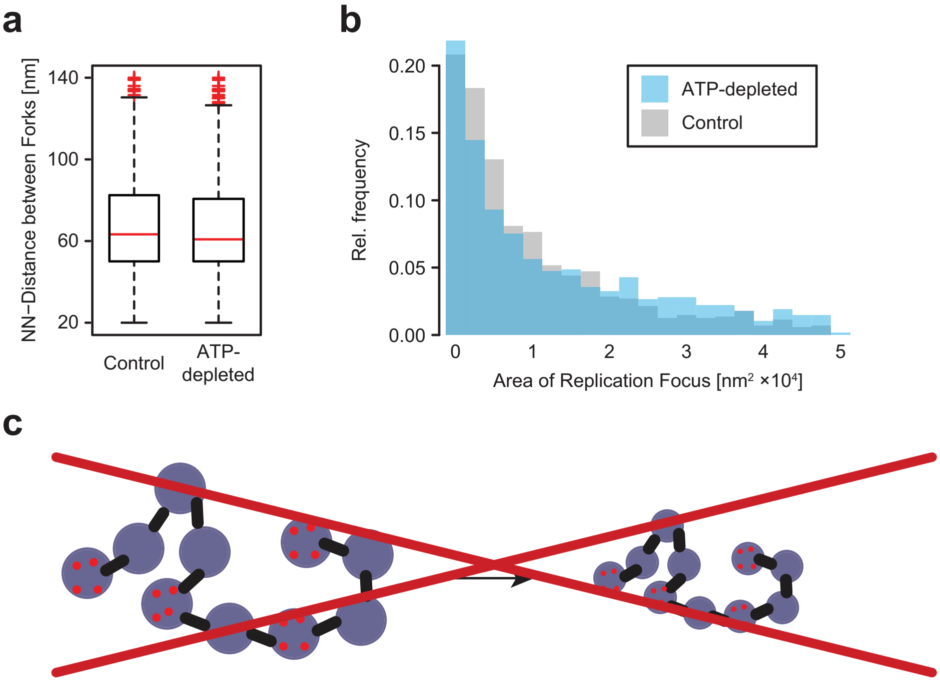

Figure 3-9: Large-scale chromosome compaction upon ATP depletion is not dominantly mediated by global, uniform chromatin condensation.
a, Median nearest-neighbor distance between replication forks decreases from 63 nm to 61 nm between control to ATP-depleted cells, change is significant ($P=2\times10^{-4}$, KS-test). **b**, The median area of RD increases from a median of 8,400 nm^2 to a median of 14,200 nm^2 upon ATP depletion ($P=9.7\times10^{-11}$). n=71 CT from 39 cells were imaged for the ATP-depleted dataset; n= 87 CT from 37 cells were imaged as the control dataset, from same dataset as shown in Figure 3-1. **c**, Data does not support a model of uniform chromatin condensation upon ATP-depletion. Data was produced jointly with Dr. Maria Julia Roberti.

Based on these findings, I exclude that the volume loss upon ATP depletion can be fully explained by uniform chromatin compaction that would also affect RDs. The measured 3.2% decrease in nearest neighbor spacing in 1 dimension translates into a volume reduction of $\mathrm{d}_{3\mathrm{D}} = 9.3\%$, $\mathrm{d}_{3\mathrm{D}} = 1 - 0.968^3$ and cannot account for the vast volume reduction by 37%, as measured by myself and others (Martin et al., 2007).

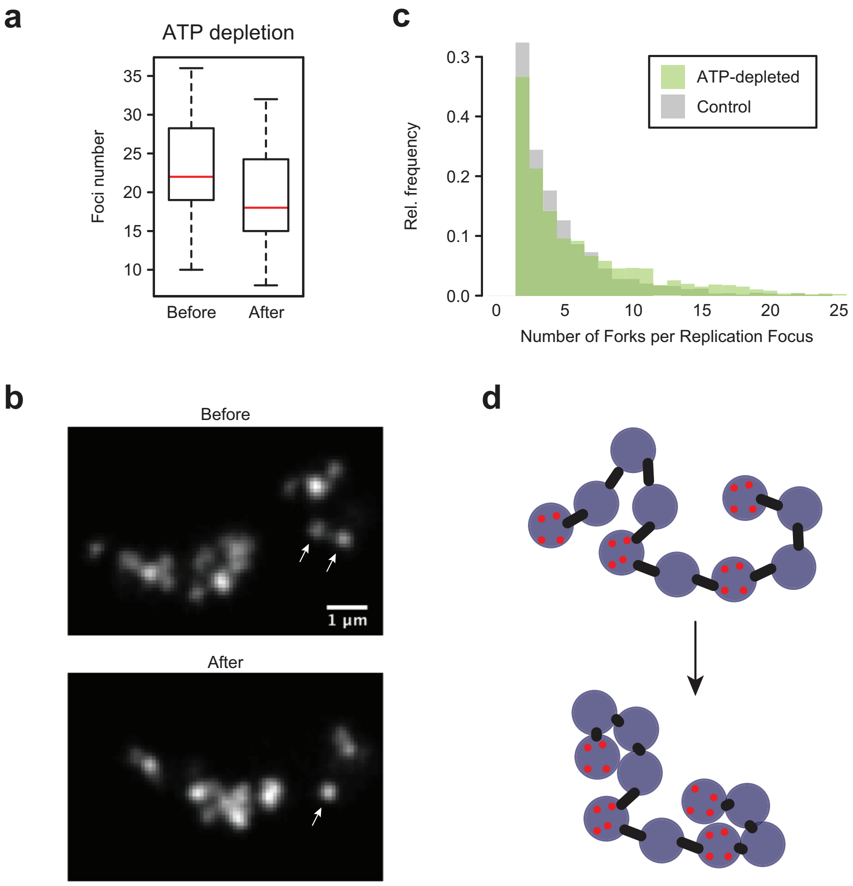

Figure 3-10: Global chromosome compaction upon ATP depletion is consistent with a model explaining volume loss by linker region contraction. **a**, RD number detected in confocal z-stacks of single labeled CT from living cells decreases significantly upon ATP depletion. Before ATP depletion, a median number of 22 domains are detected. After ATP depletion, the median number decreased to 18 domains per RD. The domains number decrease is significant ($P = 0.016$, KS-test). **b**, An example of a CT before and after ATP depletion is shown. Both a volume decrease and a decrease in the number of discernible RD can be detected. Smaller domains seemingly merge into larger ones (indicated by arrows). **c**, The number of replication forks per RD increases upon ATP depletion. There are less RD with fewer than 6 forks per RD and more RD with at least 8 forks per RD in the ATP-depleted cells compared to control, suggesting smaller labeled RD which have come close to each other are sometimes detected as one single big RD. **d**, We favor the second proposed compaction model which attributes the vast volume loss upon ATP depletion to contraction of previously extended linker regions between RD. Data was produced jointly with Dr. Maria Julia Roberti.

Model 2 offers a simple explanation for the seemingly counterintuitive result of almost unchanged nearest-neighbor spacing of replication forks within RDs and almost 40% increased RD area. When linker regions contract, they bring formerly distally spaced RDs closer together. In the unperturbed state, two adjacent RDs would be clearly separated spatial units. In the ATP-depleted state, they would have come so close that they are perceived as one larger "fused" RD and lead to a seemingly increased RD area. The model also predicts that number of replication forks per RD detected must also increase. Indeed, we find that a larger numbers of RDs contain 8 or more forks in ATP-depleted cells compared to control, see Figure 3-10c. This change in replication fork number per RD is significant ($P = 5\times10^{-7}$, KS-test).

The 'merging' of fluorescently labeled RD by non-uniform compaction can also be observed in live cell experiments. Figure 3-10b shows an example of a single labeled CT before and after ATP depletion. The number of discernible RDs has decreased upon ATP depletion. On the lower right of the confocal image, two small and dim domains spaced almost 1 μm apart before ATP depletion appear as one bright focus after ATP depletion (indicated by arrows). The quantification of RD number discernible in confocal z-stacks of the same cells before and after ATP depletion is shown in Figure 3-10a. 49 cells with single labeled territories were used for the analysis. The same dataset was used to calculate the volume reduction shown in Figure 3-7b. The median number of detected domains decreased significantly from a median of 22 to a median number of 18 domains per territory (KS-test; $P = 0.0155$). In conclusion, all our findings are consistent with a model in which preferential condensation of linker regions is the dominant mechanism of non-uniform chromatin compaction.

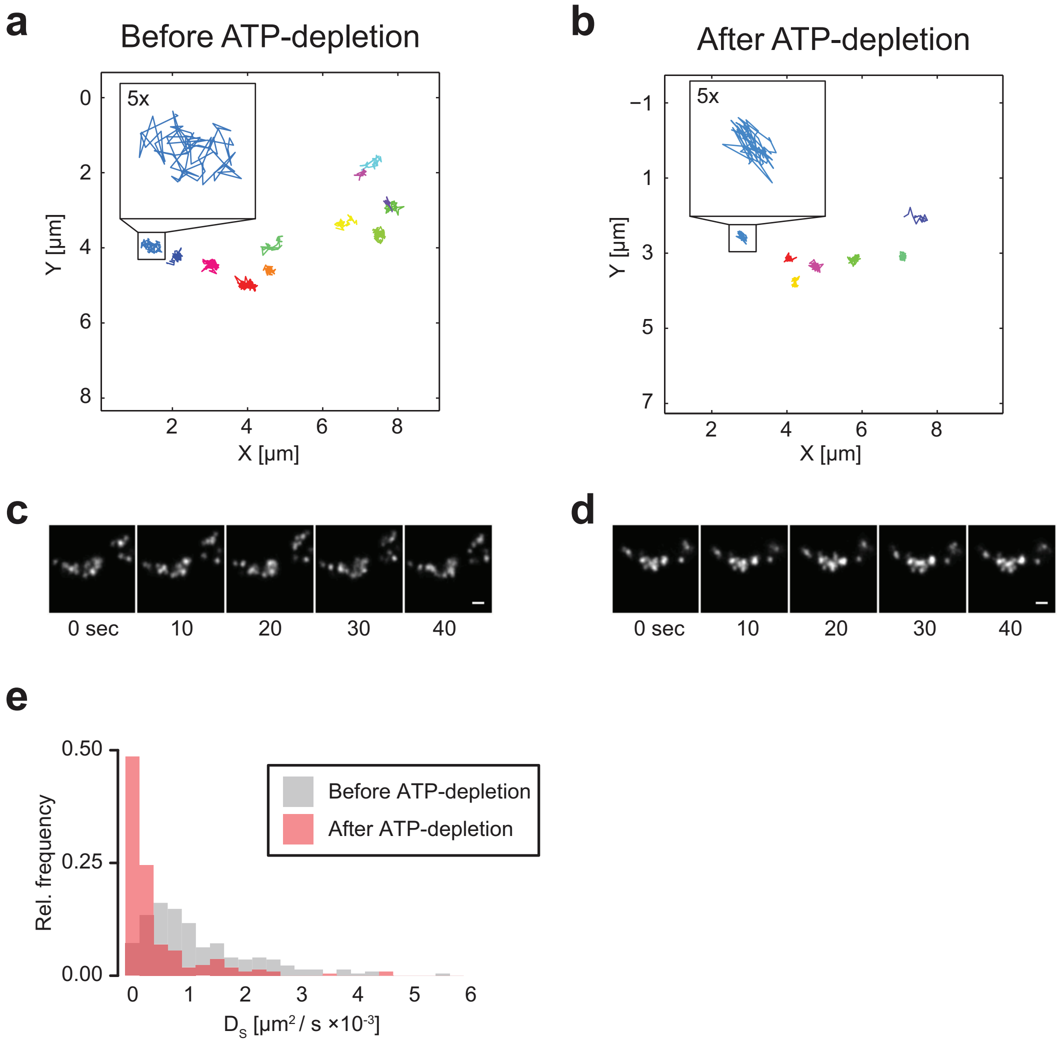

Figure 3-11: RD mobility is reduced upon ATP depletion.
a, Time-projected trajectories of RD movement from a single labeled CT, tracked on confocal time-lapse movies with 2 Hz sampling, an exemplary sequence is shown in **c**. **b**, Time-projected trajectories of RD from the same cell, an exemplary sequence is shown in **d**. As previously addressed, RD number decreases upon ATP depletion and mobility of remaining 'merged' RD is clearly decreased. **e**, Median diffusion coefficient D_S before ATP depletion was $D_S = 1.09 * 10^{-3} \mu m^3/s$ and decreases significantly to upon ATP depletion to $D_S = 0.24 * 10^{-3} \mu m^3/s$ ($P = 2.6{\times}10^{-35}$, KS-test). Movies acquired from $= 42$ cells before and after ATP-depletion.

I also monitored if there is a change in chromatin dynamics upon ATP depletion by taking time-lapse movies of single labeled territories before and after ATP depletion see Figure 3-11; the methodology is described in more detail in the following chapter). The results clearly confirm the previously reported ‘freezing’ of chromatin mobility upon ATP depletion, see Figure 3-11e (Zidovska et al., 2013). In the framework of our model, one can imagine that the linker regions stiffen upon retraction and cause the slow-down of RD movement. I also collected a control data set of n = 16 cells in which RD were tracked before and after changing them into fresh imaging buffer without ATP-depleting reagents. These cells did not show a significant mobility change. Their quantification is shown in the Appendix, see Figure 5-3.

In summary, we were able to measure the compaction state of individual RDs upon ATP depletion, by imaging fluorescently labeled RD with GSDIM microscopy. Only about a quarter of the total volume decrease can be explained by a very mild shrinkage of the size of individual RDs. However we see fusion of adjacent RDs, a decrease in the total number of spatially distinct RDs and an decreased mobility. We therefore propose that the dominant part of energy loss induced chromatin compaction is mediated by the contraction of linker regions between RDs. In a recent study, the authors report compelling evidence that the newly discovered TADs are identical to the long-known RD (Moindrot et al., 2012; Pope et al., 2014). In light of this report, the extended linker regions between RDs, which we propose likely represent the boundary regions between TADs in Hi-C chromatin interaction maps. We have hypothesized in chapter 3.2 that these linker regions are less compacted than chromatin within RD in the unperturbed state. Our observation of non-uniform chromatin compaction upon ATP depletion suggests that this more open chromatin configuration in linker regions is particularly sensitive to ATP depletion.

3.4 Replication domain dynamics in live cells

In the previous chapters, I have presented our measurements on size and spacing of RD. In the following chapter, I present our results on the dynamics of these basic structural subunits of chromatin in living cells. Arguably, the dynamic picture is so far the least understood aspect of chromatin organization.

Useful insight has come from previous live cell studies of chromatin organization. Many of these have focused on movement and turnover of DNA-associated proteins by fluorescence-correlation spectroscopy, photobleaching and photoactivation techniques (Phair and Misteli, 2000) (Görisch et al., 2005). Another set of live cell experiments has studied the dynamics of single fluorescently-labeled genomic loci (Chuang et al., 2006) (Levi et al., 2005) (Bronstein et al., 2009). These studies describe observed chromatin dynamics as sub-diffusive, with few reports on apparent ATP-dependent directional movement of single genes over the distance of micrometers. While the idea is highly interesting, it is not easily reconciled with the picture of generally very the static chromatin, leaving many open questions.

We wanted to systematically study general chromatin dynamics and were asking the following questions in specific: What is the range of RD dynamics across the nucleus? Is there a gradient of dynamics from the gene dense, transcriptionally more active interior of the nucleus to the periphery? And is the surface of chromosome territories (CT), which has also been described as particularly transcriptionally active, and potentially exposed to “open” interchromatin space dynamically different than more interior regions? Also, how does RD size influence RD dynamics?

For the live cell imaging experiments, we labeled the cells with a pulse of ATTO 633-dUTP, as previously described. The detailed protocol is given in the Methods chapter.

We decided to image both euchromatic and heterochromatic domains to assess the range of chromatin dynamics that can be found in the nucleus. By adjusting the waiting time between aphidicolin washout from the G1/S synchronized cells and exposure to the pulse of labeled nucleotides, it is possible to specifically label either early replicating euchromatin or mid/late replicating heterochromatin. S-phase in PCNA-eGFP NRK cell-line takes 6 to 10 h to complete. To label early replicating euchromatin specifically, we waited 15 min after aphidicolin washout and 3.5 h for mid-replicating heterochromatin. Further culturing of labeled cells over several divisions eventually resulted in nuclei with only one labeled territory, which we used for imaging.

3.4.1 Live Cell Imaging of RD Dynamics

To establish a first reference dataset mapping global dynamics of native chromatin subunits across the nucleus, I acquired confocal time-lapse sequences of 300 frames sampled at 2 Hz (spanning a time of 150 s in total) with 90 nm pixel-size of 121 individual chromosome territories in single cells with labeled euchromatin, and of 20 territories/cells with labeled heterochromatin. The details of the custom-written analysis pipeline are found in the Materials and Methods section 2.3.2.1.

A major challenge was to perform the live cell imaging experiments without perturbing chromatin structure because of its high sensitivity to phototoxic effects (Belmont, 2006). In the beginning of my experiments, I consistently observed a reduction in RD number and CT volume with increasing time after imaging. The effect was strongest ~30 min after exposing labeled cells to the laser.

Laser-excited fluorophores are prone to react with molecular oxygen, forming free radicals that damage biological structures. We have chosen a dye with a long excitation wavelength in order to lower phototoxicity effects. To further prevent any light induced change to structure or dynamics of chromatin, I adapted the imaging protocol in 2 key steps. Total light dose on the sample by the time-lapse movie was always kept below 5 $\mathrm{J/cm^2}$ and oxygen concentration at the bottom of the labtek dish was reduced to 5%, details are given in the Methods chapter 2.2.1.1.

Since RD dynamics is sub-diffusive and step-sizes between time-steps of 0.5 s are typically only 100 nm, the tracking needs to reach high precision in order to output useful results. I could demonstrate that the tracker is capable to track RDs at a precision below 30 nm with the imaging conditions used in a set of 264 trajectories from 31 fixed cells. The full tracker characterization can be found in the Methods Section 2.3.2.1. Exemplary time-lapse sequences from two cells with euchromatic RDs labeled and two cells with heterochromatic RD labeled in single CTs are shown in Figure 3-12. The respective time-projected trajectories are shown to their right.

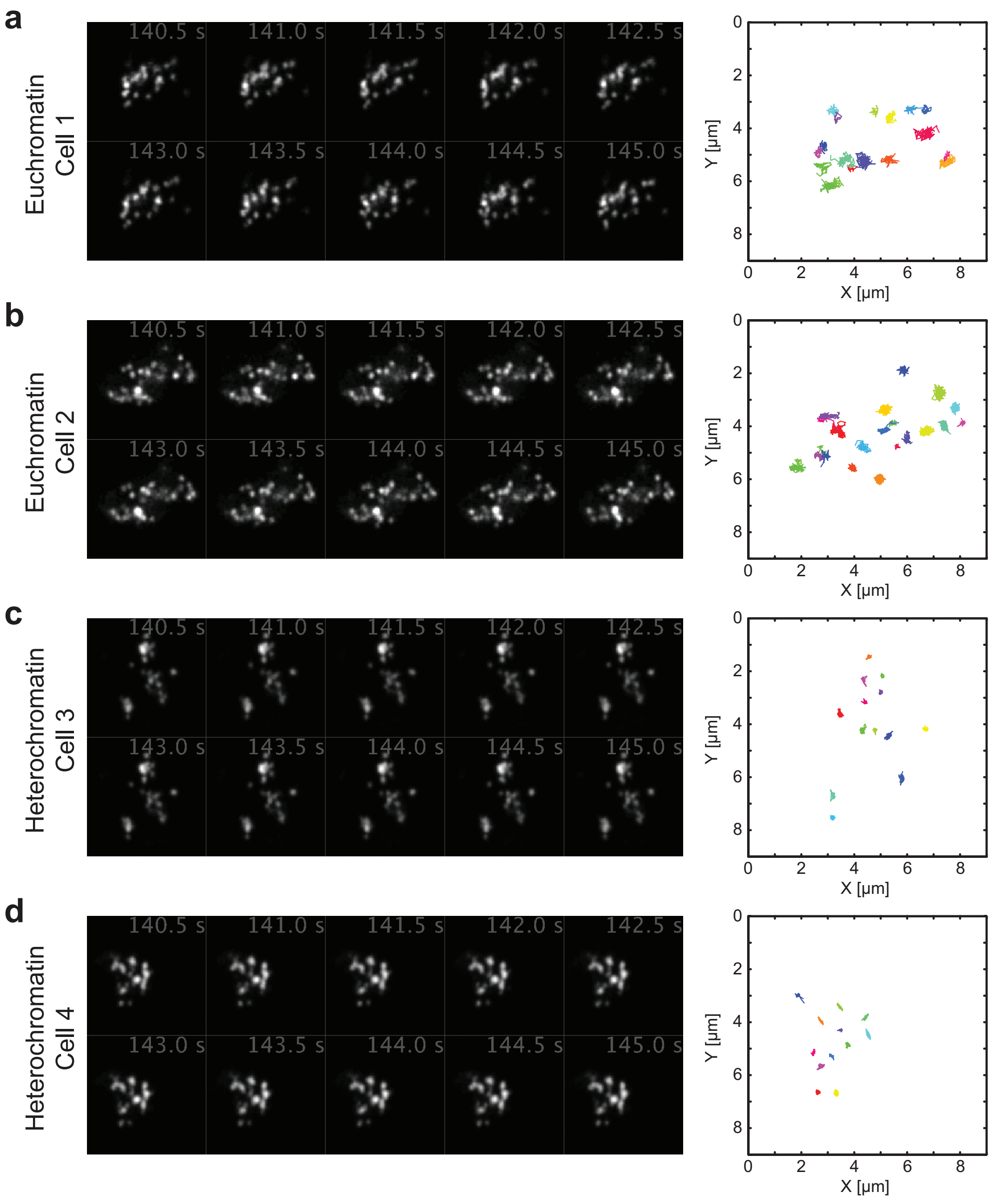

Figure 3-12: Tracking of individual RD in cell nuclei containing a single labeled chromosome.

a-b, Examples of ATTO 633-dUTP labeled early replicating RD, labeled 15 min after aphidicolin release. **c-d**, Examples of ATTO 633-dUTP labeled mid/late-replicating heterochromatin, labeled 3.5 h after aphidicolin release. Time-lapse movies from a single z-plane were recorded with CLSM, and were recorded for 300 frames over a timespan of 2:30 min in total (sampled at 2 Hz). Exemplary montages of ten frames from each movie are shown on the left. RD were detected and tracked using a self-written algorithm. The resulting time-projected trajectories of each RD are shown on the right.

The trajectories outputted by the tracker were analyzed with mean-square-displacement (MSD) analysis. A visualization of the analysis is shown in Figure 3-13. The MSD curve can help to distinguish between different categories of diffusive motion. The MSD $< r^2(\Delta) >$ is calculated by averaging all squared particle displacements for increasing lag times $\Delta = n * \tau$, where τ is the sampling interval and n is the increasing integer. N is the number of trajectory frames.

$$< r^2(\Delta) > = \frac{1}{N-n} \sum_{m=1}^{N-n} [\vec{r}\big((m-1)\tau + \Delta\big) - \vec{r}((m-1)\tau)]^2$$

The slope of the MSD curve distinguishes purely diffusive motion from directional transport and sub-diffusive motion. If the observed particle is diffusing freely, the slope of the MSD curve depends linearly on time and will be exactly 1. When the MSD slope is non-linear, as for my trajectories, it can be described by $MSD = 4D * t^\alpha$ for a 2-dimensional trajectory. α represents the subdiffusion exponent and D a prefactor sometimes termed 'apparent diffusion coefficient'. It needs to be pointed out though, that the dimension of D does not have the unit of a diffusion coefficient, when α is not equal to 1.

I calculated the MSD curve with correlating pairs for each of my trajectories. I then fitted the MSD using a variance-weighted fit using the function $MSD = 4D * t^\alpha + c$, with c represents an MSD offset introduced by tracking imprecision. For each trajectory the variance of all squared distances for each time-lag used for averaging was calculated and used for weighting. In order to avoid noisy data-points on the far end of the MSD compromising the fit, only the first quarter of each MSD curve was used. Only trajectories longer than 40 frames were used for fitting. The fits yielded a subdiffusion exponent $\alpha = 0.47 \pm 0.39$. α was only calculated for trajectories longer than 40 frames, only fits with $R^2 > 0.95$ were used to calculate the mean of α (424 of 1,117 trajectories were used). To also extract information from the shorter trajectories, a short-range diffusion coefficient D_s was calculated by fitting the first four points of the MSD with a linear curve (Saxton, 1997), no fitting weights were used.

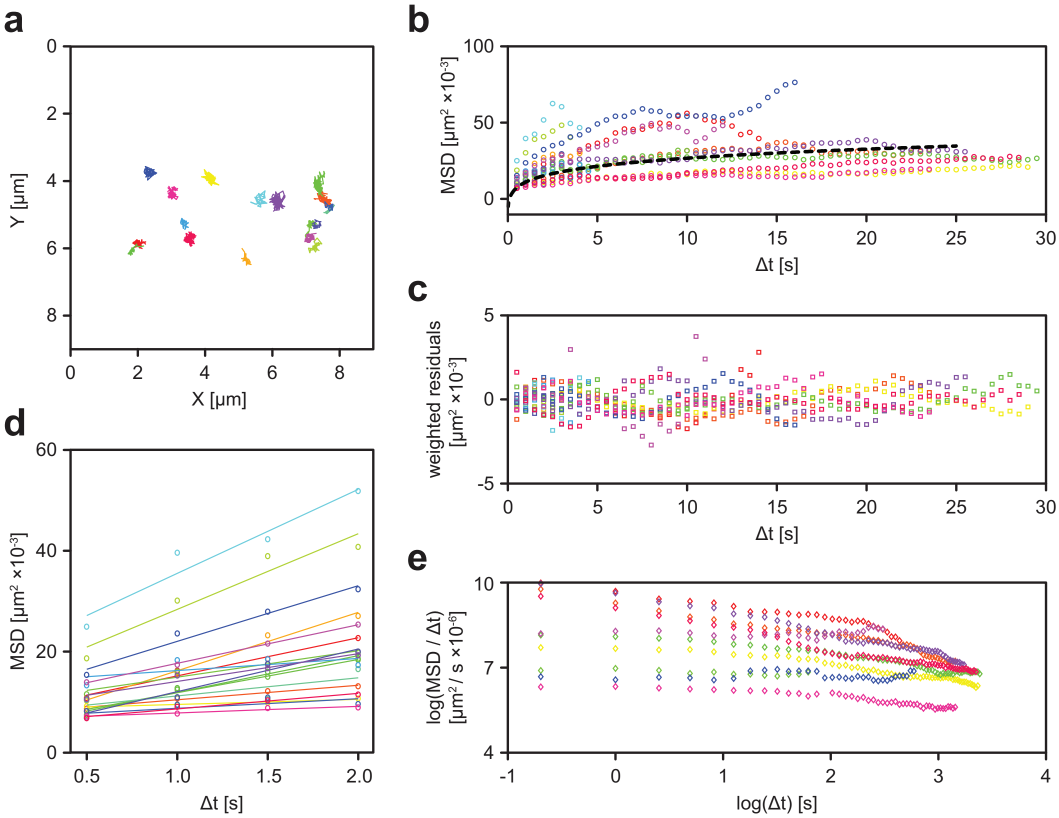

Figure 3-13: Mean-square-displacement (MSD) analysis, to extract short-range diffusion coefficient (D_s) and anomalous subdiffusion exponent (α) from trajectories.

a, Example of time-projected trajectories of a single CT, each track is displayed in a different color. **b**, Scatter curves are MSD curves calculated using correlated time-windows. The dotted black line indicates a fit f to the purple MSD curve, $f(\Delta t) = 4 * D * \Delta t^{\propto} + c$. **c**, Fitting-residuals; actual MSD subtracted from f. **d**, Zoom-in onto the beginning of the MSD curve; Lines indicate linear fits to the first 4 points of the MSD to calculate short-range diffusion coefficient D_S. **e**, Log-log plot to look at the time-dependent diffusion constant $\frac{MSD(\Delta t)}{\Delta t} = A * \Delta t^{\propto - 1}$. No indication of cross-over to free diffusion in time-range sampled.

I also plotted the log-log presentation of the time-dependent MSD, defined as $\frac{\mathrm{MSD}(\Delta t)}{\Delta t} = A * \Delta t^{\alpha-1}$. In this plot, one can detect a cross-over from constrained to free diffusion by change in the slope. The y-axis on the log-log plot represents $(\alpha - 1) * \log(A * \Delta t)$. In this formulation, it is evident that $(\alpha - 1)$ is the slope of the curve. Subdiffusion with $\alpha < 1$ results in a negative slope, while free diffusion would result in a slope of 0. A previous publication which found transient anomalous diffusion of telomeres has reported that the cross-over regime starts around 100 s (Bronstein et al., 2009). In the time range that my trajectories cover, I still have reasonable statistics up to a lag time of about 30 s and could not detect cross-over behavior of the trajectories in this time-range.

Running the tracker on our reference dataset from 121 cells with euchromatic RD labeled (introduced in 3.4.1) yielded 1,117 trajectories. Running the tracker on another 20 cells with heterochromatic RD labeled yielded 255 trajectories. Figure 3-14 shows a histogram of the short-range diffusion coefficient D_s extracted from all euchromatic and heterochromatic RD.

In my analysis I could confirm, that heterochromatic domains are mostly located close to the nuclear periphery and were significantly less mobile compared to the euchromatic RD (Chubb et al., 2002) (Pliss et al., 2009). This was a useful control, showing that the automated analysis pipeline works well to extract RD dynamics and assign their positioning within the nucleus, see Figure 3-15.

In my systematic study of global RD dynamics, I did not find evidence for directional movement, as previous studies investigating the dynamics of single loci at different time scales suggest (Levi et al., 2005) (Chuang et al., 2006; Zidovska et al., 2013). The only occasion on which I could observe directional and coherent motion in RD was upon photo-damage, which triggered large-scale chromatin compaction. This issue is further addressed in the Discussion chapter.

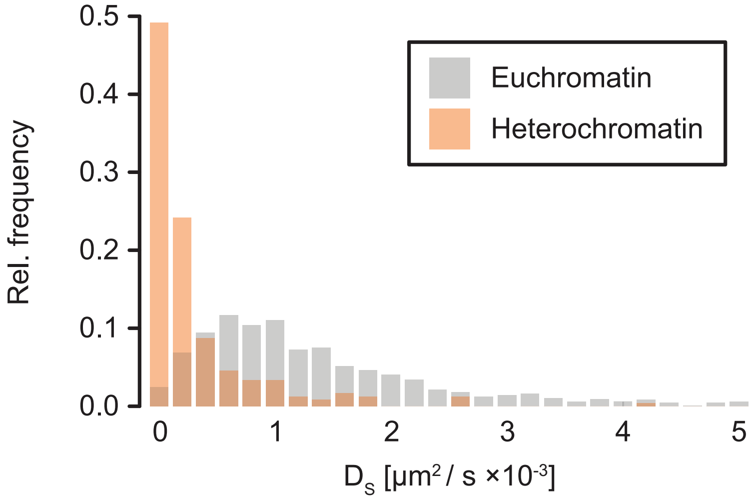

Figure 3-14 Diffusion dynamics of euchromatic RD compared to heterochromatic RD
Histogram of D_S extracted from all trajectories recorded for euchromatin (n = 1,117) median D_S = 1.15 $*10^{-3}\frac{\mu m^2}{s}$ compared to heterochromatin (n = 255) D_S = 0.19 $*10^{-3}\frac{\mu m^2}{s}$. Euchromatin shows significantly faster diffusion compared to heterochromatin ($P = 2.5 * 10^{-82}$, KS-test). Most heterochromatic RD are almost immobile.

3.4.2 Effect of RD intranuclear and intraterritory position and RD size on mobility

It was found in FISH experiments that smaller, gene rich CTs tend to be more internally located compared to bigger, gene poor CTs, which are more preferentially located close to the nuclear periphery (Bolzer et al., 2005). This finding can be recapitulated in polymer models of chromatin built based on chromosome conformation capture data (Kalhor et al., 2012). It is known already that chromatin associated to the nuclear periphery is less mobile than more internally located regions

(Chubb et al., 2002), and that it is mostly late replicating chromatin domains that associate with the nuclear periphery and are strongly constrained in diffusion (Pliss et al., 2009).

We were asking if the gradient of gene density across the nucleus impacts RD mobility and reflects in a gradient of dynamics from the nuclear periphery towards the center. Thus, in addition to each movie, I collected a z-stack of each imaged CT, which was used to calculate a rough estimate of the CT surface. Since the cell line expresses PCNA-eGFP, I could also collect a z-stack of the entire nucleus for all cells imaged. This allowed me to map the location of all tracked RDs relative to the nuclear membrane and nucleoli. In this way I was able associate each of the trajectories from the reference dataset with its intra-nuclear and intra-territorial position.

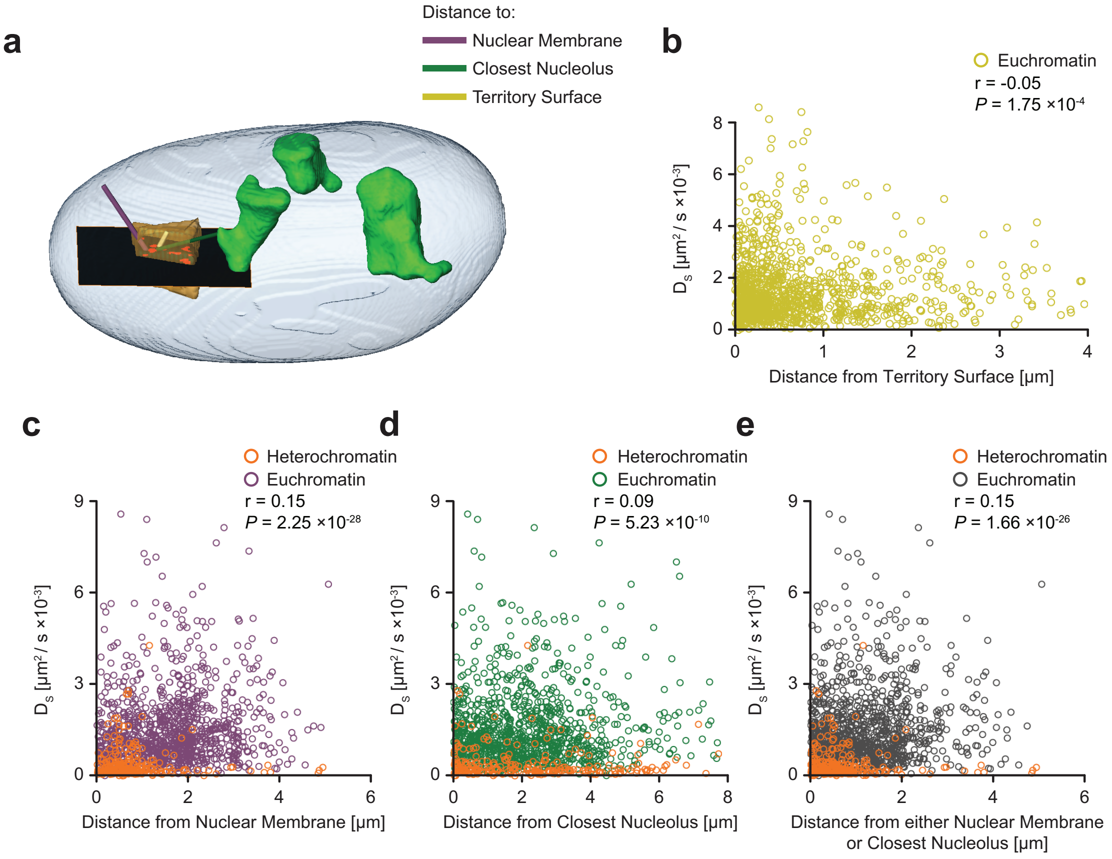

Figure 3-15: Intra-territorial positioning of euchromatic RD does not correlate with RD dynamics. Replication Timing rather than intra-nuclear position define RD dynamics.

A Schematics visualizing the segmentation of nuclear membrane (purple), nucleoli (green) and chromosome territory surface (yellow). The black plane represents the position where the 2D time-lapse of dynamic RDs (red) was recorded. Colored lines indicate respective measurements of 3D RD positioning relative to these landmarks. **b**, RD distance from CT surface does not influence euchromatin RD dynamics (yellow circles). Most heterochromatic RDs are immobilized at the membrane (orange circles). **c**, RD distance from CT surface does not influence euchromatin RD dynamics (purple circles). **d**, RD distance from closest nucleolus surface does not influence RD dynamics (green circles). **e**, Closest RD distance from either nuclear membrane or closest nucleolus surface (the shorter of these two distances was used) does not influence RD dynamics (gray circles). r = Pearson correlation coefficient (1117 euchromatin trajectories, 255 heterochromatin trajectories, point cloud is weighted by trajectory length); *P* = significance of correlation.

I could now investigate a possible correlation between positioning and dynamics. I confirmed that most heterochromatic RD are either located very close to the nuclear periphery or nucleoli and are presumably attached there, since many of them are almost completely immobilized. The analysis of euchromatic domains by contrast shows that they are dynamic across the entire nucleus, even in close proximity to the nucleus. I could detect a very mild gradient of diffusion coefficients within euchromatic RDs from nuclear membrane towards the center, Figure 3-15c-e, the effect is seen most strongly within a distance 0.5 μm from the nuclear periphery, but clearly the main defining parameter of chromatin diffusion is replication timing rather than intranuclear positioning.

A second question we had concerned the intraterritorial positioning of RDs. Many studies in the literature have identified the surface of chromosome territories to be a region of high gene density and transcriptional activity (Kurz et al., 1996) (Verschure et al., 1999) (Boyle et al., 2001). Nascent RNA is preferentially detected in this region. Unlike in the ICN model, where no distinction is made between 'interior' and 'outside' of a CT, The CT-IC model suggested fundamental differences between these two regions. We were interested to see if the higher transcriptional activity of the CT surface, which is also sometimes termed 'corona', results in a higher mobility of RDs located at the CT surface.

I have therefore mapped the 3D positions of all tracked domain within their territory. I have segmented the 3D outlines of the CTs using active contours and used the convex hull of theses outlines as an estimate for CT surface. I could not pick up a striking difference in dynamics depending on whether the focus was located more to the interior or surface of a territory, see Figure 3-15b. *P*-values associated to the correlation coefficients are not significant after correction for multiple testing according to Bonferroni. We also did not find a correlation of RD dynamics when comparing RDs on compact compared to more elongated CTs, or smaller compared to larger CTs. The full matrix of pairwise correlation plots can be found in the Appendix Figure 5-1, each trajectory in the data cloud is weighted by its lenght.

My estimation segmentation of CT surface is likely an underestimation, since it is calculated based only on the set of RDs labeled by the nucleotide pulse, and will thus miss unlabeled RDs not replicating at the time of the pulse, as well as extended linker regions, which would not be reliably detected by live cell confocal imaging. However, even though we likely undersegment the territory surface, our measurements clearly exclude a strong effect of intra-territorial positioning on RD dynamics.

The remaining features we wanted to test for correlation with dynamics were RD size, intensity and shape. For this purpose, I developed an object tracker, which not only tracks RD center positions, but also segmented the 2-dim RD outlines, extracting RD area, intensity and shape at every time-frame (example given in Figure 3-16a,b). I found that RD diffusion speed correlates mildly with all three features, see Figure 3-16c-e. Generally speaking, the bigger, brighter or more irregularly shaped a RD is, the slower it moves. Brighter domains are likely genomically larger RDs, since they consist of more labeled forks, which are believed to be regularly spaced across the genome. It is not a surprise that there is also strong correlation between size and brightness of RD. The result condenses to bigger RDs (genomically and spatially) being commonly irregularly shaped and moving slower compared to small, circular and dim RDs. Both local viscoelastic forces and/or accessible open volume constrains can explain this finding.

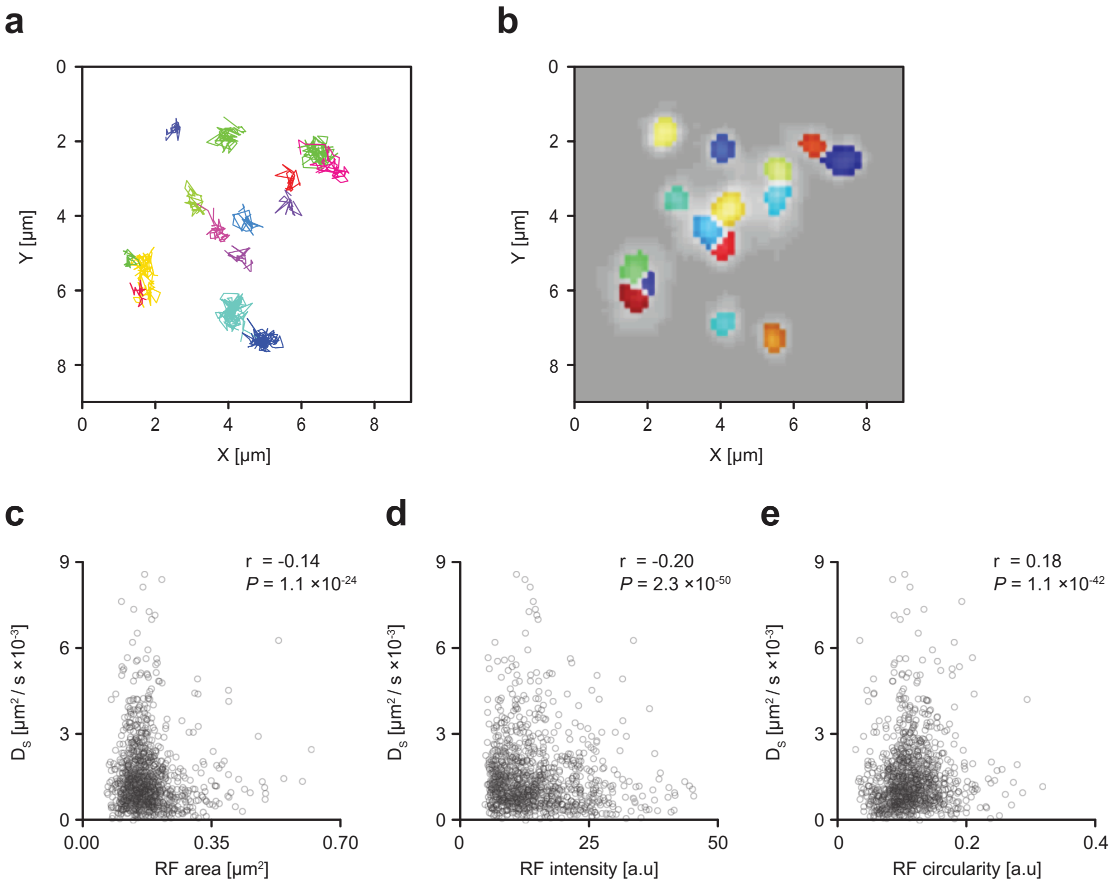

Figure 3-16: RD size, intensity and shape weakly correlate with RD dynamics.

a, The custom-written object tracker records RD position centers, and also RD size, mean intensity and RD shape at every time-step. **b**, RD outlines are segmented by an algorithm, which combines active contours and marker-controlled watershed segmentation. **c**, Big RD tend to move slightly slower than smaller RD, scatter plot using all tracked and segmented euchromatic RD (n=1,117) from 121 cells. **d**, Bright RD tend to move slightly slower than dim RD. Bright RD are presumably RD with more labeled forks. **e**, The more circular RD are, the faster they move. Circularity is calculated as $\mathrm{circ} = \frac{4*\pi*\mathrm{area}}{\mathrm{perimeter}^2}, 0 \leq \mathrm{circ} \leq 1$. In this definition, a perfect circle has circularity 1, and a line has circularity 0.

3.4.3 Effect of cell cycle stage on RD mobility

The NRK cell line used throughout this study is stably expressing PCNA-eGFP. Proliferating Cell Nuclear Agent (PCNA) is a cofactor of DNA polymerase δ and essential for DNA replication. It served us as a marker for cell cycle stage, since it allow for distinguishing between cells in early, mid and late S-phase through changing accumulation patterns. During G1 and G2-phase of the cell cycle, PCNA is evenly distributed in the cell nucleus. Examples are shown in Figure 3-17a. This allowed us to also investigate chromatin dynamics in distinct stages of interphase , see Figure 3-17b. We detected a drop in the median short-range diffusion constant $\mathrm{D_s}$ from $1.51 * 10^{-3} \frac{\mu\mathrm{m}^2}{\mathrm{s}}$ in late G1-phase to $0.99 * 10^{-3} \frac{\mu\mathrm{m}^2}{\mathrm{s}}$ in late S-phase and a recovery to $1.18 * 10^{-3} \frac{\mu\mathrm{m}^2}{\mathrm{s}}$ in G2-phase.

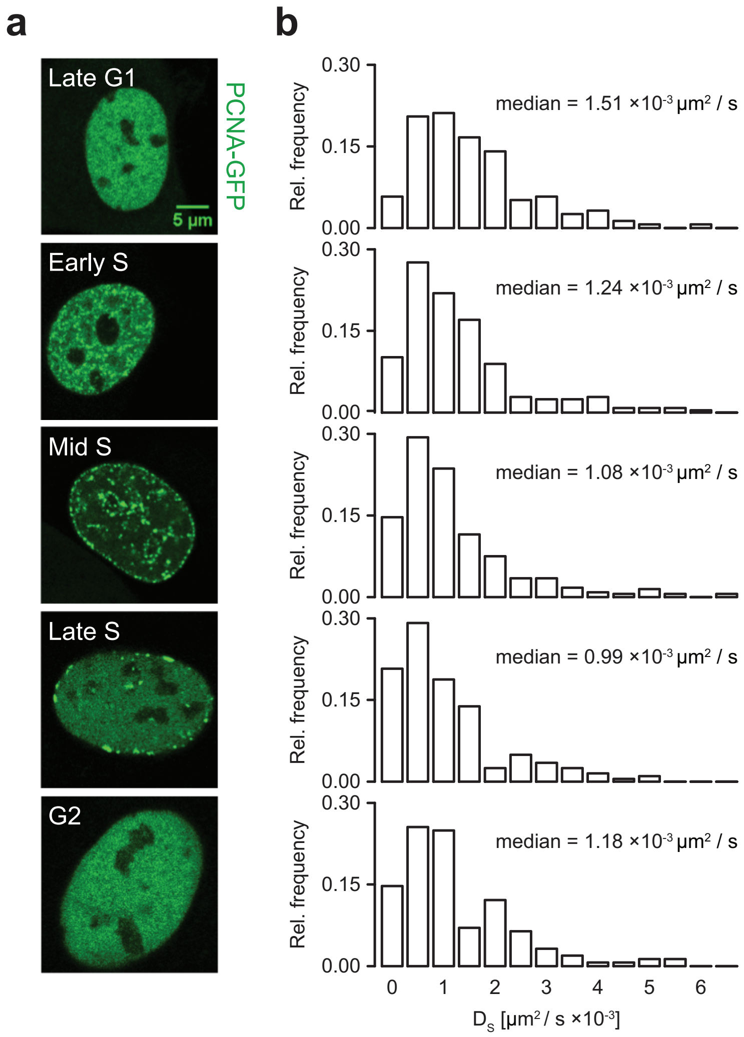

Figure 3-17: Changing dynamics of euchromatic RD throughout interphase. **a**, Confocal images of NRK cells stably expressing PCNA-eGFP during different stages of interphase from late G1 to G2-phase. **b**, Distributions of the short-range diffusion constant D_S for the individual cell cycle stages are shown. G1-phase n = 20 cells; early S-phase n = 31; mid S-phase n = 39; late S-phase n = 17; G2-phase = 14.

3.4.4 Perturbation of RD dynamics

We were asking how RD dynamics responds to global changes in accessible nuclear. We decided to perform perturbation experiments changing the ratio of chromatin mass to nuclear volume and to monitor the response of RD mobility to this change. We decided to test two conditions to increase and one condition to reduce the available free nuclear volume for euchromatin and measure their effect on the dynamics of euchromatic RDs. The results of these experiments are shown in Figure 3-18.

To increase nuclear volume, we treated cells with aphidicolin for 20 h to block DNA synthesis. As we reported before (Dultz et al., 2008), nuclei continue to grow in G1/S arrested cells and reached almost twice their normal nuclear volume although DNA content remained constant, see Figure 3-18, 4th column. The cells were given at least 2 h to recover from drug treatment before they were imaged. In cells with large nuclei, the short-range diffusion coefficient D_s was significantly increased relative to control cells, see Fig. 3—19, c.

In a second perturbation experiment, we treated cells with the histone-deacetylase inhibitor Trichostatin A (TSA) for 20 h. TSA is also known to cause cell cycle arrest preventing an increase in DNA content, while still allowing nuclei to grow. However, TSA treatment additionally decondenses the compacted heterochromatin at the nuclear periphery(Görisch et al., 2005), which could counteract the effect of increased nuclear size in terms of making additional free volume available for chromatin movement. Cells were given a 4 h recovery period after drug washout before they were imaged a time after which the compacted heterochromatic rim in had reformed, see Figure 3-18, 3rd column. The short-range diffusion coefficient D_s was significantly increased in cells with TSA enlarged nuclei (Fig. 3-19 c).

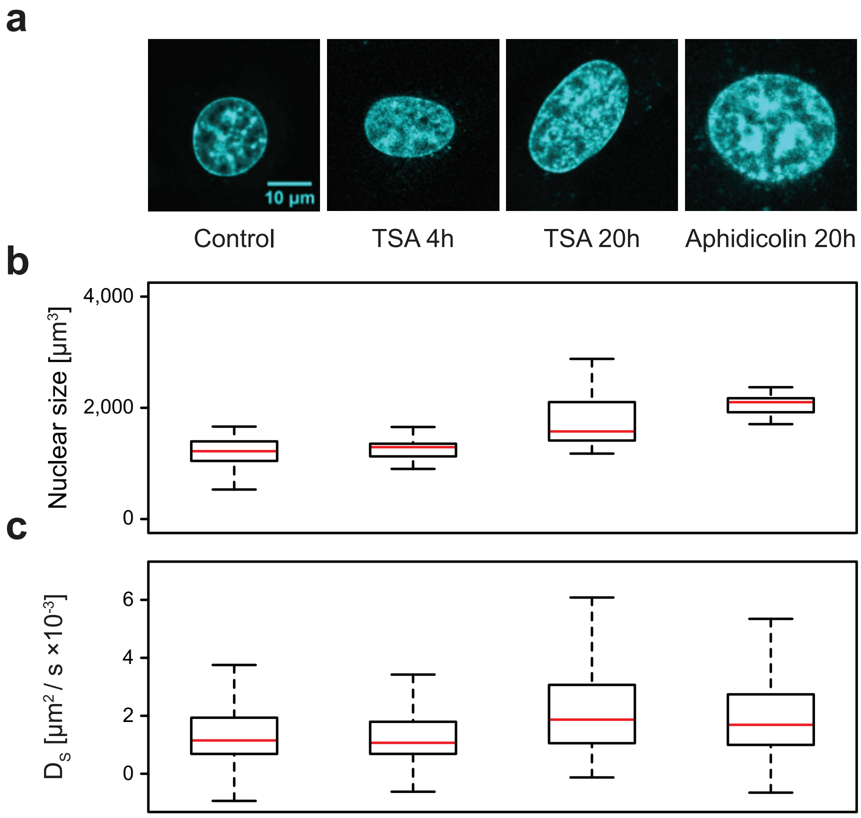

Figure 3-18: Chromatin dynamics responds to changes in topological confinement.

a, Exemplary Hoechst-stained nuclei visualizing size and ratio change of nucleoplasmic versus peripherally residing chromatin. Examples of single nuclei are given for treatment with Trichostatin A (TSA) for 4 h, for treatment with TSA for 20 h followed by a 4 h washout phase, for treatment with aphidicolin for 20 h followed by a 2 h washout phase and untreated controls. TSA treatment for 4 h results in a decompaction of peripherally residing heterochromatin, which is restored after a 4 h washout phase following 20 h TSA treatment. **b**, Quantification of the nuclear size for treatments as indicated in a. Control n = 121 cells; TSA 4 h n = 31, KS-test $P = 0.63$ relative to Control; TSA 20 h n = 29, $P < 10^{-8}$; Aphidicolin 20 h n = 29, $P < 10^{-15}$. **c**, Quantification of the short-range diffusion constant D_S for treatments as indicated in a. Control n = 1,117 trajectories; TSA 4 h n = 768, KS-test $P = 0.0002$ relative to Control; TSA 20 h n = 934, $P < 10^{-15}$; Aphidicolin 20 h n = 976, $P < 10^{-15}$.

It is known that about a third of the entire chromatin mass in a cell is stably associated with the nuclear periphery (Guelen et al., 2008). We therefore decided to reduce the available free volume for euchromatin movement by detaching this chromatin fraction from the periphery with an acute treatment with TSA for 4 h without drug washout before imaging. In this condition, peripherally residing heterochromatin was dramatically decompacted, while nuclear size was unchanged. Hoechst staining of treated nuclei showed that the formerly strong signal of the compacted nuclear periphery vanishes over the course of 4 h, see Figure 3-18a, 2nd column. By relocating more more chromatin into the nucleoplasm, this should reduce the available free volume for euchromatic RDs. However we did not find a significant reduction of the short term diffusion coefficient Ds, suggesting that increasing nucleoplasmic chromatin content by 1/3 is not sufficient to impose a strong confinement on the movement of euchromatic RDs.

In summary, our investigations have confirmed that global RD dynamics are characterized by slow sub-diffusive motion. Almost all heterochromatic domains seem to be in close contact with either the nuclear membrane or nucleoli and my analysis shows that heterochromatic RDs are basically immobilized on these nuclear scaffold structures. Euchromatic domains, which are located all across the nucleoplasm on the other hand, show significantly higher mobility, which varies significantly between individual RDs (median $D_S = 0.0065\,\frac{\mu m^2}{s}$). We could show that one explanation for the spread in D_S is the variability of RD size, since bigger RDs tend to move slower compared to smaller RDs. We could also demonstrate that euchromatic RD dynamics across the nucleoplasmic space is independent of proximity to the nuclear membrane or nucleoli. We further found that chromatin dynamics slows down progressively from late G1 stage during S-phase and that RD dynamics can be increased by making additional nuclear volume available by blocking DNA replication while allowing continued nuclear growth.

3.5 Quantifying elastic coupling between RDs

In the previous chapters, I have presented our results on measuring RD size, spacing and their global dynamics across the nucleus. In the next chapter, I am presenting my results on quantifying the coupling of movement between closely spaced RD. To understand how stiff the chromatin fiber is an to what extend being part of the same chromosomal DNA molecule constrains the movement of individual RDs. We were interested to identify the typical distance between RDs up to which their movement is elastically coupled.

We used time-lapse recordings of RDs to quantify the loss of motion-correlation between RDs spaced at increasing distances from one another. The idea is that a pair of RDs, which are elastically coupled, move coherently. The trajectories of the respective domains should be close to parallel, since both RD move into similar directions at each time-step. We expected that the degree of coherence in motion is lost over longer distances, as a consequence of weakening elastic coupling The typical distance at which coupling is lost is thus a measure of stiffness of the chromatin polymer.

For quantification, I calculated the correlation angles α between displacement vectors of trajectories in every time-step. The concept is shown in Figure 3-19a. Looking at a pair of domains, if the displacement vectors of the two trajectories are parallel in each time-step, the angle α is constantly zero and movement fully correlated. This scenario is shown in the left panel of Figure 3-19a. On the other hand, if looking at a pair of trajectories of freely diffusing particles without motion correlation, the correlation angle α measured in every time-step are evenly distributed from 0 to 180° and the trajectory average <α> is 90°. When plotting the mean correlation angle per trajectory pair versus their 2D spatial distance, it is possible to monitor the loss of correlation with increasing pair distance, indicated by the average correlation angle going up toward 90°.

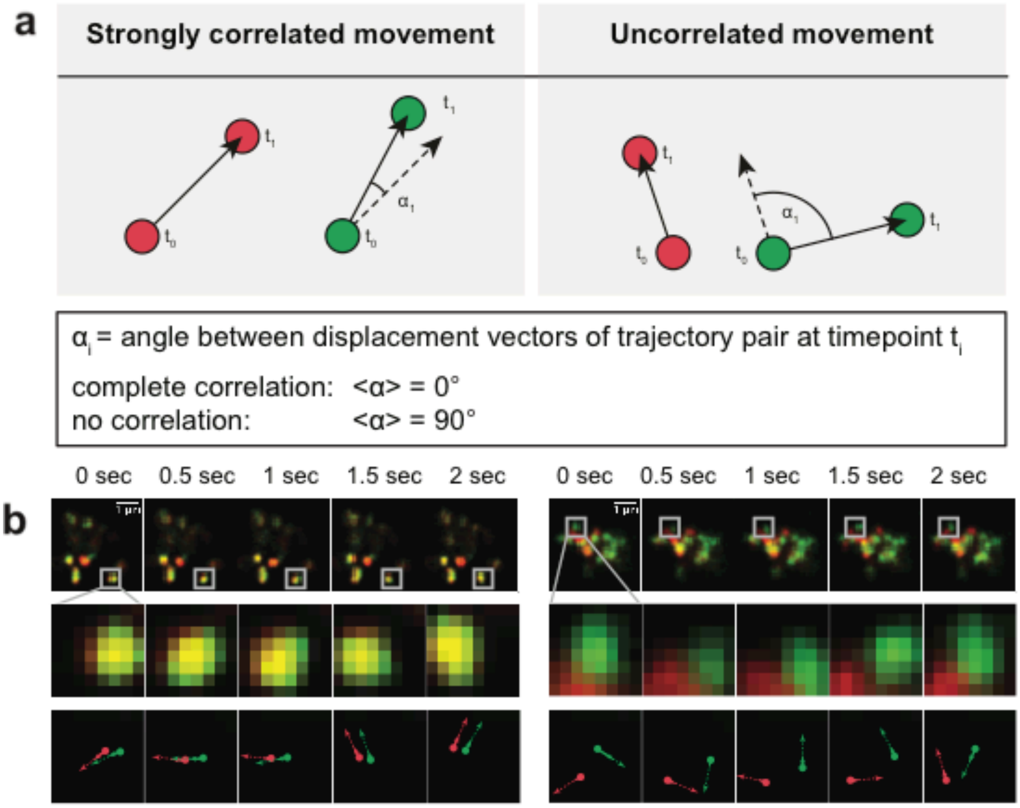

Figure 3-19: Quantifying coherence of movement between RD pairs labeled in different colors, using correlation angle α_i.

a, Schematics explaining the concept of calculating correlation angles between trajectory pairs. The left panel shows an example of strongly correlated/coherent movement and the right panel shows an example of uncorrelated/incoherent movement between a pair of tracked domains. **b**, On the left is an exemplary sequence of a lime-lapse movie showing double-color labeled CT with waiting time 30 minutes between pulses. On the right is an exampled with waiting time 90 minutes. The lower panels show the zoom-in into a respective pair. On the left example ($\Delta t = 30$ min), the displacement vectors of the red and the green focus are almost parallel in every time-step, resulting in small average correlation angles. On the right example ($\Delta t = 90$ min), the displacement vectors of the red and the green focus are not correlated, resulting in random angles, which average out to 90°. Scale bars are 2 µm.

By analyzing the trajectories from 121 CTs of the single-color reference dataset, I did not find a correlation for distances above 500 nm and faint correlation for distances smaller than 500 nm. The calculations were done for time intervals of 0.5 s, 5 s and 10 s (results are shown in the Discussion). However, pairs with spacing below 500 nm in 2D are not easily tracked in a single-color: Firstly, RD labeled by a single pulse of fluorescent nucleotides are typically spaced more than 500 nm from another, so only few pairs spaced below this distances found. Secondly, there is also the technical problem of tracking objects spaced so closely with confocal resolution.

The solution to this problem was to label nearby RD in different colors. The method was introduced in chapter 3.2 already. In brief, synchronized cells were exposed to two pulses of differently colored nucleotides after aphidicolin release. They were exposed to a first pulse of ATTO 633-dUTP and, after a waiting time, to a second pulse using ATTO 565-dUTP. In this way, I could track pairs of RD labeled in different colors, which were spaced at distances below confocal resolution from one other and even pairs with overlapping signal. Only euchromatic RD were used for this analysis, since most heterochromatic RD are immobilized. In total, I recorded a dataset using 7 different waiting times between nucleotide pulses from 15 minutes and to 120 minutes. Examples for waiting times of 30 min and 90 min are given in Figure 3-19b. A control, where both nucleotides were applied simultaneously, was used to assess the noise in my measurement (see Discussion).

I recorded a series of 2D confocal time-lapse movies of double-color labeled CT on a Zeiss LSM 780 ConfoCor and simultaneously scanned with both a 633 nm and a 565 nm-laser to excite sets of RD labeled with ATTO 633 and ATTO 565 respectively. Both channels were detected using APD detectors, which have superior sensitivity for dyes emitting over 600 nm compared to GaAsP-PMTs. As in all live cell imaging experiments presented in this thesis, oxygen in the imaging medium was reduced to approximately 5%. For the analysis I picked pairs of trajectories that were both tracked over at least 30 frames (15 s), and then calculated the mean correlation angle as described before.

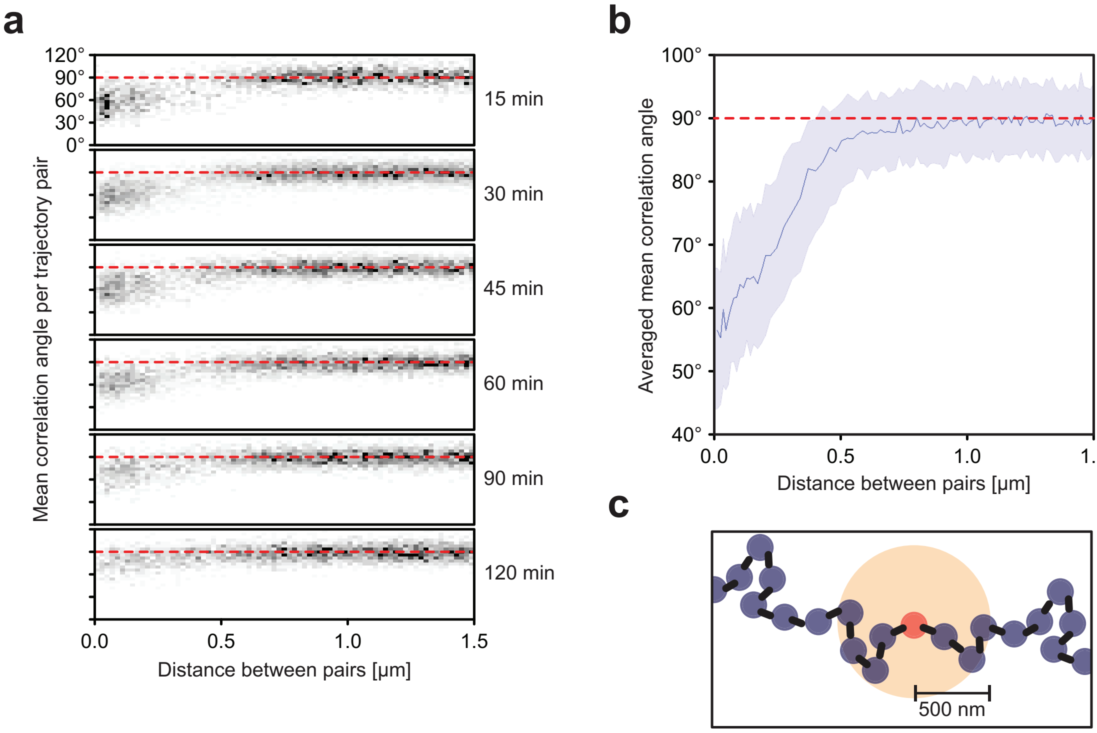

Figure 3-20: Coherent movement between pairs of labeled RD is lost with increasing distance between pairs, elastic coupling range ~500 nm.
a, Averaged correlation angles for every trajectory pair <α> is scattered versus the spatial distance between the pairs in a density plot. Analysis shown for six different waiting times between labeling pulses: 15 min (n = 3,144 pairs, 26 cells), 30 min (n = 8,256 pairs, 27 cells), 45 min (n = 5,126 pairs, 21 cells), 60 min (n = 5,306 pairs, 15 cells), 90 min (n = 4,103 pairs, 22 cells), 120 min (n = 4,329 pairs, 22 cells). **b**, Bundled data from all six datasets (n = 30,264 pairs, 133 cells). Mean is displayed in dark blue, standard deviations in light blue. **c**, Schematics of elastic coupling range ~500 nm.

Using the six different waiting times of double labeled neighboring RDs, I was able to sample pair distances below 500 nm and to calculate the mean correlation angle between trajectory pairs. While the shorter waiting time datasets constitute mostly shorter pair distances, the longer waiting time datasets constitute increasing pair distances as well. In the 15 min dataset, most pairs are not yet separated and I measure many distances around and below 100 nm, see Figure 3-20a. With increasing waiting times up to 120 minutes, it was possible to sample the entire range of pair distances below 500 nm, which were not covered well in the single-color dataset.

The data clearly shows that correlation is lost with increasing pair distance. Figure 3-20b shows the combined data from all six waiting times. It is evident that the mean correlation angle $\langle\alpha\rangle$ approaches 90°, indicating near complete loss of correlation, starting at a distance of approximately 500 nm (schematic provided in Figure 3-20c). In summary, our quantitation on loss of coherence in dynamics between RD spaced at increasing distances has a revealed a short elastic coupling range below 500 nm.

4 Discussion

The study presented in this thesis focuses on two main aspects: The structural and the dynamic organization of replication domains (RD). We have investigated RD size and internal organization using super-resolution microscopy in native and energy-depleted condition. Additionally, I have quantified chromatin dynamics in live cells across the nucleus, throughout the cell cycle and in response to perturbations. I will review both parts of the work in the following chapter and suggest a direction for future research on this topic.

4.1 Investigating chromatin structure using stochastic super-resolution microscopy

In this work, the key to studying RD internal organization was the increased resolution provided by ground state depletion followed by individual molecule return (GSDIM) microscopy. However, this resolution can only be reached if the labeling provides high localization density, which for instance is a problem in studies using fluorescently labeled histones (Bohn 2010). We have used *in vivo* scrape replication labeling, which allows high-density fluorophore labeling with low background. Our approach sets apart from previous studies using stochastic super-resolution microscopy to study global chromatin structure by investigating single basic structural subunits of chromatin, instead of attempting to visualize the entire fiber. The high compaction of the chromatin polymer is a problem when using unspecific DNA labeling approaches, such as DNA-intercalating dyes (Flors 2009). We could reduce problematic signal abundance in the dense chromatin polymer by culturing cells for at least 3 days after labeling, to a stage where individual labeled chromosome territories (CT) could be identified. This problem is also avoided when using stochastic super-resolution microscopy in combination with fluorescence *in situ* hybridization (FISH) to visualize specific genomic regions of interest (Weiland *et al.*, 2011). Major concerns regarding FISH protocols are disruption of nuclear structure by the denaturation step. (Solovei *et al.*, 2002b). *In vivo* scrape labeling, our method of choice, is compatible with good conservation of nuclear structure. It does not require a permeabilization step after cell fixation to introduce the fluorophore, since living cells are labeled prior to fixation.

The exact genomic length of the DNA segment that is labeled by scrape labeling is currently unknown. The time-window in which I scrape attached cells from their surface in the presence of a high concentration of ATTO 633-dUTP was typically about 60 seconds. We thus assume that the labeling interval is reasonably short, yielding labeled segments of only a few kilobasepairs. However, this estimate is yet to be confirmed experimentally, e.g. by molecular DNA combing, a technique that produces uniformly stretched DNA strands *in vitro*. To this date, there is no molecular DNA combing data on scrape pulse labeled cells published.

4.1.1 Replication fork clusters

We find that RD in our NRK cell line are encompassing a smaller number of resolvable domains, that we assume to represent replicons than what has been reported in previous studies. While I find a median number of 4 forks per RD, Jackson and Pombo have reported a typical number of 6 bidirectional replicons per RD, which results in 12 forks per RD (Jackson and Pombo, 1998).Other authors have suggested even higher numbers (as high as 20 replicons or 40 forks) per RD (Cook, 1999). While there are cell-line dependent differences, the high number of replicons per RD reported might be biased due to various technical limitations This issue was addressed in detail in a review by Berezney *et al.*, 2000 (Berezney et al., 2000).

DNA combing is a very useful technique to measure fork progression speed and directionality of replication. However, it is technically difficult to stretch out single DNA molecules for more than 500 kb. Thus, single labeled forks are easily found, whereas groups of forks belonging to the same RD are more difficult to detect, making this method vulnerable to bias when quantifying the number of forks per RD (Técher et al., 2013). We demonstrate that GSDIM imaging is well-suited to assess the number of spatially resolvable active forks within a RD. However, it needs to be noted that imaging labeled forks *in situ* cannot reach the resolution of DNA combing, which allows for distinguishing labeled DNA sections that are only few kilobasepairs apart. Since the typical median number of replicon spacing is reported to be approximately 130 kb, it seems likely that most active forks in a RD are spaced far enough from one another to be resolved by GSDIM imaging, but until correlative GSDIM imaging and DNA combing of replication forks has been performed this is assumption is plausible but not yet formally validated.

We did a simple calculation to assess if a median number of 4 forks per RD is compatible with what is currently known about the process of replication. RDs typically finish replication within approximately 60 min (Ma et al., 1998) (Jackson and Pombo, 1998). The replication speed of a single fork is in the order of 2 kb/min (Palumbo et al., 2013). Assuming 4 forks replicating DNA for 60 min, this would result in 480 kb of replicated DNA. This number matches the genomic length covered by one RD, which is approximately 500 kb according to the most recent systematic replication timing study on over 30 different cell lines (Pope et al., 2014). Formerly it was thought that RD are spanning bigger genomic regions, partially explaining the overestimation of typical numbers of forks per RD (Cook, 1999).

4.1.2 Replication domain size

The median diameter of a RD we measure is 150 nm. Since I do not label the entire

RD by scrape labeling, but only the co-replicating origins at the moment of pulse labeling, there is a chance that the diameter and area measurements are an underestimate of the actual RD size.

This RD size is significantly smaller than measurements by confocal microscopy (350 to 500 nm (Albiez et al., 2006; Maya-Mendoza et al., 2010)), and consistent with studies reporting sizes from 40 to 210 nm (median size of 125 nm), as measured using both spatially modulated illumination (SMI) and 3D structured illumination microscopy (3D-SIM) (Baddeley et al., 2010). In another study using stimulated emission depletion microscopy (STED), a typical size of 170 nm was reported (Cseresnyes et al., 2009).

Even though the median values are comparable, I have measured a broader and strongly skewed distribution of RD diameters. We find mostly small clusters and a tail of bigger clusters up to a maximum size of approximately 400 nm. This distribution resembles that of genomic sizes measured for replication domains using next-generation sequencing-based replication time profiling. Authors find that most of the domains are in the range of 400 to 800 kb, with a tail in the distribution going up to several Mb (Pope et al., 2014).

The combination of quantitative knowledge about genomic size with the physical dimension my data provides is an ideal starting point for building more realistic polymer models describing the folding of chromatin within a RD.

4.1.3 Solitary replication forks

Besides the groups of spatially clustered replication forks, we also find solitary, unclustered forks in our GSDIM images. *In vivo* scrape replication labeling is virtually free of background (Zink, 2006) (Schermelleh et al., 2001). We can therefore assume that the single peaks in the GSDIM images are not background noise, but truly reflect solitary replication forks. Using the corresponding confocal z-stacks of the entire CT, I could also exclude that the solitary forks found are part of RD, which were not fully in focus of the GSDIM. My analysis revealed that most replication forks cluster into small groups (87.4%). The remaining 12.6% of forks are solitary that are distally spaced from other forks and cannot be assigned to a RD. I find almost equal numbers of RD compared to solitary forks. Our findings are consistent with a previous publication, in which authors have looked at autoradiographs of sheered DNA labeled by radioactive nucleotides (Yurov and Liapunova, 1977). The authors reported that half of the replicons are unclustered. This number is identical to what we have counted. Our data is also in line with a more recent systematic study comparing data of molecular DNA combing in various cell lines (Palumbo et al., 2013). The authors find up to 5-50% of replication forks to be unidirectional. The authors do not make a statement about whether these unidirectional forks are grouped or not.

There is an ongoing debate in the literature about the prevalence of large unidirectional forks. A large unidirectional replicon (450 kb) has been well characterized in the IgH locus (Zhou et al., 2002) (Norio et al., 2005). Additionally, genome-wide profiling of replication timing has suggested that there are long origin-free regions of the genome, preferentially in transition regions of replication timing. It was proposed that these transition regions are replicated by single unidirectional forks (Hiratani et al., 2008). However, a study analyzing different replication time zones in several human cells lines using DNA combing is contradicting this view (Guilbaud et al., 2011).

Our data does not reveal any information about the underlying genomic replicon size of the solitary replication forks we find. But it is consistent with the idea that, while most DNA is replicated synchronously by small groups of replicons, a fraction of the genome is replicated by solitary, unidirectional forks. It has been speculated that single forks could have been missed by confocal microscopy imaging of RD, since they give less signal compared to groups of labeled forks (Berezney et al., 2000). Our correlated confocal and GSDIM imaging confirm that most solitary forks we find on GSDIM images are indeed not visible in the confocal image illustrating that GSDIM is a suitable method for future studies on this issue.

4.2 Measuring nearest neighbor distance between RDs

Additionally, I have measured the typical nearest neighbor distance between RD using confocal microscopy and double-color labeling. In these experiments, cells are exposed to a second dye-conjugated nucleotide precursor after a waiting time (pulse-chase-pulse), likely resulting in labeling of neighboring RD. My results indicate that the typical RD (center to center) spacing of 270 nm is significantly bigger than the typical RD size of 150 nm, as measured in our GSDIM experiments. I therefore propose that there are DNA linker regions spanning approximately 120 nm between genomic regions organized into RDs. It is known that most DNA from early replicating chromatin is organized into RD spaced by narrow transition regions. We hypothesize that these transition regions are spatially much less compacted than chromatin within RD and therefore mediate the additional spacing in the order of 120 nm. I need to point out that the assumption of 60 minutes replication timing is based on published literature (Jackson and Pombo, 1998; Ma et al., 1998; Maya-Mendoza et al., 2010). We have yet to perform molecular DNA combing experiments to verify that this timing also applies to our NRK cell line.

In the study using confocal microscopy by of Maya-Mendoza *et al.* from 2010, the authors have estimated both the median RD diameter and the nearest neighbor distance to be 350 nm and have concluded that neighboring RDs are touching. We assume that this size measurement is overestimated because of confocal resolution.

For distance measurements between neighboring RDs, we have performed a control measurement to assess the technical noise. In the control, RDs were simultaneously labeled with both fluorophores. A measurement imprecision is clearly detectable , see Figure 4-1a, left panel. It occasionally occurs that RDs are only detected in the brighter channel leading to an erroneous assignment of this RD during nearest neighbor pairing. Different intensity levels between the two channels can therefore explain the tail in the distribution.

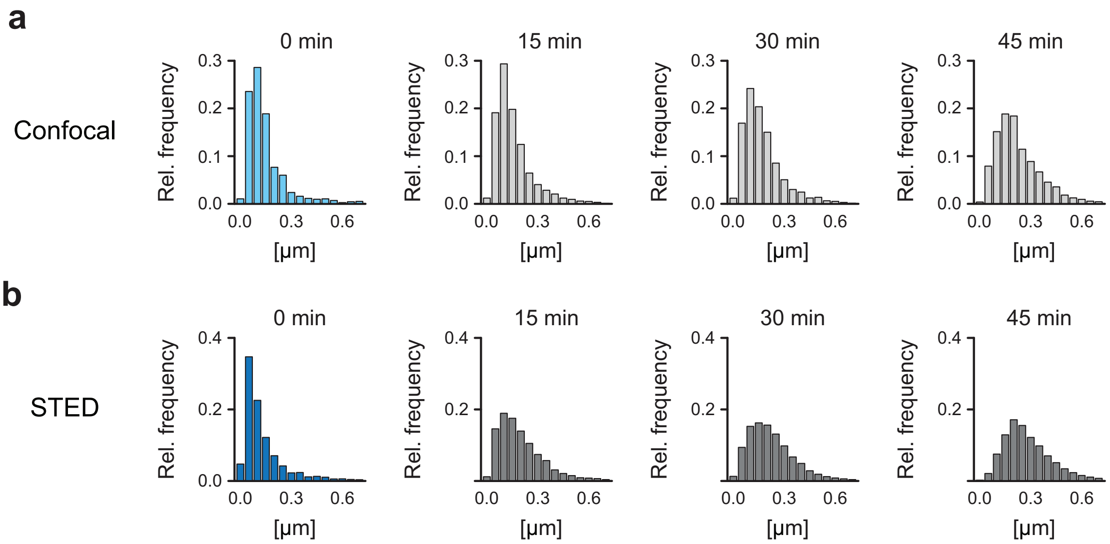

Figure 4-1: Nearest neighbor distance measurement between RD.
a, Results of confocal microscopy. 0 min indicates the control in which cells were simultaneously exposed both fluorophores. **b**, Results of STED microscopy with waiting times as in a.

We further validated that the resolution of the confocal microscope allows reliable distance measurement between RD. This was to ensure that the nearest neighbor distance measurements were not overestimated, since our hypothesis of extended linkers is based on this number. We could confirm the results by performing a small series of double-color STED imaging experiments on a Leica SP8 STED 3X. On average, the median STED measurements were approximately 30% bigger than the confocal result, see Figure 4-1a,b. The technical noise, again assessed by simultaneous labeling with both fluorophores, was a bit lower compared to the confocal measurements, even though the problem of the unpaired domains persisted, see Figure 4-1b, left panel. I speculate that the measured nearest neighbor distances using STED microscopy were bigger compared to the confocal measurements because of the higher intensities reached by the depletion beam. Using in-vivo scrape labeling, the labeling strength varies between both channels. The high laser intensities have likely photobleached the signal of the weaker labeled channel at times, and therefore measure increased median distances because of imperfect pairing. Detailed STED microscopy protocols are included in the Methods chapter.

It is interesting to review the idea of extended linker regions between RDs in the light of new evidence showing that RDs closely resemble the more recently discovered topologically associated domains (TADs) (Pope et al., 2014). I have addressed this reported correspondence of RD to TADs in the Introduction chapter of this thesis. Assuming TADs are the population-averaged reflection of RDs, it is interesting to highlight some findings about boundary regions between TADs. Between neighboring TADs, which are regions of enhanced cis-interactions (typically several hundred kilobasepairs in size), smaller genomic regions were found (76.3% of them being <50 kb), separating TADs from one another (Dixon et al., 2012). If the genomic TAD boundary size corresponds to the genomic size of the proposed linkers, they would be about 10 times less compacted than chromatin within RD. This lowered level of compaction could be associated with their specific protein occupancy. For instance, they are described to be enriched for the insulator binding protein CTCF (Dixon et al., 2012).

There is additional evidence from the literature supporting the idea that boundary regions between TADs mediate spatial insulation. In a fluorescent *in situ* hybridization (FISH) experiment, spatial distances between two pairs of genomic loci have been studied in fixed cells. One pair of genomic loci within the same TAD was compared to a pair of loci between TADs. The authors could demonstrate that, even though the two pairs have the same genomic spacing, the spatial distance between loci on the same TAD was significantly smaller than the distances of loci between TADs

(Nora et al., 2012). This result, just as our findings, cannot be explained by spatially touching RD/TADs, and supports the existence of extended linker regions.

Another aspect that raised our interest were reports of distance measurements between presumably second nearest neighbors, by using even bigger chase times of 120 minutes for double-color labeling. The authors have reported a median distance of 350 nm between nearest neighbors and a median distance of 500 nm between second nearest neighbors (Maya-Mendoza et al., 2010). We were asking if this finding could indicate that chromatin at the scale of RDs might have a short persistence length of only few hundred nanometers, see the cartoon in Figure 4-2.

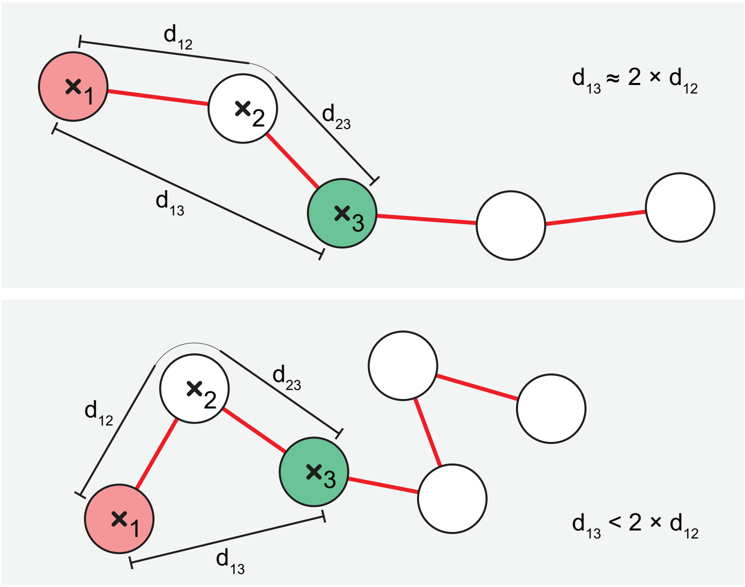

Figure 4-2: Cartoon depicting polymers with varying persistence length. In the top panel, a stiff polymer with a long persistence length is shown. The distance between second nearest neighbors is approximately twice the distance of nearest neighbors. In the bottom panel, a soft polymer with a short persistence length is shown. The distance between second nearest neighbors is much smaller than twice the distance between nearest neighbors.

A short persistence length characterizes a soft polymer. It indicates that orientation correlation along the polymer is lost at short distances along the polymer contour. The experiments measuring the second neighbor distance were performed using antibody-staining of permeabilized cells which had been exposed to extended pulses of tagged nucleotides (Ma et al., 1998), (Maya-Mendoza et al., 2010). We could verify this result in *in vivo* scrape labeled cells, where the nuclear structure is better conserved. Even though we measured significantly smaller median distances, the qualitative result was confirmed. Our data is shown in Figure 4-3. The median second neighbor distance we measure is 320 nm, thus much closer to the nearest neighbor distances of 270 nm than twice the nearest neighbor distance (which would be 540 nm). We conclude that the persistence length of chromatin at the scale of RDs must be rather short, probably in the range of the nearest neighbor spacing. To get to a more quantitative number, it would be useful to trace a bigger section along the contour.

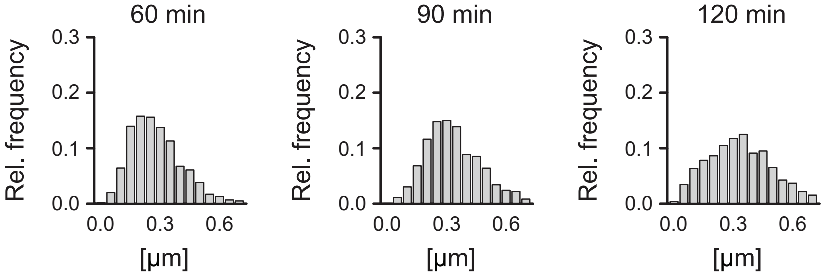

Figure 4-3: Nearest neighbor distance measurement between RD at longer waiting times 60 min, 90 min and 120 min.
Median second nearest neighbor distance (measured at waiting time 120 min) is significantly smaller than twice the median nearest neighbor distance (320 nm and 2×270 nm, respectively), indicating that chromatin is a soft polymer with a short persistence length.

4.3 ATP depletion-induced chromatin compaction

We have used ATP depletion as a simple experimental means to acutely induce chromatin compaction. We could confirm literature reports that chromatin volume reduces by approximately 40% upon ATP depletion (Martin et al., 2007). I could also exclude that part of this compaction is indirectly caused by phototoxicity of imaging, see Appendix Figure 5-2. By measuring nearest neighbor fork distance within RD and RD size in ATP-depleted cells compared to control samples, we could additionally demonstrate that despite the chromatin volume reduction upon ATP depletion there is little compaction of DNA within RDs.

Since the drastic volume change cannot be fully attributed to compaction of DNA within RD, I assume that the major contribution of volume loss must be mediated by the spatially extended linker regions between RDs, which may respond more strongly to ATP-depletion. However, since I do not have direct evidence of non-uniform volume reduction from live cell imaging experiments performed before and after ATP depletion, I can only indirectly infer that this non-uniform volume reduction is mediated by linker contraction. We cannot exclude the possibility that later replicating RDs, not labeled by our nucleotide pulse, compact more strongly upon ATP depletion than the RD we are observing.

Upon ATP depletion, I could observe a strong decrease in RD mobility. This observation can also be explained by a contraction of linkers, by which several formerly spaced apart RDs would be brought together and diffuse as one unit. Both the increased size of RD, but also the changed physical properties of contracted linkers (increased rigidity) could potentially explain this loss in dynamics.

Cell nuclei can undergo compaction changes during natural transitions such as cell differentiation (Talwar et al., 2013) or gene activation. I speculate that cells could use local chromatin condensation/decondensation via linker contraction/expansion for gene repositioning. It was recently shown that both transcriptional activation, but also mere chromatin decondensation, induced by the recruitment of an acidic peptide (not altering the transcription state), can reposition genes (Bickmore and van Steensel, 2013).

4.4 Dynamics

A major part of my PhD work was dedicated to the analysis of chromatin dynamics in life cells, as presented in chapter 3.4. Previous studies addressing the topic have consistently reported general sub-diffusive movement of chromatin (Levi et al., 2005) (Bronstein et al., 2009) (Bornfleth et al., 1999). Other studies have additionally found ATP-dependent switching to directional movement for hours over micrometers (Chuang et al., 2006), or sporadic switching to directional movement for seconds (Levi et al., 2005). A direct comparison of results is difficult, since different time domains were covered, by recording with sub-second sampling over minutes to sampling every 10 minutes over hours. The data were also tracked with varying precision, since both single tagged loci and larger structures, such as entire territories were tracked. While the reported diffusion coefficients agree in their magnitude, previous studies could not provide explanations for the wide distribution in diffusion coefficients found.

We wanted to advance the field by systematically assessing which parameters influence chromatin dynamics. The parameters we investigated can be grouped into four categories. At first, we were asking if the proximity of euchromatic RDs to peripheral or nucleolar compartment affects their dynamic behavior. Secondly, we asked if proximity to the CT surface has an influence. This was particularly interesting since the CT surface has been associated with elevated transcriptional activity (Mahy et al., 2002) and since chromatin poor space between territories has been postulated. The third question was whether RD size and shape influence their dynamics. And finally we were asking if RD dynamics change with cell cycle progression and especially progressing replication.

4.4.1 RD dynamics change with cell cycle stage

I have observed a drop in the short-range diffusion coefficient D_s of euchromatic RDs with cell cycle progression from late G1 over early S-phase to mid S-phase, with the lowest D_s found for late S-phase. The diffusion coefficient then relaxed again in G2-phase to similar values as in G1. A study looking into the same question published in 2013 could not observe this change of RD dynamic with cell cycle progression in mammalian cells (Pliss et al., 2013). Surprisingly the authors were also not able to pick up a change in dynamics upon ATP depletion, which has been consistently reported in the literature 3(Zidovska et al., 2013) I thus suggest that we were able to detect the significant change because of higher tracking precision and longer trajectories (up to 20-fold longer trajectories compared to (Pliss et al., 2013)).

A comparable finding has been reported from chromosome loci in *Saccharomyces cerevisiae,* tagged by GFP-fused to the *lac* repressor (Heun et al., 2001). The authors had observed more strongly constrained movement of single loci in S-phase compared to G1-phase. They could restore the higher mobility of chromatin loci in S-phase yeast nuclei by inhibiting DNA replication. They also had shown that a mutant yeast strain with *orc2-1* deficiency, which lacks the ability to efficiently activate replication origins, does not show a dynamic change between G1 and S-phase. These results lead the authors to conclude that it is the active replication process that decreases chromatin dynamics.

I can only speculate how exactly replication impairs RD dynamics. It was demonstrated, that mechanical stress builds up on the nuclear membrane during the course of S-phase, despite the activity of topoisomerase, and that this mechanical stress needs to be actively counteracted over the entire S-phase by ATR (Kumar et al., 2014) in mammalian cells. In ATR-deficient cells, which cannot detach chromatin from the membrane during replication, chromatin condenses aberrantly. I speculate that there could be a residual built-up of mechanical stress during S-phase (strongest in late S-phase) despite the activity of ATR. I hypothesize that it could be the topological replication stress, which cannot be completely neutralized by the activity of topoisomerase on chromatin and ATR on the nuclear membrane, which constrains RD mobility. This idea could explain both the continuous drop of D_s from early G1-phase to late S-phase and the recovery in G2-phase.

4.4.2 Directional movement of RDs is very rare

Spontaneous switching into directional diffusion of single chromatin loci has been reported in the literature (Levi et al., 2005). However, I could not find conclusive evidence for directional diffusion in my dataset in the timescale observed. The median trajectory length for euchromatic RD in our dataset is about half a minute. Within this time domain I could not find evidence for directional motion as a common behavior of RDs. Given the normal distribution (without a tail) of the subdiffusive exponent α ($\alpha = 0.47 \pm 0.39$, see Chapter 3.4), I conclude that overall prevalent mode of chromatin dynamics is uniformly sub-diffusive. It should be noted however that I have only observed labeled RDs, which very likely represent dense areas of chromatin organized in TADs (see above). I cannot exclude that the less compact and according to my data flexible and extended linker domains exhibit directed motion.

Furthermore, I have to point out that the high object density (RD density) in the movies are a challenge for the tracker, since RD often come so close that they seemingly ‘merge’ and cannot be unambiguously assigned. This is why most of the RD cannot be tracked over the entire movie, but only for parts of it. The median trajectory length is 57 frames for euchromatic RD. I can therefore not exclude the possibility that very mobile RD, which can sporadically switch into a directional diffusion mode, could have preferentially escaped tracking. However, I can exclude that active, directional movement of RDs is common. If RDs really exhibit active motion, the fraction of RDs showing this behavior must either be very small or the time-window in which directional movement occurs must be below the second range.

4.4.3 RDs become more dynamic by increasing nuclear volume

Furthermore, I have performed perturbation experiments to test if the available nuclear volume, or chromatin density limits chromatin dynamics. To this end, I have increased the nucleoplasmic chromatin content by a TSA-induced release of heterochromatin from the nuclear periphery into the nucleoplasmic space. Presumably, this increases chromatin density, since more DNA mass has to share the nucleoplasmic volume. I could observe a mild, yet statistically significant decrease in euchromatic RD dynamics.

In two additional experiments, I decreased the density of chromatin by blocking DNA replication during continued nuclear growth, using aphidicolin or TSA for 20 h (Tóth et al., 2004). The cells grew to about twice their normal volume. TSA-treated cells were imaged 4 h after drug-washout to give them time for recondensing their heterochromatin. Aphidicolin treated cells were imaged 2 h after drug-washout. In both these conditions, the RD dynamics increased significantly.

I concluded that RD dynamics correlate with chromatin density. One can speculate that cells have a way to regulate the global exploration range and thus the likelihood of chromatin trans-interactions by either changing the ratio between condensed peripheral heterochromatin and nucleoplasmic ‘open’ chromatin or by adjusting nuclear size. A natural transition were this ratio is commonly changed is cell differentiation.

This interpretation has to be handled with care. Both drug perturbations induce a range of additional changes to the chromatin state other than just preventing replication. Chromatin in cells treated for 4 h with TSA is hyperacetylated, which could have a direct influence on chromatin dynamics. Hyperacetylation also alters the global transcriptional profile (Gialitakis et al., 2006), adding another source of possible side-effects. Cells treated with long-term drug perturbations might also accumulate different forms of DNA damage, which has been reported to change chromatin condensation state. Therefore I cannot exclude that these effects have affected the RD dynamics, rather than the pure density of chromatin.

4.5 Coherence of RD movement

In the final part of the results section, I have presented my results on quantifying the coherence of movement between closely spaced RD as a measure of elastic coupling between RD. Quantifying elastic coupling in the nucleus is interesting, since it is poorly understood how and up to which range one chromatin fiber is capable to transduce mechanical force. We are addressing this question in order to understand observations such as the relocation of genes over several micrometers upon a change in transcriptional activity, or how ATR controls chromatin dynamics from the nuclear membrane (discussed in chapter 4.4).

The range up to which I could observe some coherent motion was approximately 500 nm (representing the elastic coupling range), which is significantly shorter than what has been previously reported using an image-correlation based approach (Zidovska et al., 2013). In this study, the authors infer positional fluctuations in chromatin from intensity fluctuations in H2B-GFP expressing nuclei. The authors identify large areas (4-5 μm in diameter) of coherent motion within nuclei for timesteps of 1-10 seconds. The areas were not identical with CTs. The observation that entire CTs might be moving in respect to each other has also been suggested before (Bornfleth et al., 1999).

Compared to our results, the areas of coherent chromatin movement identified by Zidovska *et al.* is about 5-fold larger. In my analysis presented in chapter 3.5, correlated motion was calculated for the time interval of 0.5 sec (corresponding to the sampling rate of 2 Hz at which time-lapse movies were recorded). To exclude that the difference in results is explained by the different time intervals, I have also calculated correlated motion for time intervals of 5 sec and 10 sec. As presented in Figure 4-4, I do not detect significant coherent movement of RD above a 500 nm pair distance for longer time intervals. This analysis was based on single-color movies. For this reason, pair distance below 500 nm is poorly sampled (compare to double-color experiments, Figure 3-20).

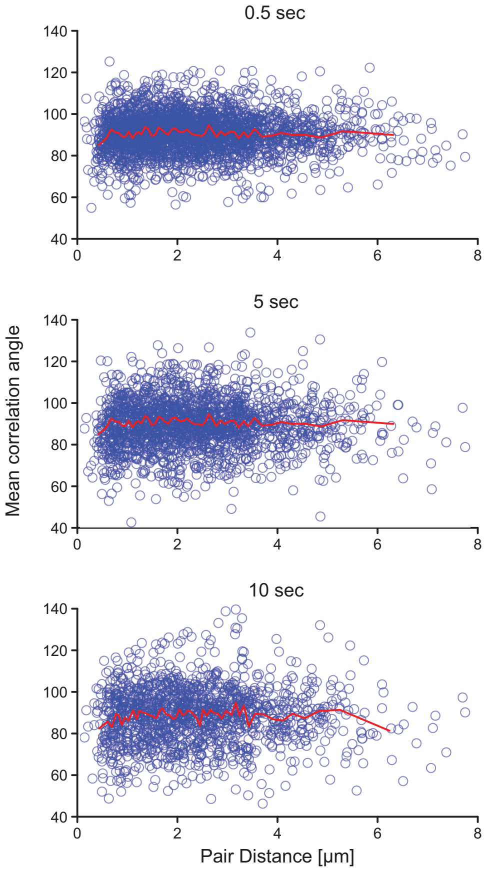

Figure 4-4: No increase in radius of motion correlation between RD for longer time intervals.
The x-axis denotes trajectory pair distances of tracked RD and the y-axis represents their respective mean correlation angle. The dataset analyzed in all 3 panels was the single-color reference dataset of euchromatin RD from 121 cells, as presented in chapter 3.4. The top panel shows the smallest time interval of 0.5 s, using n = 2,629 trajectory pairs. The middle panel shows the analysis for the time interval of 5 s using n = 1,869 trajectory pairs. The lower panel shows the analysis for the time interval of 10 s using n = 1,434 trajectory pairs.

Which forces are mediating the coupling remains an unanswered question. We cannot directly tell if coupling is mediated only over the contour of the fiber between genomic neighboring RD, or if it can also be mediated between different sections of the fiber or even in trans between two fibers, which are spatially close but genomically distal. Zidovska et al. have suggested the latter scenario.

We cannot exclude cell-type specific differences as a possible explanation for the contrasting results. A more plausible reason for the difference between my results and the study described by Zidovska *et al.* could be the sensitivity in detecting correlated motion. We use trajectories of single RDs, while they use bulk chromatin signal to quantify the coherence of chromatin movement. Doing both measurements simultaneously in the same cell would allow for a direct comparison. One could use a cell expressing fluorescent histones, label RD by *in vivo* scrape labeling and perform both analyses to directly compare results.

4.6 A simple comprehensive model for chromosome organization in interphase nuclei

Our findings on structural and dynamic organization of RD converge into a comprehensive model of higher order chromatin organization. Our main findings are highlighted in the cartoon depicted in Figure 4-5.

The main findings are the following:

- There is a large variability in RD size. The median size is 150 nm and ranges up to approximately 400 nm. The median number of replication forks labeled per RD is 4.
- Typical nearest neighbor spacing (center to center) between RD is significantly bigger than typical RD size. The median spacing is 270 nm and ranges up to approximately 600 nm. We hypothesize the existence of extended linker regions between RD, whose median length would be 120 nm. The chromatin persistence length on the scale of RD is comparably short, less than 500 nm, or two RDs.
- Bulk chromatin can undergo 40% compaction without significant compaction of chromatin within RDs, presumably because of linker contraction.
- Heterochromatic RDs are mostly immobilized at the nuclear periphery or on nucleoli. Euchromatic RDs are dynamic across the nucleus, even in close proximity to either nuclear periphery or nucleoli. They consistently show sub-diffusive behavior. Bigger RDs show slightly slower movement than smaller domains.
- The elastic coupling range between RD is approximately 500 nm

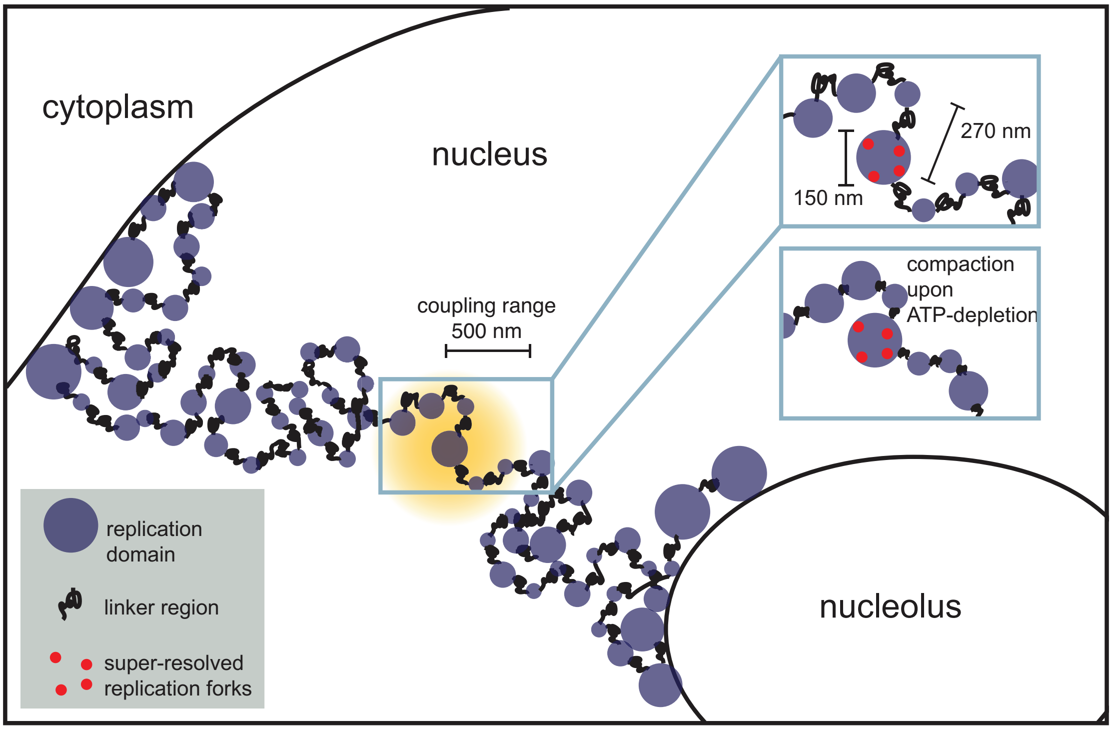

Figure 4-5: Illustration of the summarizing model.

4.7 Outlook

In this thesis, I could demonstrate that super-resolution imaging of RD can be used to visualize substructure, most likely individual replication forks, within RD. This assay can be used to quantitatively assess chromatin compaction state at the level of RDs. I suggest that this method can be a useful tool to study how native biological transition processes, such as mitosis, cell differentiation or X-chromosome inactivation shape chromatin compaction at the level its basic structural subunits. It is a complementary approach to currently available methods to measure chromatin compaction, such as FISH or fiber sedimentation studies and HiC. The measurements of RD size, RD nearest neighbor distances and RD coupling radius will help to make more realistic constrains for computational polymer models of chromatin.

I further suggest that our approach to study the loss of elastic coupling between RDs spaced at increasing distances within the nucleus is a useful addition to the available toolset for quantifying global chromatin dynamics. It is yet to be determined how variable or conserved the elastic coupling radius is between different cell lines and how the coupling is established and regulated.

In the recent past, there has been a wealth of genomic sequencing studies describing epigenetic modifications and occupancy of DNA-interacting proteins along the linear DNA sequence. These methods provide increasingly precise linear maps of functional genomic elements in healthy and diseased tissue types and at different developmental stages. More recently, this information was extended by datasets from chromosome conformation capture-based methods, which provide probabilistic and population averaged insight into chromatin topology.

A major future challenge will be the assembly of these rich datasets into a three-dimensional picture of the physical distances of dynamic chromatin associations. Technical biases introduced by population averaging, fragmentation and sequencing need to be carefully considered when interpreting this data and building chromatin models based on translating interaction frequencies into physical distances in a dynamic context. Single cell imaging will therefore be essential to complement the efforts by evaluating model predictions and refining model constraints. The combined analysis and interpretation of data generated using sequencing and imaging-based methods will set the framework for understanding genome regulation at a mechanistic level. A combination of super-resolution microscopy and FISH has the potential to investigate large chromatin loops, which have been hypothesized. I would be also extremely interesting to investigate the internal TAD regions compared to TAD boundaries using super-resolution FISH.

Technical advances in both fields will soon boost the amount of available information about dynamic associations of chromatin, which is currently still the most elusive aspect of chromatin organization. Methods such as Hi-C and DamID are already starting to be applicable at the single cell level. In the field of light microscopy, various technical advances are also on the way. They include the development of new chemical tags and engineered protein systems (e.g. CRISPR/Cas9-System) for specific labeling of nuclear structures and the development of new synthetic dyes with optimized photo-physical properties for super-resolution imaging. There are also strong efforts to make 3D super-resolution microscopy and live-cell super-resolution microscopy routinely applicable to biological samples. The combined efforts of sequencing-based methods and imaging will pave the way to an exiting future in the field studying chromatin organization and dynamics.

5 Appendix

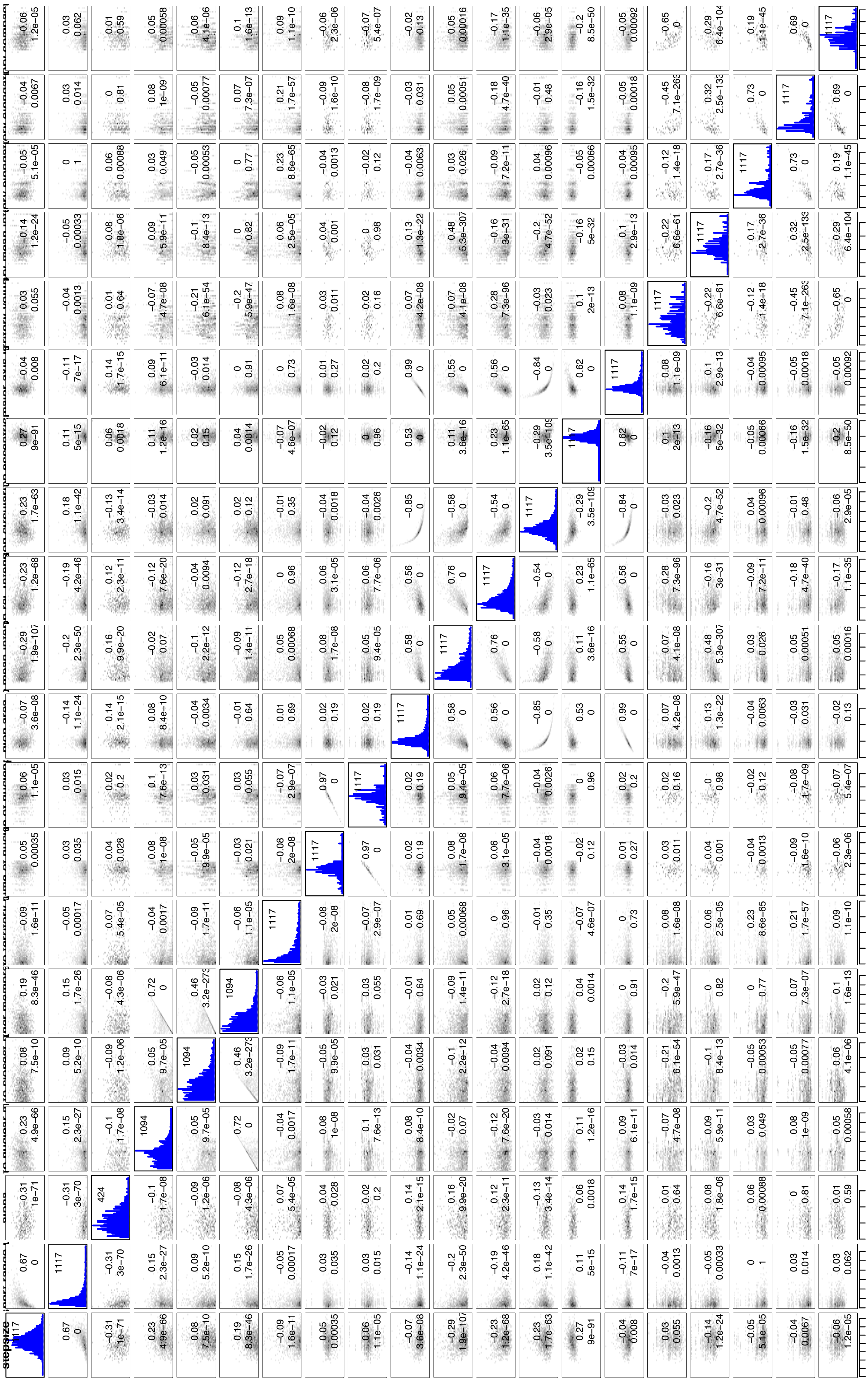

Figure 5-1 Pairplot Matrix showing Overview of entire Parameter Space

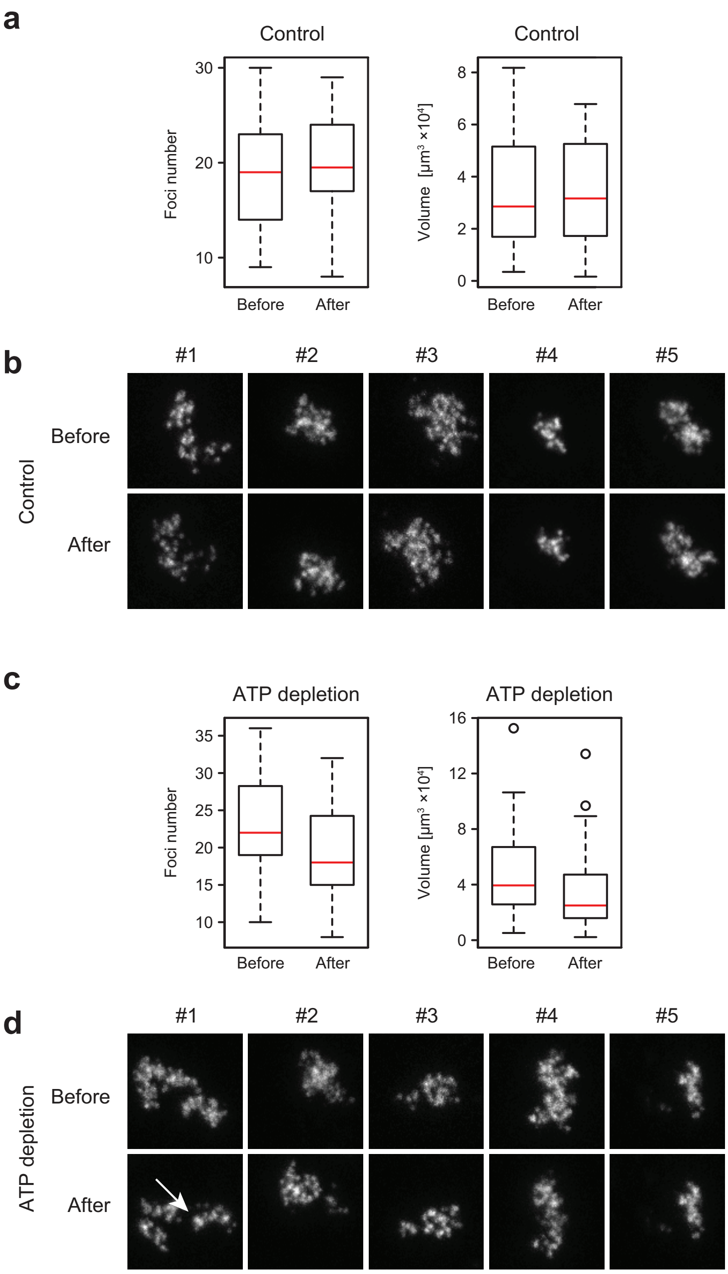

Figure 5-2 Photo-toxicity control for ATP depletion volume calculation
a, No significant change in RD number and CT territory volume before and after imaging of untreated control. **b,** examples of z-projected confocal stacks showing CTs before and after imaging of untreated control. **c,** RD number and CT territory volume decrease significantly before and after ATP depletion. **d,** examples of z-projected confocal stacks showing CTs before and after ATP depletion.

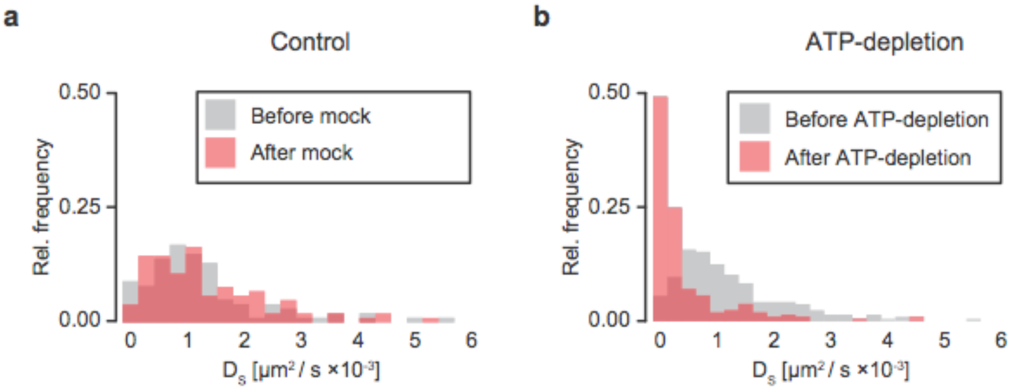

Figure 5-3 Photo-toxicity control for chromatin diffusion before and after ATP depletion.

a, CT was imaged before and after mock treatment, no significant change in chromatin dynamics is observed. **b,** CT was imaged before and after ATP depletion, a significant decrease in chromatin dynamics can be observed.

Bibliography

Abney, J.R., Cutler, B., Fillbach, M.L., Axelrod, D., and Scalettar, B.A. (1997). Chromatin dynamics in interphase nuclei and its implications for nuclear structure. The Journal of Cell Biology *137*, 1459–1468.

Albert, B., Mathon, J., Shukla, A., Saad, H., Normand, C., Léger-Silvestre, I., Villa, D., Kamgoue, A., Mozziconacci, J., Wong, H., et al. (2013). Systematic characterization of the conformation and dynamics of budding yeast chromosome XII. The Journal of Cell Biology *202*, 201–210.

Albiez, H., Cremer, M., Tiberi, C., Vecchio, L., Schermelleh, L., Dittrich, S., Küpper, K., Joffe, B., Thormeyer, T., Hase, von, J., et al. (2006). Chromatin domains and the interchromatin compartment form structurally defined and functionally interacting nuclear networks. Chromosome Res *14*, 707–733.

Amendola, M., and van Steensel, B. (2014). Mechanisms and dynamics of nuclear lamina-genome interactions. Current Opinion in Cell Biology *28*, 61–68.

Aquino, D., Schönle, A., Geisler, C., Middendorff, C.V., Wurm, C.A., Okamura, Y., Lang, T., Hell, S.W., and Egner, A. (2011). Two-color nanoscopy of three-dimensional volumes by 4Pi detection of stochastically switched fluorophores. Nat. Methods *8*, 353–359.

Baddeley, D., Chagin, V.O., Schermelleh, L., Martin, S., Pombo, A., Carlton, P.M., Gahl, A., Domaing, P., Birk, U., Leonhardt, H., et al. (2010). Measurement of replication structures at the nanometer scale using super-resolution light microscopy. Nucleic Acids Research *38*, e8–e8.

Bancaud, A., Huet, S., Daigle, N., Mozziconacci, J., Beaudouin, J., and Ellenberg, J. (2009). Molecular crowding affects diffusion and binding of nuclear proteins in heterochromatin and reveals the fractal organization of chromatin. The EMBO Journal *28*, 3785–3798.

Banterle, N., Bui, K.H., Lemke, E.A., and Beck, M. (2013). Fourier ring correlation as a resolution criterion for super-resolution microscopy. Journal of Structural Biology.

Bednar, J., Horowitz, R.A., Dubochet, J., and Woodcock, C.L. (1995). Chromatin conformation and salt-induced compaction: three-dimensional structural information from cryoelectron microscopy. The Journal of Cell Biology *131*, 1365–1376.

Belmont, A.S., and Bruce, K. (1994). Visualization of G1 chromosomes: a folded, twisted, supercoiled chromonema model of interphase chromatid structure. The Journal of Cell Biology *127*, 287–302.

Belmont, A.S. (2006). Mitotic chromosome structure and condensation. Current Opinion in Cell Biology *18*, 632–638.

Bensimon, A., Simon, A., Chiffaudel, A., Croquette, V., Heslot, F., and Bensimon, D. (1994). Alignment and sensitive detection of DNA by a moving interface. Science *265*, 2096–2098.

Berezney, R., Dubey, D.D., and Huberman, J.A. (2000). Heterogeneity of eukaryotic replicons, replicon clusters, and replication foci. Chromosoma *108*, 471–484.

Betzig, E., Lewis, A., Harootunian, A., Isaacson, M., and Kratschmer, E. (1986). Near Field Scanning Optical Microscopy (NSOM): Development and Biophysical Applications. Biophys. J. *49*, 269–279.

Betzig, E., Patterson, G.H., Sougrat, R., Lindwasser, O.W., Olenych, S., Bonifacino, J.S., Davidson, M.W., Lippincott-Schwartz, J., and Hess, H.F. (2006). Imaging intracellular fluorescent proteins at nanometer resolution. Science *313*, 1642–1645.

Bickmore, W.A., and van Steensel, B. (2013). Genome architecture: domain organization of interphase chromosomes. Cell *152*, 1270–1284.

Bolzer, A., Kreth, G., Solovei, I., Koehler, D., Saracoglu, K., Fauth, C., Müller, S., Eils, R., Cremer, C., Speicher, M.R., et al. (2005). Three-dimensional maps of all chromosomes in human male fibroblast nuclei and prometaphase rosettes. Plos Biol *3*, e157.

Bornfleth, H., Edelmann, P., Zink, D., Cremer, T., and Cremer, C. (1999). Quantitative motion analysis of subchromosomal foci in living cells using four-dimensional microscopy. Biophys. J. *77*, 2871–2886.

Boyle, S., Gilchrist, S., Bridger, J.M., Mahy, N.L., Ellis, J.A., and Bickmore, W.A. (2001). The spatial organization of human chromosomes within the nuclei of normal and emerin-mutant cells. Hum. Mol. Genet. *10*, 211–219.

Branco, M.R., and Pombo, A. (2006). Intermingling of Chromosome Territories in Interphase Suggests Role in Translocations and Transcription-Dependent Associations. Plos Biol *4*, e138.

Branco, M.R., and Pombo, A. (2007). Chromosome organization: new facts, new models. Trends in Cell Biology *17*, 127–134.

Bronstein, I., Israel, Y., Kepten, E., Mai, S., Shav-Tal, Y., Barkai, E., and Garini, Y. (2009). Transient Anomalous Diffusion of Telomeres in the Nucleus of Mammalian Cells. Phys. Rev. Lett. *103*.

Brown, C.R., and Silver, P.A. (2007). Transcriptional regulation at the nuclear pore complex. Curr. Opin. Genet. Dev.

Carreau, A., Hafny-Rahbi, El, B., Matejuk, A., Grillon, C., and Kieda, C. (2011). Why is the partial oxygen pressure of human tissues a crucial parameter? Small molecules and hypoxia. J. Cell. Mol. Med. *15*, 1239–1253.

Catté, F., Lions, P.-L., Morel, J.-M., and Coll, T. (1992). Image selective smoothing and edge detection by nonlinear diffusion. SIAM Journal on Numerical Analysis *29*, 182–193.

Chagin, V.O., Stear, J.H., and Cardoso, M.C. (2010). Organization of DNA Replication. Cold Spring Harb Perspect Biol *2*, a000737–a000737.

Chan, T.F., and Vese, L.A. (2001). Active contours without edges. IEEE Trans Image Process *10*, 266–277.

Chen, B., Gilbert, L.A., Cimini, B.A., Schnitzbauer, J., Zhang, W., Li, G.-W., Park, J., Blackburn, E.H., Weissman, J.S., Qi, L.S., et al. (2013). Dynamic imaging of genomic loci in living human cells by an optimized CRISPR/Cas system. Cell *155*, 1479–1491.

Chi, P., Allis, C.D., and Wang, G.G. (2010). Covalent histone modifications--miswritten, misinterpreted and mis-erased in human cancers. Nat Rev Cancer *10*, 457–469.

Chuang, C.-H., Carpenter, A.E., Fuchsova, B., Johnson, T., de Lanerolle, P., and Belmont, A.S. (2006). Long-range directional movement of an interphase chromosome site. Curr. Biol. *16*, 825–831.

Chubb, J.R., and Bickmore, W.A. (2003). Considering nuclear compartmentalization in the light of nuclear dynamics. Cell *112*, 403–406.

Chubb, J.R., Boyle, S., Perry, P., and Bickmore, W.A. (2002). Chromatin motion is constrained by association with nuclear compartments in human cells. Curr. Biol. *12*, 439–445.

Cook, P.R. (1999). The organization of replication and transcription. Science *284*, 1790–1795.

Cremer, T., and Cremer, C. (2001). Chromosome territories, nuclear architecture and gene regulation in mammalian cells. Nat. Rev. Genet. *2*, 292–301.

Cremer, T., Cremer, C., Schneider, T., Baumann, H., Hens, L., and Kirsch-Volders, M. (1982). Analysis of chromosome positions in the interphase nucleus of Chinese hamster cells by laser-UV-microirradiation experiments. Hum. Genet. *62*, 201–209.

Cremer, T., Kurz, A., Zirbel, R., Dietzel, S., Rinke, B., Schröck, E., Speicher, M.R., Mathieu, U., Jauch, A., Emmerich, P., et al. (1993). Role of chromosome territories in the functional compartmentalization of the cell nucleus. Cold Spring Harbor Symposia on Quantitative Biology *58*, 777–792.

Crocker, J.C., and Grier, D.G. (1996). Methods of Digital Video Microscopy for Colloidal Studies. Journal of Colloid and Interface Science 1–13.

Croft, J.A., Bridger, J.M., Boyle, S., Perry, P., Teague, P., and Bickmore, W.A. (1999). Differences in the localization and morphology of chromosomes in the human nucleus. The Journal of Cell Biology *145*, 1119–1131.

Cseresnyes, Z., Schwarz, U., and Green, C.M. (2009). Analysis of replication factories in human cells by super-resolution light microscopy. BMC Cell Biol *10*, 88.

Daszykowski, M., Walczak, B., and Massart, D.L. (2002). Looking for natural patterns in analytical data. 2. Tracing local density with OPTICS. J Chem Inf Comput Sci *42*, 500–507.

de Chaumont, F., Dallongeville, S., Provoost, T., Lecomte, T., Dufour, A., and Olivo-Marin, J.C. (2013). Icy: A user-friendly environment for algorithm development and deployment. 1–5.

de Laat, W., and Dekker, J. (2012). 3C-based technologies to study the shape of the genome. Methods *58*, 189–191.

de Wit, E., and de Laat, W. (2012). A decade of 3C technologies: insights into nuclear organization. Genes & Development *26*, 11–24.

Dehghani, H., Dellaire, G., and Bazett-Jones, D.P. (2005). Organization of chromatin in the interphase mammalian cell. Micron.

Dekker, J., Rippe, K., Dekker, M., and Kleckner, N. (2002). Capturing chromosome conformation. Science *295*, 1306–1311.

Demmerle, J., Koch, A.J., and Holaska, J.M. (2012). The nuclear envelope protein emerin binds directly to histone deacetylase 3 (HDAC3) and activates HDAC3 activity. Journal of Biological Chemistry *287*, 22080–22088.

Dempsey, G.T., Vaughan, J.C., Chen, K.H., Bates, M., and Zhuang, X. (2011). Evaluation of fluorophores for optimal performance in localization-based super-resolution imaging. Nat. Methods *8*, 1027–1036.

Deschamps, J., Mund, M., and Ries, J. (2014). 3D superresolution microscopy by supercritical angle detection. Opt. Express *22*, 29081–29091.

Dixit, R., and Cyr, R. (2003). Cell damage and reactive oxygen species production induced by fluorescence microscopy: effect on mitosis and guidelines for non-invasive fluorescence microscopy. Plant J. *36*, 280–290.

Dixon, J.R., Jung, I., Selvaraj, S., Shen, Y., Antosiewicz-Bourget, J.E., Lee, A.Y., Ye, Z., Kim, A., Rajagopal, N., Xie, W., et al. (2015). Chromatin architecture reorganization during stem cell differentiation. Nature *518*, 331–336.

Dixon, J.R., Selvaraj, S., Yue, F., Kim, A., Li, Y., Shen, Y., Hu, M., Liu, J.S., and Ren, B. (2012). Topological domains in mammalian genomes identified by analysis of chromatin interactions. Nature.

Dostie, J., Richmond, T.A., Arnaout, R.A., Selzer, R.R., Lee, W.L., Honan, T.A., Rubio, E.D., Krumm, A., Lamb, J., Nusbaum, C., et al. (2006). Chromosome Conformation Capture Carbon Copy (5C): a massively parallel solution for mapping interactions between genomic elements. Genome Res. *16*, 1299–1309.

Dultz, E., Zanin, E., Wurzenberger, C., Braun, M., Rabut, G., Sironi, L., and Ellenberg, J. (2008). Systematic kinetic analysis of mitotic dis- and reassembly of the nuclear pore in living cells. The Journal of Cell Biology *180*, 857–865.

Dundr, M., Ospina, J.K., Sung, M.H., and John, S. (2007). Actin-dependent intranuclear repositioning of an active gene locus in vivo. The Journal of Cell ….

Dyba, M., and Hell, S.W. (2002). Focal spots of size lambda/23 open up far-field fluorescence microscopy at 33 nm axial resolution. Phys. Rev. Lett. *88*, 163901.

Edelmann, P., Bornfleth, H., Zink, D., Cremer, T., and Cremer, C. (2001). Morphology and dynamics of chromosome territories in living cells. Biochim. Biophys. Acta *1551*, M29–M39.

ENCODE Project Consortium, Bernstein, B.E., Birney, E., Dunham, I., Green, E.D., Gunter, C., and Snyder, M. (2012). An integrated encyclopedia of DNA elements in the human genome. Nature *489*, 57–74.

Ester, M., Kriegel, H.-P., Sander, J., and Xu, X. (1996). A Density-Based Algorithm for Discovering Clusters in Large Spatial Databases with Noise

. Proceedings of 2nd International Conference on Knowledge Discovery and Data Mining *27*, i205–i213.

Ferreira, J., Paolella, G., Ramos, C., and Lamond, A.I. (1997). Spatial organization of large-scale chromatin domains in the nucleus: a magnified view of single chromosome territories. The Journal of Cell Biology *139*, 1597–1610.

Fiolka, R., Shao, L., Rego, E.H., Davidson, M.W., and Gustafsson, M.G.L. (2012). Time-lapse two-color 3D imaging of live cells with doubled resolution using structured illumination. Proceedings of the National Academy of Sciences *109*, 5311–5315.

Fox, A.H., and Lamond, A.I. (2010). Paraspeckles. Cold Spring Harb Perspect Biol *2*, a000687–a000687.

Fölling, J., Bossi, M., Bock, H., Medda, R., Wurm, C.A., Hein, B., Jakobs, S., Eggeling, C., and Hell, S.W. (2008). Fluorescence nanoscopy by ground-state depletion and single-molecule return. Nat. Methods *5*, 943–945.

Francis, N.J. (2004). Chromatin Compaction by a Polycomb Group Protein Complex. Science *306*, 1574–1577.

Fussner, E., Ching, R.W., and Bazett-Jones, D.P. (2011). Living without 30nm chromatin fibers. Trends Biochem. Sci. *36*, 1–6.

Gall, J.G. (1966). Chromosome fibers studied by a spreading technique. Chromosoma *20*, 221–233.

Gerlich, D., Beaudouin, J., Kalbfuss, B., Daigle, N., Eils, R., and Ellenberg, J. (2003). Global chromosome positions are transmitted through mitosis in mammalian cells. Cell *112*, 751–764.

Gialitakis, M., Kretsovali, A., Spilianakis, C., Kravariti, L., Mages, J., Hoffmann, R., Hatzopoulos, A.K., and Papamatheakis, J. (2006). Coordinated changes of histone modifications and HDAC mobilization regulate the induction of MHC class II genes by Trichostatin A. Nucleic Acids Research *34*, 765–772.

Gilbert, D.M. (2010). Evaluating genome-scale approaches to eukaryotic DNA replication. Nat. Rev. Genet. *11*, 673–684.

Gilbert, D.M. (2012). Replication origins run (ultra) deep. Nat. Struct. Mol. Biol. *19*, 740–742.

Gilbert, N., Boyle, S., Fiegler, H., Woodfine, K., Carter, N.P., and Bickmore, W.A. (2004). Chromatin architecture of the human genome: gene-rich domains are enriched in open chromatin fibers. Cell *118*, 555–566.

Görisch, S.M., Wachsmuth, M., Tóth, K.F., Lichter, P., and Rippe, K. (2005). Histone acetylation increases chromatin accessibility. Journal of Cell Science *118*, 5825–5834.

Grotjohann, T., Testa, I., Leutenegger, M., Bock, H., Urban, N.T., Lavoie-Cardinal, F., Willig, K.I., Eggeling, C., Jakobs, S., and Hell, S.W. (2011). Diffraction-unlimited all-optical imaging and writing with a photochromic GFP. Nature *478*, 204–208.

Guelen, L., Pagie, L., Brasset, E., Meuleman, W., Faza, M.B., Talhout, W., Eussen, B.H., de Klein, A., Wessels, L., de Laat, W., et al. (2008). Domain organization of human chromosomes revealed by mapping of nuclear lamina interactions. Nature *453*, 948–951.

Guilbaud, G., Rappailles, A., Baker, A., Chen, C.-L., Arneodo, A., Goldar, A., d'Aubenton-Carafa, Y., Thermes, C., Audit, B., and Hyrien, O. (2011). Evidence for sequential and increasing activation of replication origins along replication timing gradients in the human genome. PLoS Computational Biology *7*, e1002322.

Gustafsson, M.G.L. (2000). Surpassing the lateral resolution limit by a factor of two using structured illumination microscopy. SHORT COMMUNICATION. J Microsc *198*, 82–87.

Gustafsson, M.G.L. (2005). Nonlinear structured-illumination microscopy: Wide-field fluorescence imaging with theoretically unlimited resolution. Proceedings of the National Academy of Sciences *102*, 13081–13086.

Gustafsson, M.G.L., Shao, L., Carlton, P.M., Wang, C.J.R., Golubovskaya, I.N., Cande, W.Z., Agard, D.A., and Sedat, J.W. (2008). Three-Dimensional Resolution Doubling in Wide-Field Fluorescence Microscopy by Structured Illumination. Biophys. J. *94*, 4957–4970.

Hajjoul, H., Mathon, J., Ranchon, H., Goiffon, I., Mozziconacci, J., Albert, B., Carrivain, P., Victor, J.-M., Gadal, O., Bystricky, K., et al. (2013). High-throughput chromatin motion tracking in living yeast reveals the flexibility of the fiber throughout the genome. Genome Res. *23*, 1829–1838.

Hamilton, C., Hayward, R.L., and Gilbert, N. (2011). Global chromatin fibre compaction in response to DNA damage. Biochemical and Biophysical Research Communications *414*, 820–825.

Hansen, R.S., Thomas, S., Sandstrom, R., Canfield, T.K., Thurman, R.E., Weaver, M., Dorschner, M.O., Gartler, S.M., and Stamatoyannopoulos, J.A. (2010).

Sequencing newly replicated DNA reveals widespread plasticity in human replication timing. Proceedings of the National Academy of Sciences *107*, 139–144.

Heilemann, M., van de Linde, S., Schüttpelz, M., Kasper, R., Seefeldt, B., Mukherjee, A., Tinnefeld, P., and Sauer, M. (2008). Subdiffraction-resolution fluorescence imaging with conventional fluorescent probes. Angew. Chem. Int. Ed. Engl. *47*, 6172–6176.

Hell, S.W. (2007). Far-field optical nanoscopy. Science *316*, 1153–1158.

Hell, S.W., and Wichmann, J. (1994). Breaking the diffraction resolution limit by stimulated emission: stimulated-emission-depletion fluorescence microscopy. Opt Lett *19*, 780.

Hess, S.T., Girirajan, T.P.K., and Mason, M.D. (2006). Ultra-high resolution imaging by fluorescence photoactivation localization microscopy. Biophys. J. *91*, 4258–4272.

Heun, P., Laroche, T., Shimada, K., Furrer, P., and Gasser, S.M. (2001). Chromosome dynamics in the yeast interphase nucleus. Science *294*, 2181–2186.

Hills, G.M. (1940). The metabolism of articular cartilage. Biochemical Journal *34*, 1070.

Hinde, E., Cardarelli, F., Digman, M.A., and Gratton, E. (2012). Changes in chromatin compaction during the cell cycle revealed by micrometer-scale measurement of molecular flow in the nucleus. Biophys. J. *102*, 691–697.

Hiratani, I., Ryba, T., Itoh, M., Yokochi, T., Schwaiger, M., Chang, C.-W., Lyou, Y., Townes, T.M., Schübeler, D., and Gilbert, D.M. (2008). Global reorganization of replication domains during embryonic stem cell differentiation. Plos Biol *6*, e245.

Hochstrasser, M., Mathog, D., Gruenbaum, Y., Saumweber, H., and Sedat, J.W. (1986). Spatial organization of chromosomes in the salivary gland nuclei of Drosophila melanogaster. The Journal of Cell Biology *102*, 112–123.

Horowitz, R.A., Agard, D.A., Sedat, J.W., and Woodcock, C.L. (1994). The three-dimensional architecture of chromatin in situ: electron tomography reveals fibers composed of a continuously variable zig-zag nucleosomal ribbon. The Journal of Cell Biology *125*, 1–10.

Hou, C., Li, L., Qin, Z.S., and Corces, V.G. (2012). Gene density, transcription, and insulators contribute to the partition of the Drosophila genome into physical domains. Molecular Cell *48*, 471–484.

Huang, B., Wang, W., Bates, M., and Zhuang, X. (2008). Three-dimensional super-resolution imaging by stochastic optical reconstruction microscopy. Science *319*, 810–813.

Huberman, J.A., and Riggs, A.D. (1968). On the mechanism of DNA replication in mammalian chromosomes. Journal of Molecular Biology *32*, 327–341.

Imakaev, M., Fudenberg, G., McCord, R.P., Naumova, N., Goloborodko, A., Lajoie, B.R., Dekker, J., and Mirny, L.A. (2012). Iterative correction of Hi-C data reveals hallmarks of chromosome organization. Nat. Methods *9*, 999–1003.

Jackson, D.A., and Pombo, A. (1998). Replicon clusters are stable units of chromosome structure: evidence that nuclear organization contributes to the efficient activation and propagation of S phase in human cells. The Journal of Cell Biology *140*, 1285–1295.

Jacobs, S.A., Taverna, S.D., Zhang, Y., Briggs, S.D., Li, J., Eissenberg, J.C., Allis, C.D., and Khorasanizadeh, S. (2001). Specificity of the HP1 chromo domain for the methylated N-terminus of histone H3. The EMBO Journal *20*, 5232–5241.

Jaqaman, K., Loerke, D., Mettlen, M., Kuwata, H., Grinstein, S., Schmid, S.L., and Danuser, G. (2008). Robust single-particle tracking in live-cell time-lapse sequences. Nat. Methods *5*, 695–702.

Jin, F., Li, Y., Dixon, J.R., Selvaraj, S., Ye, Z., Lee, A.Y., Yen, C.-A., Schmitt, A.D., Espinoza, C.A., and Ren, B. (2013). A high-resolution map of the three-dimensional chromatin interactome in human cells. Nature *503*, 290–294.

Juette, M.F., Gould, T.J., Lessard, M.D., Mlodzianoski, M.J., Nagpure, B.S., Bennett, B.T., Hess, S.T., and Bewersdorf, J. (2008). Three-dimensional sub-100 nm resolution fluorescence microscopy of thick samples. Nat. Methods *5*, 527–529.

Kalhor, R., Tjong, H., Jayathilaka, N., Alber, F., and Chen, L. (2012). Genome architectures revealed by tethered chromosome conformation capture and population-based modeling. Nature Biotechnology *30*, 90–98.

Kapoor, P., and Shen, X. (2014). Mechanisms of nuclear actin in chromatin-remodeling complexes. Trends in Cell Biology *24*, 238–246.

Kind, J., Pagie, L., Ortabozkoyun, H., Boyle, S., de Vries, S.S., Janssen, H., Amendola, M., Nolen, L.D., Bickmore, W.A., and van Steensel, B. (2013). Single-cell dynamics of genome-nuclear lamina interactions. Cell *153*, 178–192.

Klar, T.A., Jakobs, S., Dyba, M., Egner, A., and Hell, S.W. (2000). Fluorescence microscopy with diffraction resolution barrier broken by stimulated emission. Proc.

Natl. Acad. Sci. U.S.a. *97*, 8206–8210.

Kner, P., Chhun, B.B., Griffis, E.R., Winoto, L., and Gustafsson, M.G.L. (2009). Super-resolution video microscopy of live cells by structured illumination. Nat. Methods *6*, 339–342.

Kruhlak, M.J., Celeste, A., Dellaire, G., Fernandez-Capetillo, O., Müller, W.G., McNally, J.G., Bazett-Jones, D.P., and Nussenzweig, A. (2006). Changes in chromatin structure and mobility in living cells at sites of DNA double-strand breaks. The Journal of Cell Biology *172*, 823–834.

Kumar, A., Mazzanti, M., Mistrik, M., Kosar, M., Beznoussenko, G.V., Mironov, A.A., Garrè, M., Parazzoli, D., Shivashankar, G.V., Scita, G., et al. (2014). ATR mediates a checkpoint at the nuclear envelope in response to mechanical stress. Cell *158*, 633–646.

Kumaran, R.I., and Spector, D.L. (2008). A genetic locus targeted to the nuclear periphery in living cells maintains its transcriptional competence. The Journal of Cell Biology *180*, 51–65.

Kuroda, M., Tanabe, H., Yoshida, K., Oikawa, K., Saito, A., Kiyuna, T., Mizusawa, H., and Mukai, K. (2004). Alteration of chromosome positioning during adipocyte differentiation. Journal of Cell Science *117*, 5897–5903.

Kurz, A., Lampel, S., Nickolenko, J.E., Bradl, J., Benner, A., Zirbel, R.M., Cremer, T., and Lichter, P. (1996). Active and inactive genes localize preferentially in the periphery of chromosome territories. The Journal of Cell Biology *135*, 1195–1205.

Lachner, M., O'Carroll, D., Rea, S., Mechtler, K., and Jenuwein, T. (2001). Methylation of histone H3 lysine 9 creates a binding site for HP1 proteins. Nature *410*, 116–120.

Lanctot, C., Cheutin, T., Cremer, M., Cavalli, G., and Cremer, T. (2007). Dynamic genome architecture in the nuclear space: regulation of gene expression in three dimensions. Nat. Rev. Genet. *8*, 104–115.

Langmore, J.P., and Schutt, C. (1980). The higher order structure of chicken erythrocyte chromosomes in vivo. Nature *288*, 620–622.

Lenhard, B., Sandelin, A., and Carninci, P. (2012). Metazoan promoters: emerging characteristics and insights into transcriptional regulation. Nat. Rev. Genet. *13*, 233–245.

Leonhardt, H., Rahn, H.P., Weinzierl, P., Sporbert, A., Cremer, T., Zink, D., and

Cardoso, M.C. (2000). Dynamics of DNA replication factories in living cells. The Journal of Cell Biology *149*, 271–280.

Letourneau, A., Santoni, F.A., Bonilla, X., Sailani, M.R., Gonzalez, D., Kind, J., Chevalier, C., Thurman, R., Sandstrom, R.S., Hibaoui, Y., et al. (2014). Domains of genome-wide gene expression dysregulation in Down's syndrome. Nature *508*, 345–350.

Levi, V., Ruan, Q., Plutz, M., Belmont, A.S., and Gratton, E. (2005). Chromatin Dynamics in Interphase Cells Revealed by Tracking in a Two-Photon Excitation Microscope. Biophys. J. *89*, 4275–4285.

Lichter, P., Cremer, T., Borden, J., Manuelidis, L., and Ward, D.C. (1988). Delineation of individual human chromosomes in metaphase and interphase cells by in situ suppression hybridization using recombinant DNA libraries. Hum. Genet. *80*, 224–234.

Lieberman-Aiden, E., van Berkum, N.L., Williams, L., Imakaev, M., Ragoczy, T., Telling, A., Amit, I., Lajoie, B.R., Sabo, P.J., Dorschner, M.O., et al. (2009). Comprehensive mapping of long-range interactions reveals folding principles of the human genome. Science *326*, 289–293.

Lleres, D., James, J., Swift, S., Norman, D.G., and Lamond, A.I. (2009). Quantitative analysis of chromatin compaction in living cells using FLIM-FRET. The Journal of Cell Biology *187*, 481–496.

Lucas, J.S., Zhang, Y., Dudko, O.K., and Murre, C. (2014). 3D trajectories adopted by coding and regulatory DNA elements: first-passage times for genomic interactions. Cell *158*, 339–352.

Luger, K., Mäder, A.W., Richmond, R.K., Sargent, D.F., and Richmond, T.J. (1997). Crystal structure of the nucleosome core particle at 2.8 A resolution. Nature *389*, 251–260.

Lupiáñez, D.G., Kraft, K., Heinrich, V., Krawitz, P., Brancati, F., Klopocki, E., Horn, D., Kayserili, H., Opitz, J.M., Laxova, R., et al. (2015). Disruptions of topological chromatin domains cause pathogenic rewiring of gene-enhancer interactions. Cell *161*, 1012–1025.

Ma, H., Samarabandu, J., Devdhar, R.S., Acharya, R., Cheng, P.C., Meng, C., and Berezney, R. (1998). Spatial and temporal dynamics of DNA replication sites in mammalian cells. The Journal of Cell Biology *143*, 1415–1425.

Maeshima, K., Hihara, S., and Eltsov, M. (2010). Chromatin structure: does the 30-

nm fibre exist in vivo? Current Opinion in Cell Biology *22*, 291–297.

Maeshima, K., Imai, R., Tamura, S., and Nozaki, T. (2014). Chromatin as dynamic 10-nm fibers. Chromosoma *123*, 225–237.

Mahy, N.L., Perry, P.E., and Bickmore, W.A. (2002). Gene density and transcription influence the localization of chromatin outside of chromosome territories detectable by FISH. The Journal of Cell Biology *159*, 753–763.

Manders, E.M., Stap, J., Brakenhoff, G.J., van Driel, R., and Aten, J.A. (1992). Dynamics of three-dimensional replication patterns during the S-phase, analysed by double labelling of DNA and confocal microscopy. Journal of Cell Science *103 (Pt 3)*, 857–862.

Manders, E.M., Stap, J., Strackee, J., van Driel, R., and Aten, J.A. (1996). Dynamic behavior of DNA replication domains. Experimental Cell Research *226*, 328–335.

Mao, Y.S., Zhang, B., and Spector, D.L. (2011). Biogenesis and function of nuclear bodies. Trends Genet. *27*, 295–306.

Marcus, R.E. (1973). The effect of low oxygen concentration on growth, glycolysis, and sulfate incorporation by articular chondrocytes in monolayer culture. Arthritis Rheum. *16*, 646–656.

Marshall, W.F., Straight, A., Marko, J.F., SWEDLOW, J., Dernburg, A., Belmont, A., Murray, A.W., Agard, D.A., and Sedat, J.W. (1997). Interphase chromosomes undergo constrained diffusional motion in living cells. Curr. Biol. *7*, 930–939.

Martin, R.M., Görisch, S.M., Leonhardt, H., and Cardoso, M.C. (2007). An unexpected link between energy metabolism, calcium, chromatin condensation and cell cycle. Cc *6*, 2422–2424.

Maya-Mendoza, A., Olivares-Chauvet, P., Shaw, A., and Jackson, D.A. (2010). S phase progression in human cells is dictated by the genetic continuity of DNA foci. PLoS Genet *6*, e1000900.

McDowall, A.W., Smith, J.M., and Dubochet, J. (1986). Cryo-electron microscopy of vitrified chromosomes in situ. The EMBO Journal *5*, 1395–1402.

Meaburn, K.J., and Misteli, T. (2007). Cell biology: chromosome territories. Nature *445*, 379–781.

Meshorer (2008). Imaging chromatin in embryonic stem cells. StemBook.

Misteli, T. (2007). Beyond the Sequence: Cellular Organization of Genome Function.

Cell *128*, 787–800.

Moffitt, J.R., Osseforth, C., and Michaelis, J. (2011). Time-gating improves the spatial resolution of STED microscopy. Opt. Express *19*, 4242–4254.

Moindrot, B., Audit, B., Klous, P., Baker, A., Thermes, C., de Laat, W., Bouvet, P., Mongelard, F., and Arneodo, A. (2012). 3D chromatin conformation correlates with replication timing and is conserved in resting cells. Nucleic Acids Research *40*, 9470–9481.

Morris, G.E. (2008). The Cajal body. Biochim. Biophys. Acta *1783*, 2108–2115.

Müller, I., Boyle, S., Singer, R.H., Bickmore, W.A., and Chubb, J.R. (2010). Stable Morphology, but Dynamic Internal Reorganisation, of Interphase Human Chromosomes in Living Cells. PLoS ONE *5*, e11560.

Nakamura, H., Morita, T., and Sato, C. (1986). Structural organizations of replicon domains during DNA synthetic phase in the mammalian nucleus. Experimental Cell Research *165*, 291–297.

Nägerl, U.V., Willig, K.I., Hein, B., Hell, S.W., and Bonhoeffer, T. (2008). Live-cell imaging of dendritic spines by STED microscopy. Proceedings of the National Academy of Sciences *105*, 18982–18987.

Németh, A., and Längst, G. (2011). Genome organization in and around the nucleolus. Trends Genet.

Nieuwenhuizen, R.P.J., Lidke, K.A., Bates, M., Puig, D.L., Grünwald, D., Stallinga, S., and Rieger, B. (2013). Measuring image resolution in optical nanoscopy. Nat. Methods *10*, 557–562.

Nora, E.P., Dekker, J., and Heard, E. (2013). Segmental folding of chromosomes: a basis for structural and regulatory chromosomal neighborhoods? Bioessays *35*, 818–828.

Nora, E.P., Lajoie, B.R., Schulz, E.G., Giorgetti, L., Okamoto, I., Servant, N., Piolot, T., van Berkum, N.L., Meisig, J., Sedat, J., et al. (2012). Spatial partitioning of the regulatory landscape of the X-inactivation centre. Nature.

Norio, P., Kosiyatrakul, S., Yang, Q., Guan, Z., Brown, N.M., Thomas, S., Riblet, R., and Schildkraut, C.L. (2005). Progressive activation of DNA replication initiation in large domains of the immunoglobulin heavy chain locus during B cell development. Molecular Cell *20*, 575–587.

Olins, D.E., and Olins, A.L. (2003). Chromatin history: our view from the bridge. Nat

Rev Mol Cell Biol *4*, 809–814.

Olivier, N., Keller, D., Rajan, V.S., Gönczy, P., and Manley, S. (2013). Simple buffers for 3D STORM microscopy. Biomed Opt Express *4*, 885–899.

Padeken, J., and Heun, P. (2014). Nucleolus and nuclear periphery: velcro for heterochromatin. Current Opinion in Cell Biology *28*, 54–60.

Palumbo, E., Tosoni, E., and Russo, A. (2013). General and specific replication profiles are detected in normal human cells by genome-wide and single-locus molecular combing. Experimental Cell Research *319*, 3081–3093.

Parada, L.A., McQueen, P.G., and Misteli, T. (2004). Tissue-specific spatial organization of genomes. Genome Biol. *5*, R44.

Parada, L.A., McQueen, P.G., Munson, P.J., and Misteli, T. (2002). Conservation of relative chromosome positioning in normal and cancer cells. Curr. Biol. *12*, 1692–1697.

Parada, L.A., Roix, J.J., and Misteli, T. (2003). An uncertainty principle in chromosome positioning. Trends in Cell Biology *13*, 393–396.

Paulson, J.R., and Langmore, J.P. (1983). Low angle x-ray diffraction studies of HeLa metaphase chromosomes: effects of histone phosphorylation and chromosome isolation procedure. The Journal of Cell Biology *96*, 1132–1137.

Pavani, S.R.P., Thompson, M.A., Biteen, J.S., Lord, S.J., Liu, N., Twieg, R.J., Piestun, R., and Moerner, W.E. (2009). Three-dimensional, single-molecule fluorescence imaging beyond the diffraction limit by using a double-helix point spread function. Proceedings of the National Academy of Sciences *106*, 2995–2999.

Pederson, T., and Aebi, U. (2005). Nuclear actin extends, with no contraction in sight. Mol. Biol. Cell *16*, 5055–5060.

Perona, P., and Malik, J. (1990). Scale-space and edge detection using anisotropic diffusion. IEEE Transactions on Pattern Analysis and Machine Intelligence *12*, 629–639.

Phair, R.D., and Misteli, T. (2000). High mobility of proteins in the mammalian cell nucleus. Nature *404*, 604–609.

Pinheiro, I., Margueron, R., Shukeir, N., Eisold, M., Fritzsch, C., Richter, F.M., Mittler, G., Genoud, C., Goyama, S., Kurokawa, M., et al. (2012). Prdm3 and Prdm16 are H3K9me1 methyltransferases required for mammalian heterochromatin integrity. Cell *150*, 948–960.

Pliss, A., Malyavantham, K.S., Bhattacharya, S., and Berezney, R. (2013). Chromatin dynamics in living cells: identification of oscillatory motion. J. Cell. Physiol. *228*, 609–616.

Pliss, A., Malyavantham, K., Bhattacharya, S., Zeitz, M., and Berezney, R. (2009). Chromatin dynamics is correlated with replication timing. Chromosoma *118*, 459–470.

Pope, B.D., and Gilbert, D.M. (2013). The replication domain model: regulating replicon firing in the context of large-scale chromosome architecture. Journal of Molecular Biology *425*, 4690–4695.

Pope, B.D., Ryba, T., Dileep, V., Yue, F., Wu, W., Denas, O., Vera, D.L., Wang, Y., Hansen, R.S., Canfield, T.K., et al. (2014). Topologically associating domains are stable units of replication-timing regulation. Nature *515*, 402–405.

Prokocimer, M., Davidovich, M., Nissim-Rafinia, M., Wiesel-Motiuk, N., Bar, D.Z., Barkan, R., Meshorer, E., and Gruenbaum, Y. (2009). Nuclear lamins: key regulators of nuclear structure and activities. J. Cell. Mol. Med. *13*, 1059–1085.

Rao, S.S.P., Huntley, M.H., Durand, N.C., Stamenova, E.K., Bochkov, I.D., Robinson, J.T., Sanborn, A.L., Machol, I., Omer, A.D., Lander, E.S., et al. (2014). A 3D Map of the Human Genome at Kilobase Resolution Reveals Principles of Chromatin Looping. Cell *159*, 1665–1680.

Reddy, K.L., Zullo, J.M., Bertolino, E., and Singh, H. (2008). Transcriptional repression mediated by repositioning of genes to the nuclear lamina. Nature *452*, 243–247.

Rhind, N., and Gilbert, D.M. (2013). DNA replication timing. Cold Spring Harb Perspect Biol *5*, a010132.

Ricci, M.A., Manzo, C., García-Parajo, M.F., Lakadamyali, M., and Cosma, M.P. (2015). Chromatin fibers are formed by heterogeneous groups of nucleosomes in vivo. Cell *160*, 1145–1158.

Robinson, P.J.J., Fairall, L., Huynh, V.A.T., and Rhodes, D. (2006). EM measurements define the dimensions of the “30-nm” chromatin fiber: evidence for a compact, interdigitated structure. Proc. Natl. Acad. Sci. U.S.a. *103*, 6506–6511.

Rouquette, J., Cremer, C., Cremer, T., and Fakan, S. (2010). Functional Nuclear Architecture Studied by Microscopy: Present and Future (Elsevier Inc.).

Rust, M.J., Bates, M., and Zhuang, X. (2006). Sub-diffraction-limit imaging by stochastic optical reconstruction microscopy (STORM). Nat. Methods *3*, 793–795.

Ryba, T., Hiratani, I., Lu, J., Itoh, M., Kulik, M., Zhang, J., Schulz, T.C., Robins, A.J., Dalton, S., and Gilbert, D.M. (2010). Evolutionarily conserved replication timing profiles predict long-range chromatin interactions and distinguish closely related cell types. *20*, 761–770.

Sadoni, N. (2004). Stable chromosomal units determine the spatial and temporal organization of DNA replication. Journal of Cell Science *117*, 5353–5365.

Saxton, M.J. (1997). Single-particle tracking: the distribution of diffusion coefficients. Biophys. J. *72*, 1744–1753.

Sbalzarini, I.F., and Koumoutsakos, P. (2005). Feature point tracking and trajectory analysis for video imaging in cell biology. Journal of Structural Biology *151*, 182–195.

Schalch, T., Duda, S., Sargent, D.F., and Richmond, T.J. (2005). X-ray structure of a tetranucleosome and its implications for the chromatin fibre. Nature *436*, 138–141.

Schermelleh, L., Markaki, Y., Eick, D., and Cardoso, M.C. FUNCTIONAL NUCLEAR TOPOLOGY ANALYZED WITH 3-DIMENSIONAL STRUCTURED ILLUMINATION MICROSCOPY (3D-SIM). Focusonmicroscopy.org

.

Schermelleh, L., Solovei, I., Zink, D., and Cremer, T. (2001). Two-color fluorescence labeling of early and mid-to-late replicating chromatin in living cells. Chromosome Res *9*, 77–80.

Schubert, I., and Shaw, P. (2011). Organization and dynamics of plant interphase chromosomes. Trends Plant Sci. *16*, 273–281.

Schwaiger, M., Stadler, M.B., Bell, O., Kohler, H., Oakeley, E.J., and Schübeler, D. (2009). Chromatin state marks cell-type- and gender-specific replication of the Drosophila genome. Genes & Development *23*, 589–601.

Schweitzer, C., and Schmidt, R. (2003). Physical mechanisms of generation and deactivation of singlet oxygen. Chem. Rev. *103*, 1685–1757.

Sexton, T., and Cavalli, G. (2015). The role of chromosome domains in shaping the functional genome. Cell *160*, 1049–1059.

Sexton, T., Schober, H., Fraser, P., and Gasser, S.M. (2007). Gene regulation through nuclear organization. Nat. Struct. Mol. Biol. *14*, 1049–1055.

Sexton, T., Yaffe, E., Kenigsberg, E., Bantignies, F., Leblanc, B., Hoichman, M., Parrinello, H., Tanay, A., and Cavalli, G. (2012). Three-dimensional folding and functional organization principles of the Drosophila genome. Cell *148*, 458–472.

Shao, L., Isaac, B., Uzawa, S., Agard, D.A., Sedat, J.W., and Gustafsson, M.G.L. (2008). I5S: wide-field light microscopy with 100-nm-scale resolution in three dimensions. Biophys. J. *94*, 4971–4983.

Shao, L., Kner, P., Rego, E.H., and Gustafsson, M.G.L. (2011). Super-resolution 3D microscopy of live whole cells using structured illumination. Nat. Methods *8*, 1044–1046.

Shtengel, G., Galbraith, J.A., Galbraith, C.G., Lippincott-Schwartz, J., Gillette, J.M., Manley, S., Sougrat, R., Waterman, C.M., Kanchanawong, P., Davidson, M.W., et al. (2009). Interferometric fluorescent super-resolution microscopy resolves 3D cellular ultrastructure. Proceedings of the National Academy of Sciences *106*, 3125–3130.

Simonis, M., Klous, P., Splinter, E., Moshkin, Y., Willemsen, R., de Wit, E., van Steensel, B., and de Laat, W. (2006). Nuclear organization of active and inactive chromatin domains uncovered by chromosome conformation capture-on-chip (4C). Nat. Genet. *38*, 1348–1354.

Sinclair, P., Bian, Q., Plutz, M., Heard, E., and Belmont, A.S. (2010). Dynamic plasticity of large-scale chromatin structure revealed by self-assembly of engineered chromosome regions. The Journal of Cell Biology *190*, 761–776.

Solovei, I., Kreysing, M., Lanctot, C., Kosem, S., Peichl, L., Cremer, T., Guck, J., and Joffe, B. (2009). Nuclear Architecture of Rod Photoreceptor Cells Adapts to Vision in Mammalian Evolution. Cell *137*, 356–368.

Solovei, I., Wang, A.S., Thanisch, K., Schmidt, C.S., Krebs, S., Zwerger, M., Cohen, T.V., Devys, D., Foisner, R., Peichl, L., et al. (2013). LBR and lamin A/C sequentially tether peripheral heterochromatin and inversely regulate differentiation. Cell *152*, 584–598.

Sparvoli, E., Levi, M., and Rossi, E. (1994). Replicon clusters may form structurally stable complexes of chromatin and chromosomes. Journal of Cell Science *107 (Pt 11)*, 3097–3103.

Spector, D.L. (2006). SnapShot: Cellular bodies. Cell *127*, 1071.

Spector, D.L., and Lamond, A.I. (2011). Nuclear speckles. Cold Spring Harb Perspect Biol *3*.

Speicher, M.R., and Carter, N.P. (2005). The new cytogenetics: blurring the boundaries with molecular biology. Nat. Rev. Genet. *6*, 782–792.

Sporbert, A., Gahl, A., Ankerhold, R., Leonhardt, H., and Cardoso, M.C. (2002). DNA polymerase clamp shows little turnover at established replication sites but sequential de novo assembly at adjacent origin clusters. Molecular Cell *10*, 1355–1365.

Strahl, B.D., and Allis, C.D. (2000). The language of covalent histone modifications. Nature *403*, 41–45.

Szymborska, A., de Marco, A., Daigle, N., Cordes, V.C., Briggs, J.A.G., and Ellenberg, J. (2013). Nuclear pore scaffold structure analyzed by super-resolution microscopy and particle averaging. Science *341*, 655–658.

Talwar, S., Kumar, A., Rao, M., Menon, G.I., and Shivashankar, G.V. (2013). Correlated spatio-temporal fluctuations in chromatin compaction states characterize stem cells. Biophys. J. *104*, 553–564.

Tanabe, H., Müller, S., Neusser, M., Hase, von, J., Calcagno, E., Cremer, M., Solovei, I., Cremer, C., and Cremer, T. (2002). Evolutionary conservation of chromosome territory arrangements in cell nuclei from higher primates. Proc. Natl. Acad. Sci. U.S.a. *99*, 4424–4429.

Tanay, A., and Cavalli, G. (2013). Chromosomal domains: epigenetic contexts and functional implications of genomic compartmentalization. Curr. Opin. Genet. Dev. *23*, 197–203.

Tang, J., Akerboom, J., Vaziri, A., Looger, L.L., and Shank, C.V. (2010). Near-isotropic 3D optical nanoscopy with photon-limited chromophores. Proceedings of the National Academy of Sciences *107*, 10068–10073.

Taniura, H., Glass, C., and Gerace, L. (1995). A chromatin binding site in the tail domain of nuclear lamins that interacts with core histones. The Journal of Cell Biology *131*, 33–44.

TAYLOR, J.H. (1960). Asynchronous duplication of chromosomes in cultured cells of Chinese hamster. J Biophys Biochem Cytol *7*, 455–464.

Técher, H., Koundrioukoff, S., Azar, D., Wilhelm, T., Carignon, S., Brison, O., Debatisse, M., and Le Tallec, B. (2013). Replication dynamics: biases and robustness of DNA fiber analysis. Journal of Molecular Biology *425*, 4845–4855.

Thoma, F., and Koller, T. (1977). Influence of histone H1 on chromatin structure.

Cell *12*, 101–107.

Tóth, K.F., Knoch, T.A., Wachsmuth, M., Frank-Stöhr, M., Stöhr, M., Bacher, C.P., Müller, G., and Rippe, K. (2004). Trichostatin A-induced histone acetylation causes decondensation of interphase chromatin. Journal of Cell Science *117*, 4277–4287.

Tremethick, D.J. (2007). Higher-order structures of chromatin: the elusive 30 nm fiber. Cell *128*, 651–654.

Tumbar, T., Sudlow, G., and Belmont, A.S. (1999). Large-scale chromatin unfolding and remodeling induced by VP16 acidic activation domain. The Journal of Cell Biology *145*, 1341–1354.

van Steensel, B. (2011). Chromatin: constructing the big picture. The EMBO Journal *30*, 1885–1895.

Verschure, P.J., van Der Kraan, I., Manders, E.M., and van Driel, R. (1999). Spatial relationship between transcription sites and chromosome territories. The Journal of Cell Biology *147*, 13–24.

Vicidomini, G., Moneron, G., Han, K.Y., Westphal, V., Ta, H., Reuss, M., Engelhardt, J., Eggeling, C., and Hell, S.W. (2011). Sharper low-power STED nanoscopy by time gating. Nat. Methods *8*, 571–573.

Visser, A.E., Jaunin, F., Fakan, S., and Aten, J.A. (2000). High resolution analysis of interphase chromosome domains. Journal of Cell Science *113 (Pt 14)*, 2585–2593.

Visvanathan, A., Ahmed, K., Even-Faitelson, L., Lleres, D., Bazett-Jones, D.P., and Lamond, A.I. (2013). Modulation of Higher Order Chromatin Conformation in Mammalian Cell Nuclei Can Be Mediated by Polyamines and Divalent Cations. PLoS ONE *8*, e67689.

Vogelsang, J., Kasper, R., Steinhauer, C., Person, B., Heilemann, M., Sauer, M., and Tinnefeld, P. (2008). A reducing and oxidizing system minimizes photobleaching and blinking of fluorescent dyes. Angew. Chem. Int. Ed. Engl. *47*, 5465–5469.

Volpi, E.V., Chevret, E., Jones, T., Vatcheva, R., Williamson, J., Beck, S., Campbell, R.D., Goldsworthy, M., Powis, S.H., Ragoussis, J., et al. (2000). Large-scale chromatin organization of the major histocompatibility complex and other regions of human chromosome 6 and its response to interferon in interphase nuclei. Journal of Cell Science *113 (Pt 9)*, 1565–1576.

Weintraub, H., and Groudine, M. (1976). Chromosomal subunits in active genes have an altered conformation. Science *193*, 848–856.

Williams, R.R.E., Broad, S., Sheer, D., and Ragoussis, J. (2002). Subchromosomal positioning of the epidermal differentiation complex (EDC) in keratinocyte and lymphoblast interphase nuclei. Experimental Cell Research *272*, 163–175.

Williamson, I., Berlivet, S., Eskeland, R., Boyle, S., Illingworth, R.S., Paquette, D., Dostie, J., and Bickmore, W.A. (2014). Spatial genome organization: contrasting views from chromosome conformation capture and fluorescence in situ hybridization. Genes & Development *28*, 2778–2791.

Willig, K.I., Harke, B., Medda, R., and Hell, S.W. (2007). STED microscopy with continuous wave beams. Nat. Methods *4*, 915–918.

Wilson, K.L., and Foisner, R. (2010). Lamin-binding Proteins. Cold Spring Harb Perspect Biol *2*, a000554–a000554.

Wittmann, T., Bokoch, G.M., and Waterman-Storer, C.M. (2003). Regulation of leading edge microtubule and actin dynamics downstream of Rac1. The Journal of Cell Biology *161*, 845–851.

Wong, H., Marie-Nelly, H., Herbert, S., Carrivain, P., Blanc, H., Koszul, R., Fabre, E., and Zimmer, C. (2012). A Predictive Computational Model of the Dynamic 3D Interphase Yeast Nucleus. Curr. Biol. 1–10.

WONGLUMSOM, W., VISHNUBHATLA, A., and FUNG, D.Y.C. (2000). EFFECT OF VOLUME OF LIQUID ENRICHMENT MEDIUM CONTAINING OXYRASE� ON GROWTH OF CAMPYLOBACTER JEJUNI. J Rapid Methods Auto Microbiol *8*, 111–139.

Woodcock, C.L., and Ghosh, R.P. (2010). Chromatin Higher-order Structure and Dynamics. Cold Spring Harb Perspect Biol *2*, a000596–a000596.

Woodcock, C.L. (2006). Chromatin architecture. Current Opinion in Structural Biology *16*, 213–220.

Wu, C., Bassett, A., and Travers, A. (2007). A variable topology for the 30-nm chromatin fibre. EMBO Rep *8*, 1129–1134.

Yurov, Y.B., and Liapunova, N.A. (1977). The units of DNA replication in the mammalian chromosomes: evidence for a large size of replication units. Chromosoma *60*, 253–267.

Yusufzai, T.M., Tagami, H., Nakatani, Y., and Felsenfeld, G. (2004). CTCF tethers an insulator to subnuclear sites, suggesting shared insulator mechanisms across species. Molecular Cell *13*, 291–298.

Zhou, J., Ashouian, N., Delepine, M., Matsuda, F., Chevillard, C., Riblet, R., Schildkraut, C.L., and Birshtein, B.K. (2002). The origin of a developmentally regulated Igh replicon is located near the border of regulatory domains for Igh replication and expression. Proc. Natl. Acad. Sci. U.S.a. *99*, 13693–13698.

Zidovska, A., Weitz, D.A., and Mitchison, T.J. (2013). Micron-scale coherence in interphase chromatin dynamics. Proceedings of the National Academy of Sciences *110*, 15555–15560.

Zink, D., Bornfleth, H., Visser, A., Cremer, C., and Cremer, T. (1999). Organization of early and late replicating DNA in human chromosome territories. Experimental Cell Research *247*, 176–188.

Zink, D., Cremer, T., Saffrich, R., Fischer, R., Trendelenburg, M.F., Ansorge, W., and Stelzer, E.H. (1998). Structure and dynamics of human interphase chromosome territories in vivo. Hum. Genet. *102*, 241–251.

Zink, D. (2006). The temporal program of DNA replication: new insights into old questions. Chromosoma *115*, 273–287.

Zirbel, R.M., Mathieu, U.R., Kurz, A., Cremer, T., and Lichter, P. (1993). Evidence for a nuclear compartment of transcription and splicing located at chromosome domain boundaries. Chromosome Res *1*, 93–106.

Ziv, Y., Bielopolski, D., Galanty, Y., Lukas, C., Taya, Y., Schultz, D.C., Lukas, J., Bekker-Jensen, S., Bartek, J., and Shiloh, Y. (2006). Chromatin relaxation in response to DNA double-strand breaks is modulated by a novel ATM- and KAP-1 dependent pathway. Nat. Cell Biol. *8*, 870–876.

Zorn, C., Cremer, C., Cremer, T., and Zimmer, J. (1979). Unscheduled DNA synthesis after partial UV irradiation of the cell nucleus. Distribution in interphase and metaphase. Experimental Cell Research *124*, 111–119.

Zullo, J.M., Demarco, I.A., Piqué-Regi, R., Gaffney, D.J., Epstein, C.B., Spooner, C.J., Luperchio, T.R., Bernstein, B.E., Pritchard, J.K., Reddy, K.L., et al. (2012). DNA sequence-dependent compartmentalization and silencing of chromatin at the nuclear lamina. Cell *149*, 1474–1487.

Acknowledgements

I want to thank Jan Ellenberg for his constant support and scientific guidance throughout my PhD project.

I would like to thank my thesis advisory committee – Christoph Müller, Lars Hufnagel and Ulrich Schwarz - for taking time and interesting in the project. I am grateful to Christoph Müller and Ulrich Schwarz for reviewing the thesis and Karsten Rippe for agreeing to participate in the defense committee.

Completing this work would have been all the more difficult were it not for my colleagues in the lab, past and present: – Aicha, Anna, Andrea, Annelie, Antje, Antonio, Bianca, Birgit, Catherine, Jean-Karim, Judith, Julia, Julius, Malte, Manu, Masashi, Mayumi, Mikhail, Moritz, Nathalie, Nike, Petr, Rob, Shotaro, Sébastien, Steffi, Sylvia, Tanja, Thomas, Tomo, Vilma and Yin - thank you for your constant support and advice.

I would like to thank Sébastien Huet for taking me under his wings, when I newly arrived in the lab. And I want to thank Julia Roberti for performing the main part of the GSDIM experiments, which was an important contribution to this work. I also want to thank Anna Szymborska for all her valuable input on all aspects of super-resolution microscopy, from experimental setup to image analysis. I also want to thank Julius Hossain, who keeps providing swift help and invaluable advice on all image processing and visualization issues. Petr Strnad who helped me countless times with MATLAB-related issues. Bianca Nijmeijer and Nathalie Daigle for general help and advice.

The ALMF and CMCI at EMBL – especially Stefan, Tischi, Marko, Yury and Kota, thank you for constantly proving advice and technical expertise throughout the project.

I want to thank my parents for a lifetime of love and support, for sparking my interest in science, and for being role models in so many aspects of life.

奶奶; 爷爷, 谢谢您们对我的照顾和恩爱, 您们永远是我 的榜样。

Volker, thank you for being an inexhaustible source of good spirits through it all, making hard days easier and good days better.

Erklärung

Ich versichere, dass ich diese Arbeit selbstständig verfasst und keine anderen als die angegebenen Quellen und Hilfsmittel benutzt habe.

Heidelberg, den 20. September 2015

Wanqing Xiang